NORTHWESTERN UNIVERSITY

The Criterion for Chaos in Three-Planet Systems and Warped Planet-Disk Interactions

A DISSERTATION

SUBMITTED TO THE GRADUATE SCHOOL
IN PARTIAL FULFILLMENT OF THE REQUIREMENTS

for the degree

DOCTOR OF PHILOSOPHY

Field of Astronomy

By

Jeremy Rath

EVANSTON, ILLINOIS

March 2023

Acknowledgements

First and foremost, I thank God for all He has done to direct my path and provide what I have needed. I want to thank my family—my wife, Anastasia, my parents, Clifton and Jane, and my sisters, Alyssa, Brittany, and Crystal, and my brother-in-law, Daniel Webb—and friends—Spencer Davis, Jonathan Solis, Dominic Bayer, and Matthew Arakaky—for their gracious support and encouragement throughout this entire process. And special thanks to my friend, Ian Founds, who was always willing to discuss details of my research and my writing.

I am deeply grateful to my supervisor, Professor Lithwick, for his continued and abundant support throughout my PhD; he has changed the way I think, write, and present, which is invaluable to me. I also want to thank my co-authors, Dr. Sam Hadden and Dr. Diego Muñoz, and research group member, Dr. Adam Dempsey, for their mentorship, assistance, and helpful discussions. Additionally, I would like to thank my thesis committee, Professor Rasio and Professor Tchekhovskoy, for their helpful discussions in my prospectus exam and my defense, and the advice they gave me going forward.

The research presented in this thesis was supported in part through the computational resources and staff contributions provided for the Quest high performance computing facility at Northwestern University which is jointly supported by the Office of the Provost, the Office for Research, and Northwestern University Information Technology. Additionally, this research was supported in part by the Illinois Space Grant.

ABSTRACT

The Criterion for Chaos in Three-Planet Systems

and

Warped Planet-Disk Interactions

Jeremy Rath

We establish the criterion for chaos in three-planet systems, for systems similar to those discovered by the Kepler spacecraft. Our main results are as follows: (i) The simplest criterion, which is based on overlapping mean motion resonances (MMRs), only agrees with numerical simulations at a very crude level. (ii) Much greater accuracy is attained by considering neighboring MMRs that do not overlap. We work out the widths of the chaotic zones around each of the neighbors, and also provide simple approximate expressions for the widths. (iii) Even greater accuracy is provided by the overlap of three-body resonances (3BRs), which accounts for the fine-grained structure seen in maps from N-body simulations, and also predicts Lyapunov times. From previous studies, it is unclear whether interplanetary chaos should be attributed to the overlap of MMRs or of 3BRs. We show that the two apparently contradictory viewpoints are in fact consistent: both predict the same criterion for chaos. (iv) We compare the predicted criterion with

high-resolution maps of chaos from N-body simulations, and show that they agree at a high level of detail.

Additionally, we derive from first principles the linear warp equations for an inclined disk perturbed by a planet. The equations predict the general solution is a flat disk interior to the planet's orbit, a smooth transition region extending to $\sim R/c_0$, and a flat outer disk. We used the warp equations to derive a bending criterion based on the parameters of the planet and disk. Finally, we test both the warp equations and the bending criterion with several 3D numerical simulations performed with the AREPO code, finding good agreement between theory and numerics.

Table of Contents

List of Figures

CHAPTER 1

The Criterion for Chaos in Three-Planet Systems

1.1. Introduction

In the Solar System, the planets' orbits are chaotic (Holman & Murray, 1996; Laskar, 1996; Laskar & Gastineau, 2009). Many exoplanetary systems are also chaotic, or at least close to the threshold for chaos, e.g., Kepler-11 (Mahajan & Wu, 2014; Yee et al., 2021), Kepler-36 (Deck et al., 2012), Kepler-102 (Volk & Malhotra, 2020), GJ876 (Goździewski et al., 2002; Batygin et al., 2015a), and Kepler-24, Kepler-85, and Kepler-444 (Yee et al., 2021). The chaos cannot be too violent, because otherwise the systems would not survive for billions of years. That raises the question of how planets were emplaced into such delicate configurations. It also opens the door to using observed planetary configurations to learn about their early history. But our understanding of how chaos works in planetary systems is not yet sufficient to answer such questions.

A simple and powerful criterion for the presence of chaos is *resonance overlap* (Walker & Ford, 1969; Chirikov, 1979). Resonance overlap accounts for much of the chaos in planetary systems. But which resonances overlap depends on the system, as planetary systems harbor a variety of different kinds of resonances. In nearly circular two-planet systems, decreasing the planets' separation drives them toward chaos. There is a critical separation inside of which the orbits are always chaotic, and its value is determined by where neighboring first-order mean motion resonances (MMRs) overlap (Wisdom, 1980;

Deck et al., 2013). Two-planet systems can also be driven toward chaos by increasing their eccentricity, because the widths of MMRs increase with increasing eccentricity. The critical eccentricity for chaos has been determined by, e.g., Mardling (2008); Hadden & Lithwick (2018). It depends not only on first-order MMRs, but on higher-order MMRs as well. In systems of more than two planets, Tamayo et al. (2021) suggest that chaos is generally attributable to the overlap of two-body MMRs—similar to the two-planet case.

Overlap of other kinds of resonances also produces chaos. In the inner Solar System, chaos is caused by the overlap of secular resonances (Laskar, 1996; Lithwick & Wu, 2011; Batygin et al., 2015b). And in the outer Solar System, chaos has been attributed to the overlap of three-body resonances (3BRs; Murray & Holman, 1999). Quillen (2011) and Petit et al. (2020) suggest that chaos in planetary systems is driven by overlapping 3BRs, while Tamayo et al. (2021) suggest that overlapping two-body MMRs are responsible. One of the goals of this paper is to resolve this apparent discrepancy.

Chaos in generic Hamiltonian systems is understood at a much deeper level than simply resonance overlap (see, e.g., textbooks and reviews of Chirikov, 1979; Lichtenberg & Lieberman, 1983; Escande, 1985; Zaslavsky, 2007). Two concepts in particular play a prominent role in this paper. First, nearby resonances that do not overlap excite chaos in the vicinity of their separatrices. The extent of the chaotic zone around each separatrix is readily calculable by applying the "whisker" or "separatrix" map (which we shall also refer to as the "theory of kicks"). One might suspect that the resulting correction to the resonance overlap criterion is at best an order-unity one. But, as we shall demonstrate, resonance overlap is only approximately correct when the two resonances have comparable strengths. In the more general case, where one resonance is much stronger than the other,

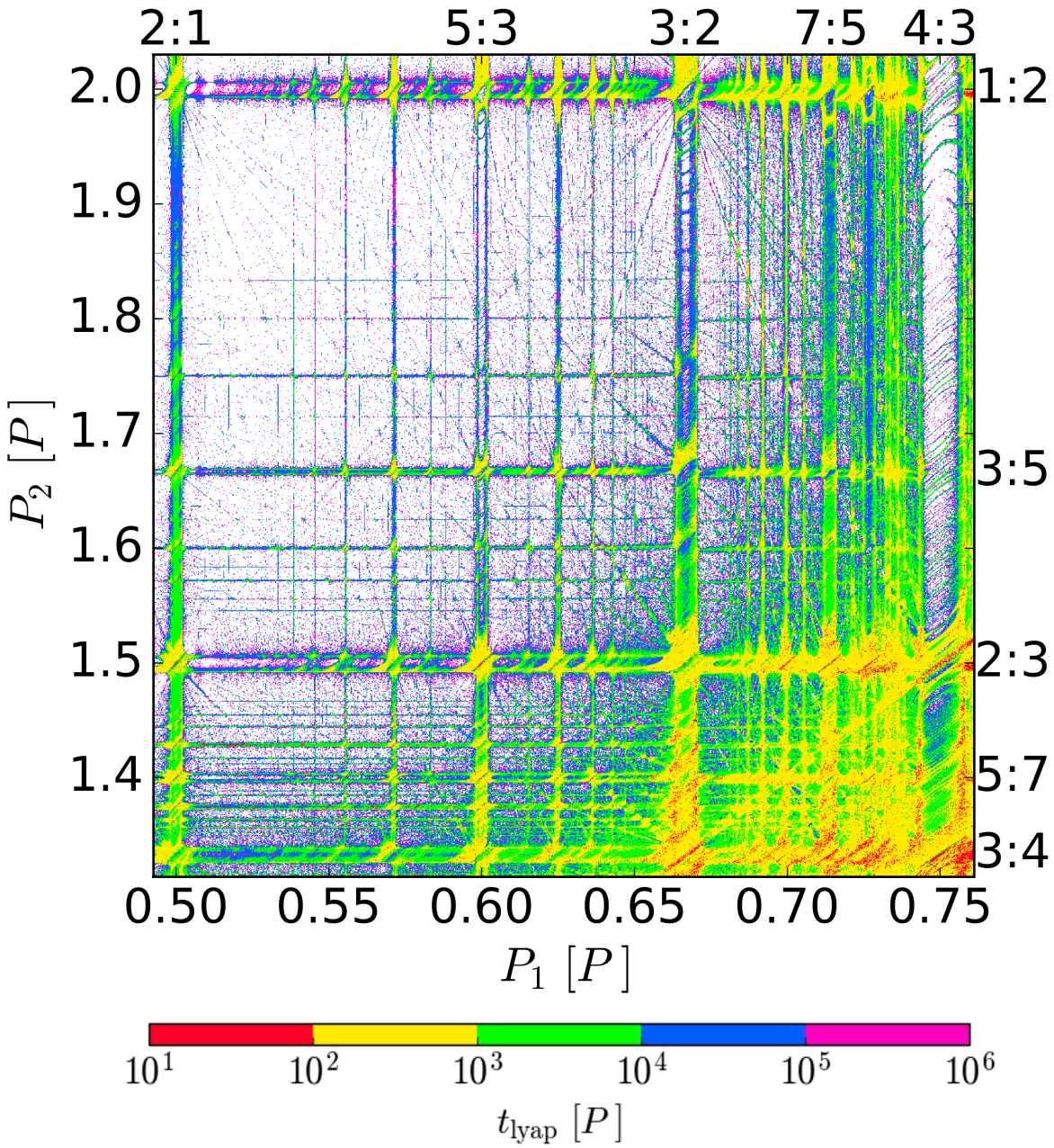

Figure 1.1. Lyapunov times for our fiducial three-planet system in the PP-plane: The axes give the initial orbital periods of the inner and outer planets, in units of the middle planet's period, and the Lyapunov time is as colored. The locations of 1st and 2nd order MMRs are on the top and right axes. Broadly speaking, MMRs tend to be chaotic, and overlapping resonances enhance chaos.

the correction becomes very large. The second concept is that of secondary resonances: two nearby resonances excite secondary resonances, and those secondaries can overlap and lead to chaos.[1] There are then two predictions for the extent of the chaotic zone—from the theory of kicks and from secondary resonances—and they have been shown to agree with each other (e.g. Lichtenberg & Lieberman, 1983). While these concepts are detailed in standard references, we provide a self-contained discussion in this paper in order to aid the nonexpert. We also develop some improvements on the standard theory, as summarized in Section 1.6.1.

The outline of this paper is as follows: In Section 1.2, we use numerical integrations to map out the chaos of a fiducial three-planet system.[2] We use that map as a touchstone for the theory of chaos developed in later sections. In Section 1.3, we show how the dynamics near a crossing of two MMRs can be reduced to a much simpler model system: the perturbed pendulum. In Section 1.4, we review the theory of kicks for the perturbed pendulum, and develop an "improved" theory that is applicable further away from the separatrix. We then use that theory to predict the chaos seen in the touchstone map. In Section 1.5, we apply the theory of overlapping secondary resonances to predict chaos. In the final section (Section 2.4), we provide a summary, assess the validity of our main approximations, compare to prior work, and discuss the outer Solar System.

[1] A 3BR is an example of a secondary resonance; it is produced when the two primary resonances involve three planets.

[2] We treat the planets as idealized point particles, neglecting non-Newtonian effects such as tides and general relativity.

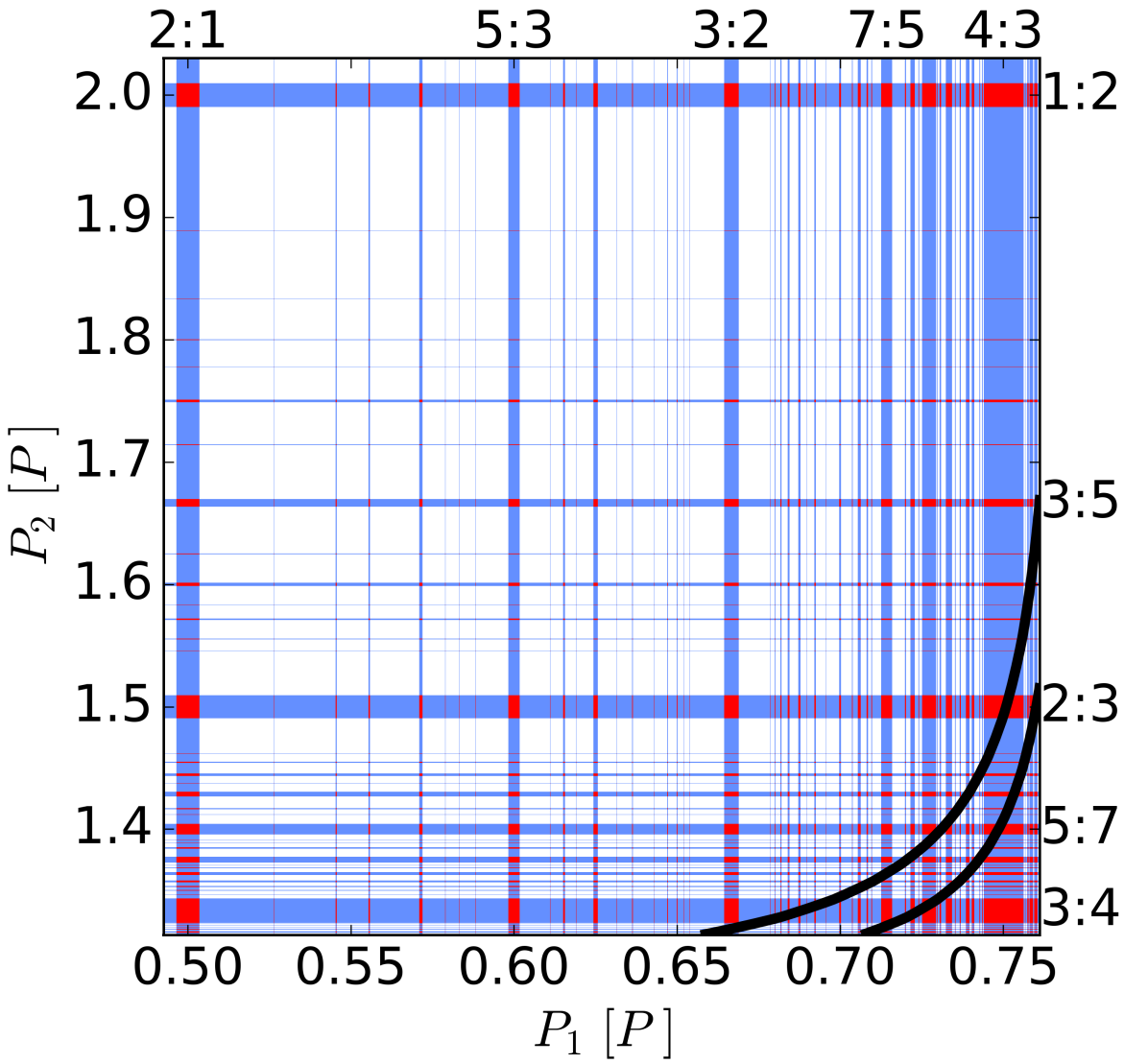

Figure 1.2. Locations and widths of two-body MMRs for the system depicted in Figure 1.1. The vertical blue bands are resonances between the inner two planets; the horizontal bands are between the outer two; and overlapping zones are red. The first- and second-order MMRs are labeled; but all resonances are shown in blue, unless their width is less than the pixel size. Tamayo et al. (2021) provide a semi-analytic formula for the chaos criterion based on two-body MMR overlap. Their results are shown by the two black curves in the lower right corner. The lower curve is based on the initial eccentricities, and the upper is based on the maximum eccentricities reached via purely secular evolution. The curves were made with D. Tamayo's code SPOCK, which is publicly available at github.com/dtamayo/spock.

1.2. Map of Chaos in a fiducial Three-Planet System

We explore the chaotic behavior of a fiducial three-planet system. The system we choose is similar to planets c, d, and e of Kepler-11, as given by the all-eccentric fit of Table S4 in Lissauer et al. (2011), with two modifications: the middle planet's mass is set to zero, and its eccentricity is boosted. (Lissauer et al. 2013 provide updated parameters for the Kepler-11 planets, but we do not use those.). To be explicit, the masses of the three planets are $\{12, 0, 9.3\}M_{\oplus}$; the eccentricities are $\{0.003, 0.070, 0.016\}$; the angular orbital elements and stellar mass are set to those in Lissauer et al. (2011); and inclinations are set to zero. Converting the middle planet to a test particle allows us to focus on its dynamics, while neglecting its backreaction on the other bodies. As discussed in Section 1.6.2, generalizing to a massive middle planet is straightforward.

Figure 1.1 shows the result from a suite of integrations of the fiducial system in the period-period ("PP") plane, i.e., the axes represent the initial orbital periods of the inner and outer planets (P_1 and P_2, respectively). For comparison, the nominal orbital periods from Lissauer et al. (2011) are $P_1/P = 0.57$ and $P_2/P = 1.41$, where P is the period of the middle planet. Each point in Figure 1.1 represents an integration with given initial periods, performed with the WHFast integrator (Rein & Tamayo, 2015) in REBOUND (Rein & Liu, 2012). The color represents the Lyapunov time, which is determined by fitting the MEGNO with a least-squares fit (Cincotta et al., 2003). In general, the Lyapunov time can vary in time, whereas for Figure 1.1 we wish to show the Lyapunov time toward the beginning of the simulation. Therefore, we halt a simulation when the runtime exceeds ten times the Lyapunov time, which we have found is typically long enough to

provide a sufficiently accurate measurement of the Lyapunov time. The systems in which the inferred Lyapunov time exceeds 106 P are colored white in Figure 1.1.

The bulk of this paper is aimed at predicting the structure in Figure 1.1. We observe that much of the chaos is associated with MMRs. For comparison, Figure 1.2 shows in blue the locations and widths of the MMRs between the inner two planets (vertical bands) and between the outer two planets (horizontal bands), where the widths are taken from Equations (1.21) and (1.23) below. The simplest predictor for chaos is resonance overlap (Chirikov, 1979). Figure 1.2 depicts the overlapping regions in red. We observe that resonance overlap provides a rough guide to where the chaotic zones are in Figure 1.1. Resonance overlap is seen to be most successful when the widths of the two overlapping resonances are comparable. But it does not explain, e.g., why many of the resonances in Figure 1.1 are chaotic even when there appear to be no nearby overlapping resonances; nor why there are diagonal chaotic bands in Figure 1.1. We shall address these issues, and others, below.

1.3. Chaos of a Perturbed Pendulum

1.3.1. Reduction to Perturbed Pendulum

In order to explain the structure seen in period-period maps (such as Figure 1.1), we examine how a test particle behaves when it is affected by two MMRs, one with an interior planet (to be labeled by subscript 1) and one with an exterior planet (labeled 2). As we show in Appendix A, the test particle's Hamiltonian can be written as a *perturbed*

pendulum:[3]

$$H(\phi, p, t) = \frac{p^2}{2} - \epsilon_1 \cos(\phi) - \epsilon_2 \cos(r(\phi - \nu t)) \ , \tag{1.1}$$

where the first two terms describe a simple pendulum, and the third is the perturbation. Before studying the dynamics of the perturbed pendulum, we summarize how it is related to the orbital system under consideration:

- The first cosine term is from the MMR with the inner planet, and the second is from the one with the outer planet. The dimensionless coefficients (ϵ_1 and ϵ_2) are proportional to the corresponding planet's mass, and are both $\ll 1$.
- The parameter ν is proportional to the difference between (i) the test particle's mean motion if it is at nominal resonance with planet 1; and (ii) the corresponding quantity with planet 2 (Equation A.9). The parameter r is a ratio of integers: if we label the frequency ratio of the inner resonance by j_1:$j_1 - k_1$, and the frequency ratio of the outer as j_2:$j_2 + k_2$ (for positive integer j's and k's), then $r = j_2/j_1$.
- The canonical co-ordinate ϕ is the resonant argument of the inner planet's resonance (Equation A.10), The argument of the second cosine,

$$\psi \equiv r(\phi - \nu t) \tag{1.2}$$

[3]The main approximation used to derive Equation (1.1) is the "pendulum approximation," whereby the coefficients of the cosine terms are assumed to be constant (Murray & Dermott, 1999). We assess its validity in Section 1.6.2. We also adopt a novel approximation, following Hadden (2019), that allows us to combine together all of the $k_1 + 1$ cosine terms associated with the inner resonance, and similarly all of the $k_2 + 1$ terms associated with the outer. Without this approximation, the form of Equation (1.1) would only be applicable to the case where the inner and outer planets are circular, and the middle planet is eccentric. But with it, we may consider three eccentric planets as a nearly trivial extension of the circular case. See Section A.2 for further details.

is the resonant argument of the outer planet's resonance.

The form of Equation (1.1), with the first two terms referring to the inner planet's resonance, is convenient when the inner planet dominates the dynamics, and the outer planet is treated as a perturbation. But that is merely a convention. By symmetry, one could swap ϵ_1 and ϵ_2 in Equation (1.1) without affecting the dynamics, provided ϕ, p, r, and ν are redefined by swapping the 1 and 2 indices in their definitions (Equations A.8–A.11). Nonetheless, throughout this paper we retain the convention of Equation (1.1), with p and ϕ corresponding to the inner planet's resonance (the "ϵ_1-resonance") and ψ to the outer planet's (the "ϵ_2-resonance").

Equation (1.1) has four parameters (ϵ_1, ϵ_2, r, and ν). These may be reduced to three by rescaling p, H, t, and ν to reduce Equation (1.1) to $H(\phi, p, t) = \frac{p^2}{2} - \cos(\phi) - \frac{\epsilon_2}{\epsilon_1}\cos(r(\phi - \nu t))$. Therefore, in analyzing Equation (1.1), one may set $\epsilon_1 \to 1$ without loss of generality. Despite that, we shall retain ϵ_1 for most of the paper, with the principal exceptions being Section 1.4.2.1 and Appendices B–D, where we set $\epsilon_1 = 1$ to reduce clutter.[4]

1.3.2. Surfaces of Section

We start by using a surface of section to exhibit the dynamics of Equation (1.1), similar to what is done in Murray & Holman (2001) and Zaslavsky (2007). For each surface of section, we fix the parameters (r, ν, ϵ_1 and ϵ_2), and numerically integrate the perturbed

[4]If one analyzes a perturbed pendulum with $\epsilon_1 = 1$, the results are easily generalized to arbitrary values of ϵ_1 by setting

$$\{\epsilon_2, p, \nu, t, H\} \to \left\{\frac{\epsilon_2}{\epsilon_1}, \frac{p}{\sqrt{\epsilon_1}}, \frac{\nu}{\sqrt{\epsilon_1}}, t\sqrt{\epsilon_1}, \frac{H}{\epsilon_1}\right\} .$$

pendulum's equations of motion for different initial values of p and ϕ. This experiment is equivalent to fixing the orbits and masses of the two planets and exploring what happens for different initial semimajor axes of the test particle. From each integrated trajectory, we plot snapshots in the p-ϕ plane at times t such that $r\nu t = \{0, 2\pi, 4\pi, \cdots\}$. Stable trajectories will create 1D curves in the p-ϕ plane, while chaotic ones will randomly fill a 2D region. Figure 1.3 shows an example surface of section with $r = 1$, $\epsilon_1 = 1$, $\epsilon_2 = 0.1$, and a large forcing frequency ($\nu \gg 1$). In that case, each cosine term (i.e., "resonance") in Equation (1.1) produces a "cat's eye" in the surface of section. The ϵ_1-resonance is centered at $p = 0$, and the ϵ_2-resonance is centered at ν. Within the ϵ_1-resonance, ϕ librates, and within the other resonance, it is ψ that librates.

For Figure 1.4, we dial down ν, which lowers the ϵ_2-resonance in the p-ϕ plane. In the context of the orbital problem, this corresponds to moving the planets so that the two resonances approach each other. At moderate separation ($\nu = 3.9$), one observes new islands close to the lower resonance's separatrix, and the separatrix becomes chaotic. As ν gets smaller, additional islands appear, and the chaotic region expands. The ϵ_2-separatrix also becomes chaotic. But chaos does not extend below the lower ϵ_1 separatrix, nor above the upper ϵ_2 separatrix. We quantify all of this behavior in the following sections.

We combine the plots for all values of ν by taking a "double surface of section": at each ν we take a cut in the surface of section at $\phi = 0$, and record the values of p where trajectories are chaotic. We then stack these for different values of ν. The result is shown in Figure 1.5(a), where chaotic trajectories are shown in black.[5] A double surface

[5]In practice, we make a double surface of section as follows: we initialize $\phi = \psi = 0$, and $p = p_i$, and plot in black in the p_i-ν plane wherever an orbit with those initial values is chaotic, as indicated by MEGNO. Note that the perturbed pendulum has 1.5 degrees of freedom, and hence the boundary between the chaotic and nonchaotic regions is well defined (Section 4.6 in Chirikov, 1979).

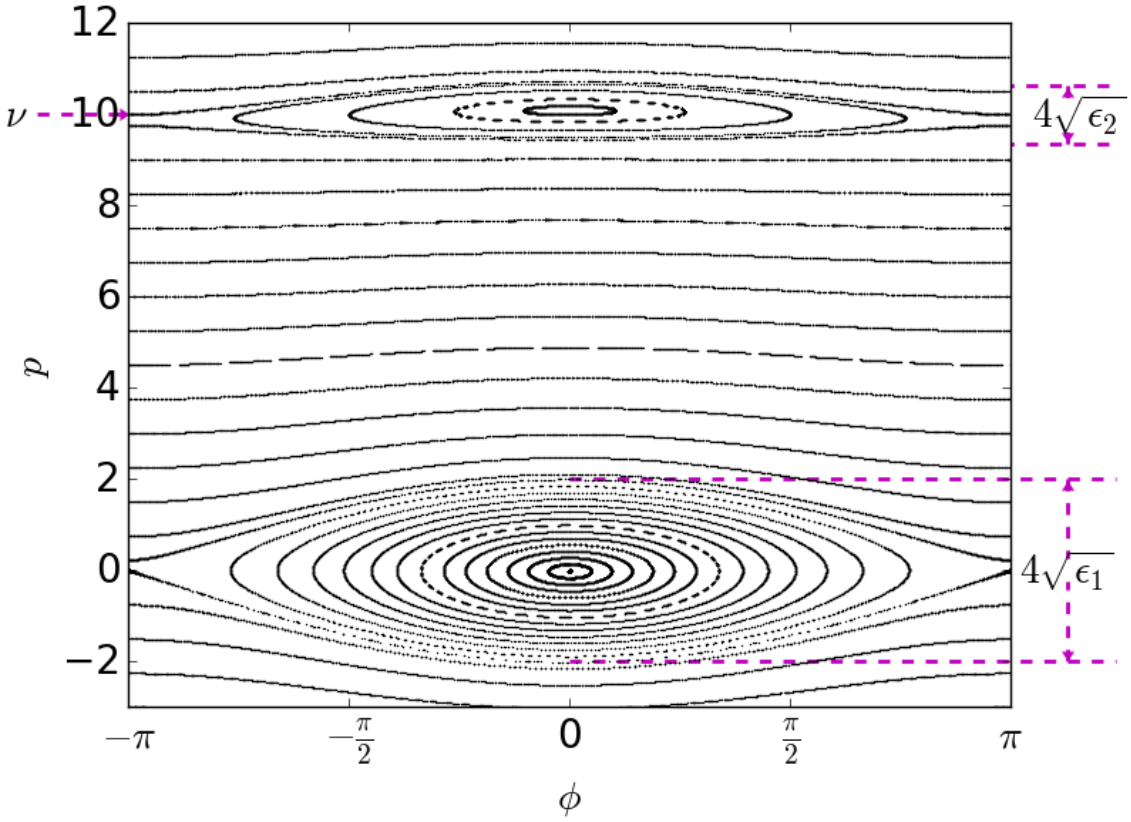

Figure 1.3. A surface of section for the perturbed pendulum with $r = 1$, $\epsilon_1 = 1$, $\epsilon_2 = 0.1$, and $\nu = 10$. At this large value of ν the two resonances appear as "cat's eyes," and are clearly separated. There is also little chaos.

of section is analogous to the PP-plane, because a simple linear change of coordinates brings $\{p, \nu\}$ to $\{P_1, P_2\}$ (Section 1.4.3). Figure 1.5(b) shows, in blue, the locations of the two resonances in the p-ν plane. This plot is the analog of Figure 1.2. The most naive criterion for chaos—resonance overlap—predicts that chaos should occur in the red zone of this plot. Comparing with panel (a), we see that, as before, this prediction provides only a rough guide to the numerical result. It does not explain, e.g., why most of the chaos occurs when the two resonances marginally overlap (i.e. at $\{\nu, p\} \sim \{2, 2\}$ and

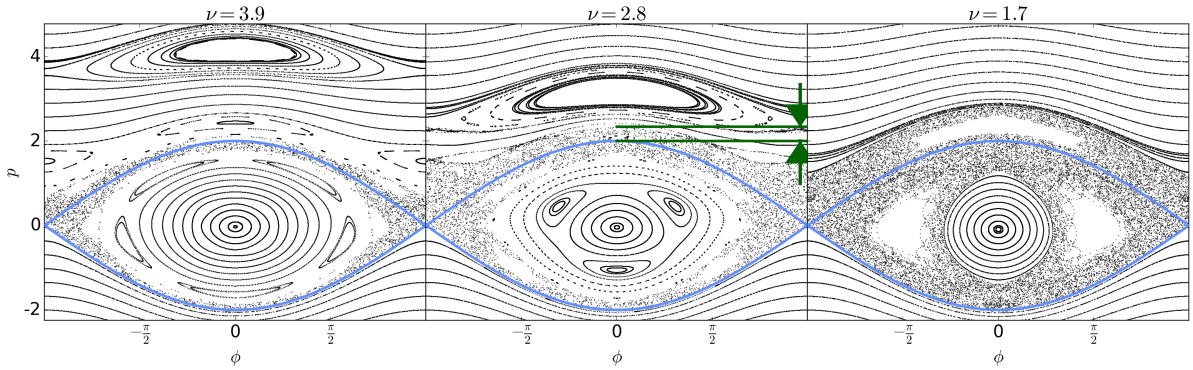

Figure 1.4. Surfaces of section for the perturbed pendulum, as in Figure 1.3, but for three lower values of ν. The separatrices of the ϵ_1 resonance are shown in blue. In the middle panel, the extent of the chaotic region predicted by Equation (1.11) is indicated in green.

$\sim \{-2, -2\}$), nor why much of the chaos consists of spikes that extend from near the points of marginal overlap.

In this paper, we develop two theories to explain the chaos in double surfaces of section, and hence in the PP-plane. The first, which we call the theory of kicks, predicts smoothed shapes for the chaotic zones, e.g., as shown in Figure 1.5(c) in red. The second is based on secondary resonance overlap. It predicts the same smoothed shapes for the chaotic zones, but it also accounts for the spikes, and predicts the Lyapunov times to moderate accuracy.

1.4. Theory of Kicks

In this section, we first derive the criterion for chaos based on the theory of kicks (Section 1.4.1), which is similar to the "whisker map" of Chirikov (1979) and the "separatrix map" of Zaslavsky (2007). We then complete the derivation, leading to two explicit, but approximate, forms for the criterion (Section 1.4.2). We call the first form the classical theory (Chirikov, 1979; Lichtenberg & Lieberman, 1983; Zaslavsky, 2007), and the second

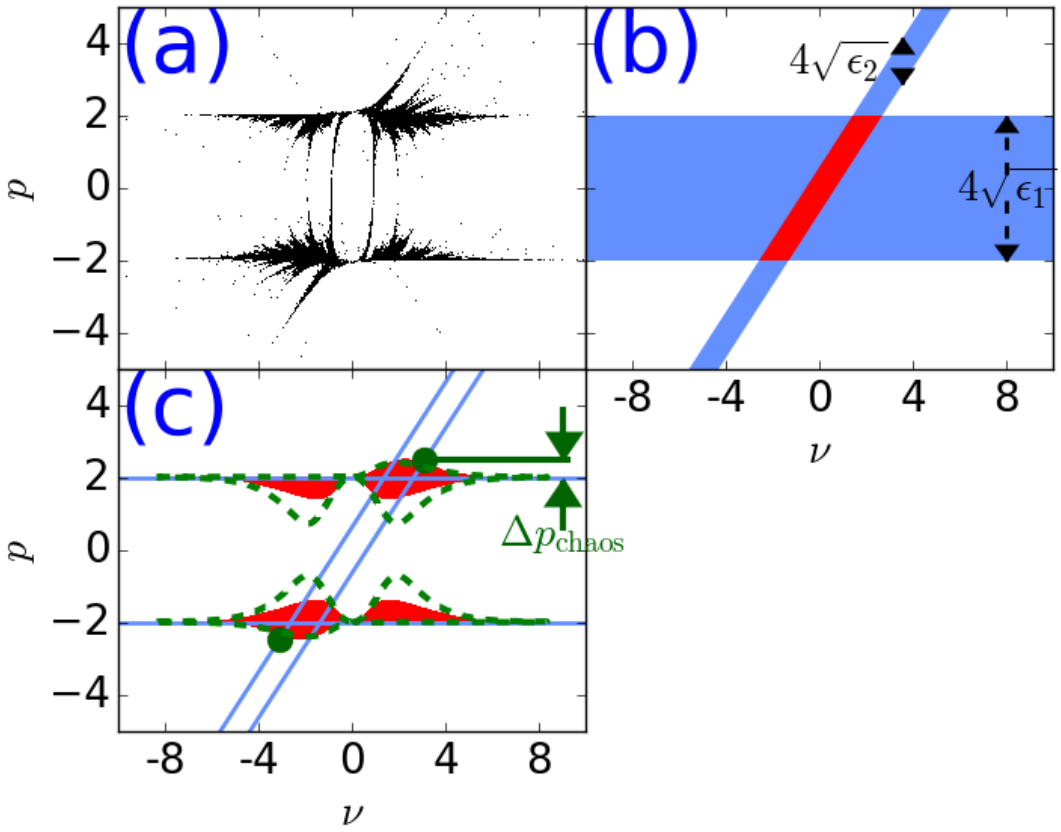

Figure 1.5. (a) Double surface of section for the system in Figure 1.4, showing the chaotic regions in black for many different values of ν (at $\phi = 0$). (b) Prediction for (a), based on naive resonance overlap. The libration regions of both resonances are blue, and the predicted chaotic region is in red. (c) The region predicted to be chaotic by the classical kick criterion (Equation 1.10) is outlined with green dashed curves. The improved kick criterion (Equations 1.8 and 1.17) is shown with the red regions. The green circles show the reduced classical criterion (Equation 1.12).

incorporates our improvements. Next, we apply the improved theory to a single resonance crossing from Figure 1.1, and finally apply it to many more resonance crossings in Figure 1.1.

1.4.1. Kick Criterion

We model the perturbed pendulum (Equation 1.1) as a simple pendulum subjected to discrete kicks that are given by the ϵ_2 term in the Hamiltonian. We focus on an unperturbed trajectory near the separatrix (i.e., the ϵ_1-separatrix). For definiteness, we assume at first that $\nu > 0$ and the trajectory is above the separatrix, in the circulation zone. Whenever ϕ swings from $-\pi$ to π—or, more generally, from $(2k-1)\pi$ to $(2k+1)\pi$ for integer k—the pendulum is considered to have experienced a kick.

Let us consider two successive kicks. The key quantity of interest for whether or not chaos occurs is the *kick phase* $\psi = r(\phi - \nu t)$, which is the argument of the ϵ_2-cosine. Chaos is postulated to occur if the first kick is sufficiently strong that it changes the kick phase at time of the second kick—relative to what it would have been without the first kick—by $\gtrsim 1$. If that happens, it means that the first kick was strong enough to scramble the amplitude of the second kick ($\propto \cos\psi$) by an order-unity amount. The scrambled second kick will in turn scramble the third kick, etc., leading to pseudorandom evolution, and hence chaos.

To calculate the change in kick phase, we first determine how the first kick changes the unperturbed energy, $E = \frac{p^2}{2} - \epsilon_1 \cos\phi$. The equations of motion from the perturbed pendulum give

$$\frac{\mathrm{d}E}{\mathrm{d}t} = -\epsilon_2 r \dot{\phi} \sin(r(\phi - \nu t)) \ . \tag{1.3}$$

Since we consider ϵ_2 to be small, we evaluate the change in energy from the first kick by integrating Equation (1.3) from half a period before the kick to half a period after, while

taking $\phi(t)$ as unperturbed:[6]

$$\delta E \;=\; -\epsilon_2 r \int_{t^{(1)}-\frac{T}{2}}^{t^{(1)}+\frac{T}{2}} \dot{\phi}_{\rm unp} \sin\left[r\left(\phi_{\rm unp}+\phi(t^{(1)})-\nu t\right)\right] {\rm d}t$$

where $t^{(1)}$ is the time of the first kick; the unperturbed $\phi(t) = \phi_{\rm unp}(t-t^{(1)})+\phi(t^{(1)})$, after adopting the convention that $\phi_{\rm unp}(t=0)=0$; and T is the unperturbed period. The above equation may be rewritten as

$$\delta E = -\epsilon_2 r \sin\psi^{(1)} \mathcal{K}(E) \tag{1.4}$$

where

$$\mathcal{K}(E) = \int_{-\frac{T}{2}}^{\frac{T}{2}} \dot{\phi}_{\rm unp}(t') \cos\left[r\left(\phi_{\rm unp}(t')-\nu t'\right)\right] {\rm d}t' \;, \tag{1.5}$$

after changing the time coordinate to $t' = t - t^{(1)}$, making use of the symmetry of $\phi_{\rm unp}$ under time reversal, and defining $\psi^{(1)} = \psi(t=t^{(1)})$. Approximate expressions for $\mathcal{K}(E)$ are presented below. In addition to its dependence on E, $\mathcal{K}$ depends on the parameters ϵ_1, r, and ν.

Given the change in energy, the period changes by $\delta T = \frac{dT}{dE}\delta E$, where the $T(E)$ relationship for an unperturbed pendulum is well-known (e.g., Lichtenberg & Lieberman, 1983). Therefore, the change in kick phase at the second kick is

$$\delta\psi^{(2)} = -r\nu\delta T = \epsilon_2 r^2 \nu \sin\psi^{(1)}\; \mathcal{K}(E)\frac{{\rm d}T}{{\rm d}E} \;, \tag{1.6}$$

[6]This expression for δE is slightly incorrect because it includes "fast oscillations," whose effects average out. In Appendix C, we show how the fast oscillations should be removed.

which has a "typical" value of

$$\delta\psi^{(2)} \sim \epsilon_2 r^2 \nu \mathcal{K}(E) \frac{\mathrm{d}T}{\mathrm{d}E} \tag{1.7}$$

Finally, for chaos to occur, one requires this typical value to be $\gtrsim 1$; i.e., trajectories with energy E that satisfy

$$\left|\frac{\mathrm{d}E}{\mathrm{d}T}\right| \lesssim \epsilon_2 r^2 \left|\nu \mathcal{K}(E)\right| \tag{1.8}$$

are chaotic. We call this the kick criterion.

1.4.2. Two Approximate Kick Criteria

1.4.2.1. Classical Kick Criterion. Previous studies (e.g., Chirikov, 1979; Lichtenberg & Lieberman, 1983; Zaslavsky, 2007) take the unperturbed trajectory to be very near the separatrix ($E \sim \epsilon_1$). One may then evaluate $\mathcal{K}$ by setting ϕ_{unp} in Equation (1.5) to its value on the separatrix, and correspondingly set the integration limits to $\pm\infty$. As we show in Appendix B, the result is

$$\mathcal{K} \approx \nu A_{2r}(r\nu) \tag{1.9}$$

where $A_{2r}(r\nu)$ is the Melnikov-Arnold (MA) integral, the value of which is given in Equation (B.2). The resulting $\mathcal{K}$ is independent of E. In deriving Equation (1.9), we assume, as above, that the unperturbed trajectory is in the circulation zone; and we also set $\epsilon_1 = 1$ for clarity. We shall continue to set $\epsilon_1 = 1$ in the remainder of this subsection, before generalizing to arbitrary ϵ_1 at the end.

Equation (1.8) may be further simplified by using the near-separatrix relation $|dE/dT| \approx |E-1|$, resulting in the "classical kick criterion:"

$$|E-1| < \epsilon_2 r^2 \nu^2 \, |A_{2r}(r\nu)| \ . \tag{1.10}$$

In order to depict this on a double surface of section, we convert E to the value of p at $\phi = 0$, via $E = \frac{p^2}{2} - 1 \approx 1 + 2\Delta p$, where Δp is the height above the separatrix at $\phi = 0$. In that case, Equation (1.10) becomes

$$\Delta p < \Delta p_{\mathrm{chaos},\nu} \equiv \frac{1}{2} \epsilon_2 r^2 \nu^2 \, |A_{2r}(r\nu)| \ . \tag{1.11}$$

The extent of the chaotic zone above the separatrix, $\Delta p_{\mathrm{chaos},\nu}$, is depicted by the arrows in Figure 1.4(b). That extent depends on the height of the ϵ_2 resonance, i.e., on ν. In particular, in Figure 1.5(c), the top green dashed curve in the upper-right quadrant shows the prediction of Equation (1.11) for how $\Delta p_{\mathrm{chaos},\nu}$ depends on ν. Comparing that part of the plot with the numerical result in panel (a) shows good agreement. For $\nu \gg 1$, $A_{2r}(r\nu) \propto e^{-\pi r \nu/2}$ (Equation B.2), and so $\Delta p_{\mathrm{chaos},\nu}$ decays exponentially as ν increases, as seen in panel (c). Furthermore, $\Delta p_{\mathrm{chaos},\nu}$ hits a peak value at $\nu \sim 1$, and then decays to zero as $\nu \to 0$. The peak value is

$$\Delta p_{\mathrm{chaos}} = \frac{1}{2} \epsilon_2 \kappa(r) \tag{1.12}$$

where

$$\kappa(r) \equiv \max_{\nu} r^2\nu^2 \,|A_{2r}(r\nu)\,| \approx \begin{cases} 3.5r^{1.0} & r < 0.28 \\ 8.9r^{1.8} & r > 0.28 \end{cases}, \tag{1.13}$$

and where the latter approximation is from a simple fit that is in error by $\sim 20\%$ near the crossover (at $r = 0.28$), and by $\lesssim 5\%$ away from the crossover. For the case shown in Figure 1.5, $r = 1$ and so $\Delta p_{\rm chaos} = \frac{1}{2} \times 0.1 \times 8.9 = 0.44$. In Figure 1.5(c) we plot a green circle at this distance from the separatrix; note that we position the ν of the circle along the ϵ_2-resonance rather than at the peak of $\Delta p_{\rm chaos}$, for reasons that will be described in Section 1.4.2.2. We refer to Equation (1.12) as the "reduced classical criterion." It will prove useful for estimating the extent of the chaotic zones in a PP diagram.

The remaining green dashed curves in Figure 1.5(c) are calculated similarly. At $\nu > 0$, there are three additional boundaries: in the upper libration zone (i.e., just below $p = 2$), the lower libration zone, and the lower circulation zone. For the first of these, the analysis is the same as previously, except that the period is twice as long, which implies that $|\Delta p_{{\rm chaos},\nu}|$ should be increased by a factor of 2 there. That factor of 2 is erroneously omitted in the literature (e.g., Chirikov, 1979). The boundary in the lower libration zone must be the same as that in the upper, because the two regions depict the same orbits. And in the lower circulation zone, one should simply switch $\nu \to -\nu$ in Equation (1.11)—because an orbit in the lower circulation zone with $\nu > 0$ is equivalent to one in the upper circulation zone with $\nu < 0$, and the previous analysis applies to the upper circulation zone. The remainder of the green curves, i.e., at $\nu < 0$, may be trivially obtained from

those at $\nu > 0$ by antisymmetry. As seen in Figure 1.5, the predicted green curves all agree moderately well with the numerical result of panel (a).

We conclude this subsection by generalizing Equations (1.9), (1.10), and (1.12) to arbitrary $\epsilon_1 \neq 1$, which may easily be done by applying the rules in footnote 4 (as well as $E \to E/\epsilon_1$). The results are as follows:

$$\mathcal{K} \approx \frac{\nu}{\sqrt{\epsilon_1}} A_{2r}\left(\frac{r\nu}{\sqrt{\epsilon_1}}\right) \tag{1.14}$$

$$|E - \epsilon_1| < \frac{\epsilon_2}{\epsilon_1} r^2 \nu^2 \left| A_{2r}\left(\frac{r\nu}{\sqrt{\epsilon_1}}\right)\right| \qquad \text{classical} \tag{1.15}$$

$$\Delta p_{\text{chaos}} = \frac{1}{2}\frac{\epsilon_2}{\sqrt{\epsilon_1}}\kappa(r) \qquad \text{reduced classical} \tag{1.16}$$

and $\kappa(r)$ is left unchanged.

1.4.2.2. Improved Kick Criterion: Although the classical criterion (Equation 1.15) is adequate for predicting the chaos in the system shown in Figure 1.5, it is inadequate for many resonant crossings in the PP diagram. There are two main shortcomings. First, when the chaotic region extends beyond the ϵ_1 separatrix by a distance larger than the width of that resonance, one may not set ϕ_{unp} to its value on the separatrix. From Equation (1.16), that occurs when $\epsilon_2\kappa(r) \gtrsim \epsilon_1$. And second, one must consider the chaos of the ϵ_2-separatrix, which becomes dominant when $\epsilon_2 \gtrsim \epsilon_1$. In the following, we address these two shortcomings in turn.

For the first, we generalize the classical criterion by (a) evaluating dE/dT in Equation (1.8) with the full expression that is valid for any E; and (b) approximating $\mathcal{K}$ without assuming that the trajectory is on the separatrix. We derive that improved approximation in Appendix C. The derivation is subtle, because one must distinguish between fast and

slow oscillations. But the final result is simple: in Equations (1.9) and (1.14), one should replace $\nu \to \nu - \Delta p$, where Δp is the height above the separatrix at $\phi = 0$, i.e., $\Delta p \equiv \sqrt{2(E+\epsilon_1)} - 2\sqrt{\epsilon_1}$. Physically, that result may be understood from the principle that the strength of the kick should depend on the difference in frequency between the perturbing ϵ_2 resonance and that of the test particle at the time of the kick (see Appendix C). It is for this reason that we position the green circles in Figure 1.5 (Equation 1.12) along the ϵ_2 separatrix: the maximum extent of chaos should occur when $\nu - \Delta p \sim 1$ rather than $\nu \sim 1$.

The resulting improved approximation for $\mathcal{K}$ is given by Equation (C.7), for the case when $\nu > 0$, $\epsilon_1 = 1$ and the trajectory is in the upper circulation zone. That is easily generalized to arbitrary ϵ_1 and to the remaining zones, following what we did for the classical criterion. To be explicit, the final "improved kick criterion" is given by Equation (1.8), in which

$$\mathcal{K}(E) \approx \begin{cases} \frac{(\nu - |\Delta p|)}{\sqrt{\epsilon_1}} A_{2r}\left[\frac{r(\nu-|\Delta p|)}{\sqrt{\epsilon_1}}\right] & \text{upper circulation} \\ \frac{(\nu + |\Delta p|)}{\sqrt{\epsilon_1}} A_{2r}\left|\frac{r(\nu+|\Delta p|)}{\sqrt{\epsilon_1}}\right| & \text{libration} \\ \frac{(\nu - |\Delta p|)}{\sqrt{\epsilon_1}} A_{2r}\left[-\frac{r(\nu-|\Delta p|)}{\sqrt{\epsilon_1}}\right] & \text{lower circulation} \end{cases} \tag{1.17}$$

when $\nu > 0$. Now $\mathcal{K}$ depends on E via its dependence on Δp. Very near the separatrix ($E \sim \epsilon_1$), $\mathcal{K}$ reduces to its classical expression. The case when $\nu < 0$ is found by antisymmetry. We show the improved criterion in red in Figure 1.5(c). Its agreement with the numerical result in panel (a) is slightly better than the classical prediction, particularly inside the libration zone.

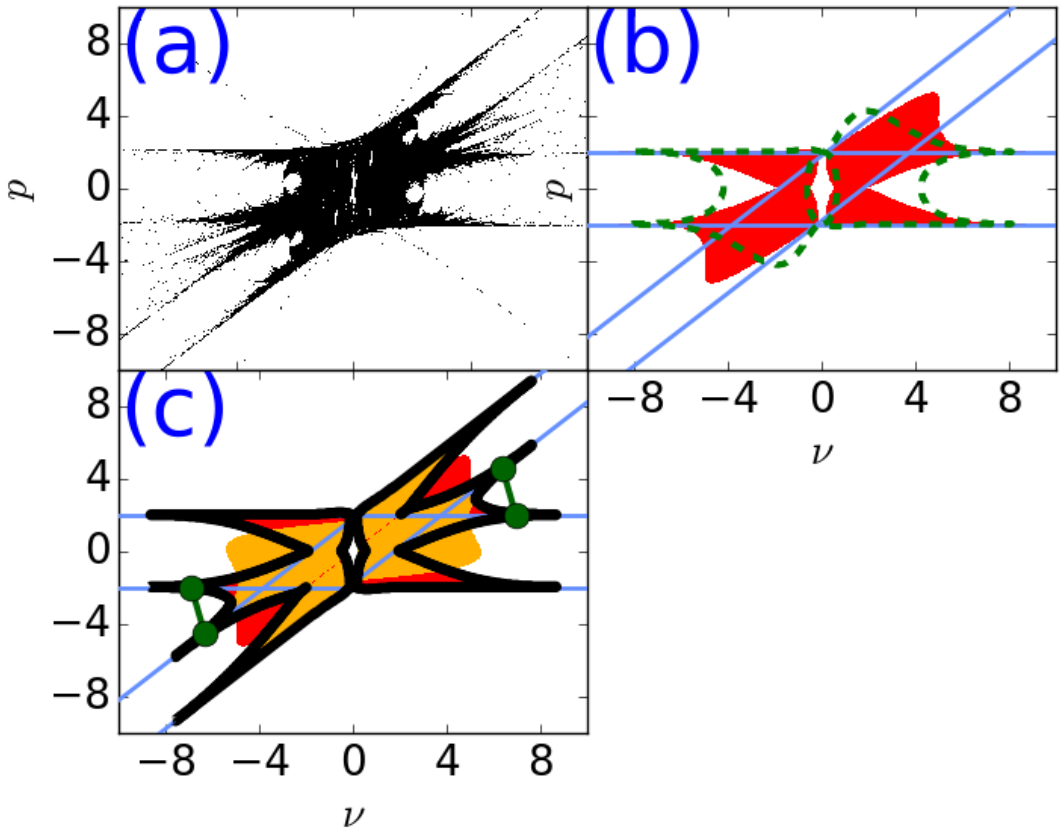

Figure 1.6. A more chaotic system: (a) Numerical double surface of section, for a system the same as in Fig 5, but ϵ_2 increased to 0.8. (b) The predicted chaotic region for the ϵ_1 resonance using the classical criterion (green outline) and the improved criterion (red region). (c) Chaos from both resonances: the improved criterion for the ϵ_1 resonance is in red, copied from panel (b), and that for the ϵ_2 resonance is overplotted in orange. The merged prediction is outlined in black. The green circles show the reduced classical criterion, now applied to both the ϵ_1- and ϵ_2- resonances.

In Figure 1.6(a)–(b), we repeat the study from Figure 1.5, but now with ϵ_2 increased from 0.1 to 0.8, in which case $\Delta p_{\rm chaos} = 3.6$. That is comparable to the width of the ϵ_1 resonance ($\Delta p = 4$), and so one expects the classical criterion to be inadequate. The numerical chaotic region is shown in panel (a), and it is now seen to be much larger than before. In fact, it agrees much better with the prediction of naive resonance overlap, i.e.,

with the analog of Figure 1.5(b) after increasing to $\epsilon_2 = 0.8$. That fact is generally true: naive resonance overlap works best when the widths of the two overlapping resonances are comparable (e.g., Shepelyansky, 2009).

In panel (b), we show the predictions from the classical criterion (the green dashed curves) and from the improved criterion (the red region). The red region is a much better match to the numerical result. In particular, the red region predicts that the chaos in the circulation zone roughly follows the ϵ_2-separatrix, whereas the classical prediction does not.

We turn now to the chaos of the ϵ_2 separatrix. To plot its improved kick criterion, we may reuse the prior results, but with the roles of the two resonances swapped. We proceed by first writing the Hamiltonian as

$$H(\phi_{sw}, p_{sw}, t) = p_{sw}^2/2 - \epsilon_2 \cos(\phi_{sw}) - \epsilon_1 \cos(r_{sw}(\phi_{sw} - \nu_{sw} t)) \ , \tag{1.18}$$

where the "sw" subscript means that those quantities are defined with the 1 and 2 indices swapped in Equations (A.8)–(A.11). We then use the chaos criterion to determine the chaos threshold in the p_{sw}-ν_{sw} plane. And finally, we map that into the p-ν plane via the transformation $p = p_{sw} + \nu_{sw}$ and $\nu = -\nu_{sw}$. For the system in Figure 1.6, the result is shown panel (c) in orange.

Finally, we must merge the red and orange regions, which we do as follows: we discard the red when it lies inside of the ϵ_2 resonance, because there the ϵ_2 resonance dominates the dynamics; and similarly, we discard the orange when it is within the ϵ_1 resonance. That procedure discards everything in the region where both resonances overlap (e.g., the red region in Figure 1.5(b)), which is incorrect: in that region, the stronger resonance

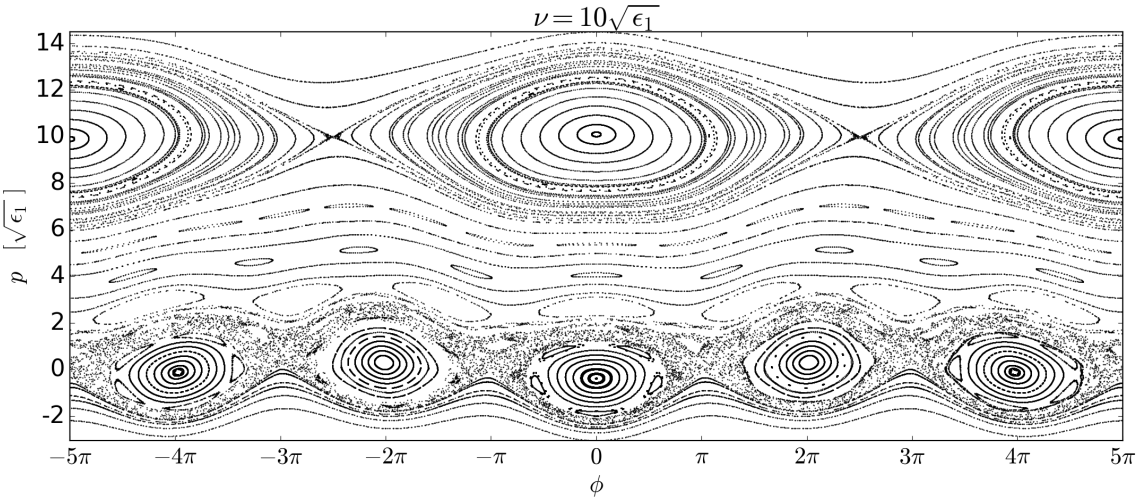

Figure 1.7. Surface of section of the perturbed pendulum, with the parameters of the 5:3–2:3 resonance crossing, and ν as shown.

dominates the dynamics. Therefore, if $\epsilon_1 > \epsilon_2$ we keep the red in the overlapping region, and, if otherwise, we keep the orange there. The resulting prediction is outlined in black in panel (c). It is seen to agree quite well with the numerical result.[7] We also show in panel (c) the green circles from the reduced classical criterion (Equation 1.12), but now for both of the resonances.

1.4.3. A Worked Example: The 5:3–2:3 Crossing

We use our prior results to predict the shape of the chaotic zone at the crossing between the 5:3 and 2:3 resonances in Figure 1.1. The resonant integers are $j_1 = 5$, $k_1 = 2$, $j_2 = 2$, and $k_2 = 1$, and hence $r = j_2/j_1 = 2/5$. The resonant strength from the inner planet is $\epsilon_1 = \mu_1 |C_1| \tilde{e}_1^2$ (Equations A.3 and Appendix A.2), where μ_1 is the planet-to-star mass ratio, $\tilde{e}_1$ is roughly the relative eccentricity between the test particle and the inner planet

[7]Panel (a) has more chaos near the center of the plot than predicted by panel (c). That is because when $\nu \sim 0$, chaos becomes adiabatic and needs to be treated differently (see, e.g., Shevchenko (2008)). However, this disparity is minor and we neglect it for the remainder of the paper.

(See Equation A.15 for the precise definition), and C_1 is the Laplace coefficient for the 5:3 resonance. For the parameters of Figure 1.1, $\epsilon_1 \approx 9.5 \times 10^{-7}$. A similar calculation yields $\epsilon_2 = \mu_2 C_2 \tilde{e}_2 \approx 3.3 \times 10^{-6}$. As explained in Section 1.3.1, ϵ_1 may be scaled out of the problem, in which case the strength of the perturbing resonance becomes ϵ_2/ϵ_1, i.e., only the relative strength of the two resonance determines which orbits are chaotic. For the present case, we have $\epsilon_2/\epsilon_1 \approx 3.5$. Although we retain dependencies on ϵ_1 in this subsection for completeness, the following results may be equally well understood by setting $\epsilon_1 \to 1$ everywhere.

Figure 1.7 shows a surface of section of Equation (1.1), when the height of the ϵ_2 resonance is $\nu = 10\sqrt{\epsilon_1}$. It differs from the one shown in Figure 1.3 in two notable ways. First, because $r = 2/5$ the ϵ_1-resonance now has five cat's eyes for every two of the ϵ_2-resonance. And second, the large value of ϵ_2/ϵ_1 produces the chaos of the ϵ_1-resonance even at this large separation.

Figure 1.8(a) is the numerical double surface of section, and panel (b) is the prediction of the improved kick criterion. For the prediction, the chaotic regions of both resonances have been merged, as for the black outlined region in Figure 1.6(c). The prediction agrees well with the numerical result. The green circles show the rough estimates from the reduced classical kick criterion—i.e., from Equation (1.16) for the topmost circle, and from the analogous equation for the rightmost circle, which marks the chaos of the ϵ_2 resonance. Also shown is the width of the ϵ_1-separatrix, $\Delta p = 4\sqrt{\epsilon_1}$.

The final step for comparing with Figure 1.1 is to transform Figures 1.8(a)-(b) to the PP plane. But before doing so, we must account for the initial resonance angles (ϕ_i and ψ_i), which are determined from the initial orbital elements via the expressions in footnote

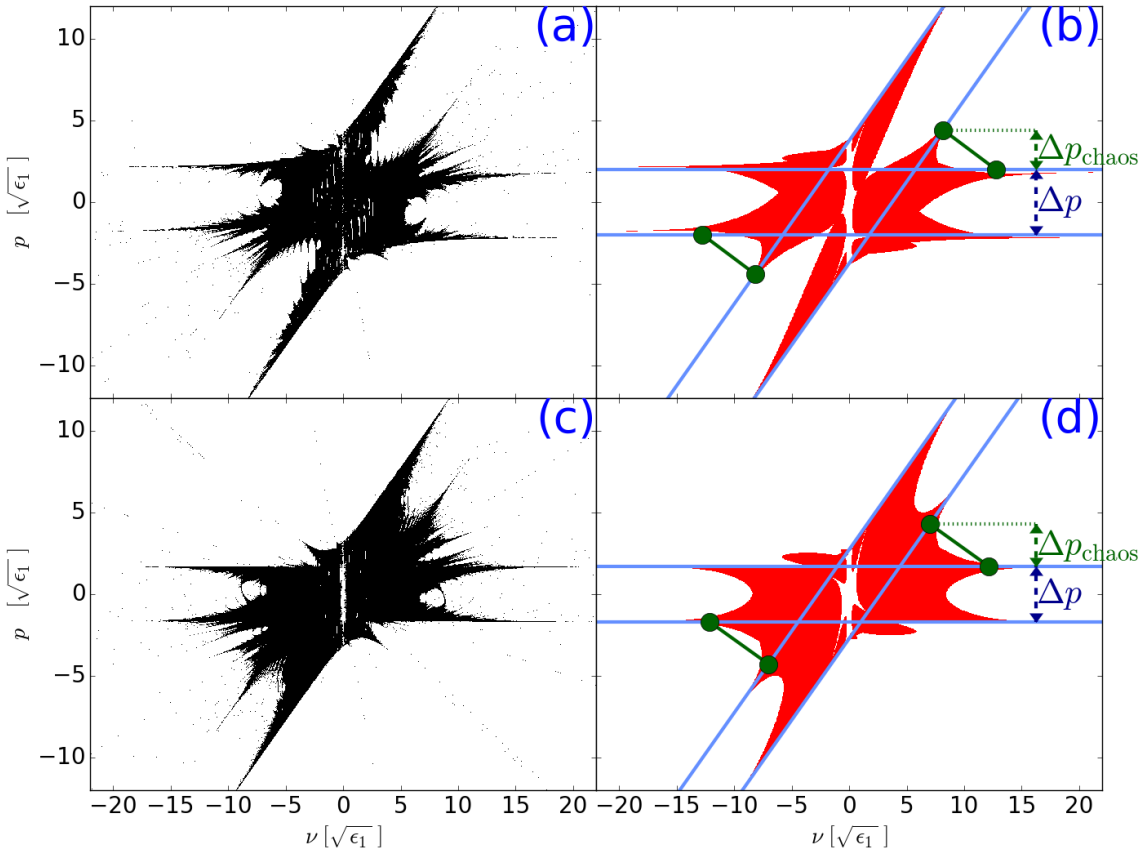

Figure 1.8. Double surface of section of the perturbed pendulum, with the parameters of the 5:3–2:3 resonance crossing. (a) Numerical result. (b) Prediction of the improved kick criterion (red) and estimate from the reduced classical criterion (green circles). (c) and (d) The same as (a) and (b), but now accounting for the initial resonance angles.

2 in Appendix A.1. We find $\phi_i \approx 1.1$ rad and $\psi_i \approx 4.8$ rad. By contrast, Figure 1.8(a) is initialized at $\phi_i = \psi_i = 0$ (see footnote 5). Therefore, panel (c) repeats panel (a), but now from integrations that start at the correct initial angles. Correspondingly, the prediction in panel (d) is determined as in panel (b), but, where we previously converted from $E \to p$ assuming $\phi = 0$, we now use $p = \sqrt{2(E + \epsilon_1 \cos\phi)}$. We use an analogous expression for the ϵ_2-resonance.

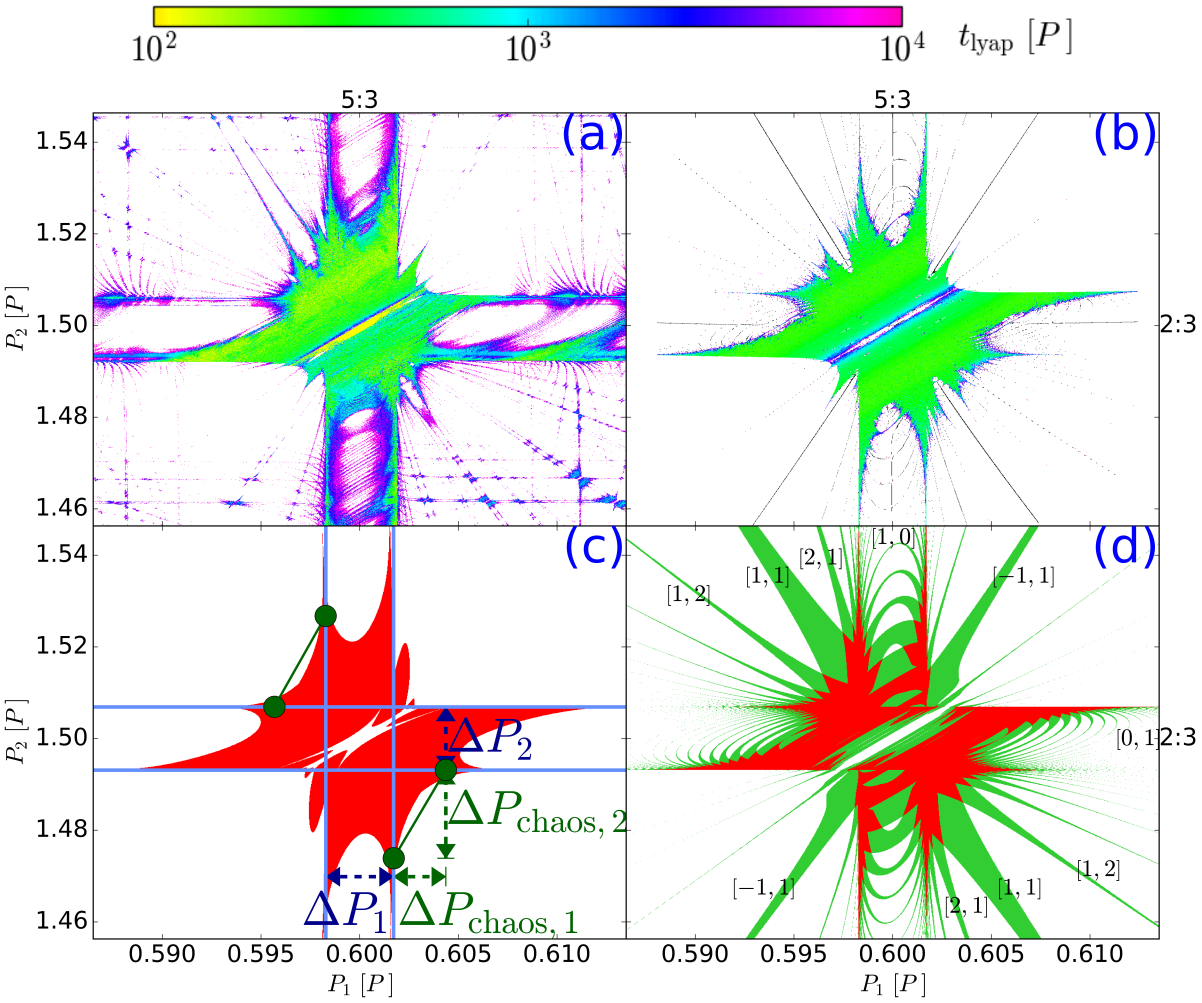

Figure 1.9. The 5:3–2:3 resonance crossing: (a) Lyapunov time in N-body simulations, in a zoomed-in region of Figure 1.1. (b) Lyapunov time in integrations of the perturbed pendulum model. This panel is the same as Figure 1.8(c) after a simple coordinate transformation, and after a change in the color-coding to indicate Lyapunov time. (c) The analytic prediction of the improved kick criterion for the chaotic region. (d) The location of (inflated) secondary resonances (green), and where they overlap (red).

Figure 1.9 shows the final result for this resonance crossing. Panel (a) repeats the N-body simulations of Figure 1.1, zoomed in to the 5:3–2:3 crossing. Panel (b) repeats the

numerical integration of the perturbed pendulum (Figure 1.8(c)), with two alterations: First, the coordinates are changed from p-ν to those of the PP plane via the linear transformation

$$\frac{P_1}{P} \approx \frac{j_1 - k_1}{j_1}(1 + \sqrt{3}\,p) \tag{1.19}$$

$$\frac{P_2}{P} \approx \frac{j_2 + k_2}{j_2}(1 + \sqrt{3}\,(p - \nu)) \ , \tag{1.20}$$

which follows from Equations (A.9) and (A.11) after expanding to linear order in p and ν. And second, the chaotic region is colored to show the Lyapunov time. Comparing panels (a) and (b) shows that the perturbed pendulum model explains the bulk of the N-body chaos, albeit not the very weak chaos with Lyapunov time $\gtrsim 10^3 P$. Panel (c) shows the prediction from the improved kick theory, which results from transforming the coordinates of Figure 1.8(d). The theory accounts for much of the structure seen in panels (a) and (b). Also shown in panel (c) are the widths of the resonances, and estimates of the chaotic extents. The width of the ϵ_1 resonance follows from $\Delta p = 4\sqrt{\epsilon_1}$, Equation (1.19), and from accounting for the initial phase ϕ_i as described above, which together imply

$$\frac{\Delta P_1}{P} = 4\sqrt{3\epsilon_1}\ \frac{j_1 - k_1}{j_1}\left(\frac{1 + \cos\phi_i}{2}\right)^{1/2} \ . \tag{1.21}$$

The extent of the ϵ_1 separatrix from the reduced classical criterion (Equation 1.16) is

$$\frac{\Delta P_{\mathrm{chaos},1}}{P} \approx \frac{\sqrt{3}}{2}\ \frac{j_1 - k_1}{j_1}\frac{\epsilon_2}{\sqrt{\epsilon_1}}\kappa(r) \ . \tag{1.22}$$

For brevity, we ignore the dependence on ϕ_i in the latter expression, which is appropriate when $\Delta P_{\rm chaos,1} \lesssim \Delta P_1$. For an average ϕ_i, the ratio of the widths is $\Delta P_{\rm chaos,1}/\Delta P_1 \sim 0.2\frac{\epsilon_2}{\epsilon_1}\kappa(r)$, which evaluates to 1.2 for this system. The extents of the ϵ_2 resonance and chaotic region follow similarly, yielding

$$\frac{\Delta P_2}{P} = 4\sqrt{3\epsilon_2}\ \frac{j_2+k_2}{j_2}\left(\frac{1+\cos\psi_i}{2}\right)^{1/2} \tag{1.23}$$

$$\frac{\Delta P_{\rm chaos,2}}{P} \approx \frac{\sqrt{3}}{2}\ \frac{j_2+k_2}{j_2}\frac{\epsilon_1}{\sqrt{\epsilon_2}}\kappa\left(\frac{1}{r}\right)\ . \tag{1.24}$$

The ratio of widths is $\Delta P_{\rm chaos,2}/\Delta P_2 \sim 0.2\frac{\epsilon_1}{\epsilon_2}\kappa\left(\frac{1}{r}\right) \approx 2.3$.

In sum, the improved kick criterion explains the overall shape of the chaos seen in panels (a) and (b). But it does not address the finer-scale structure. As we shall show in Section 1.5 much of that is explained by the overlap of secondary resonances. We show the final result in panel (d), but defer discussion of that panel to Section 1.5.4.

1.4.4. Many Crossings

We repeat the prior calculation for many more resonance crossings in Figure 1.1. Figure 1.10 shows the prediction of the improved criterion in red, for resonances up to tenth order. It reproduces the majority of the strong chaos seen in Figure 1.1, with Lyapunov time $\lesssim 10^4 P$. We also show the reduced classical criterion (green circles) for the largest resonance crossings. These show that the classical estimate is an adequate approximation. It improves upon the naive resonance overlap when the two resonances have different sizes.

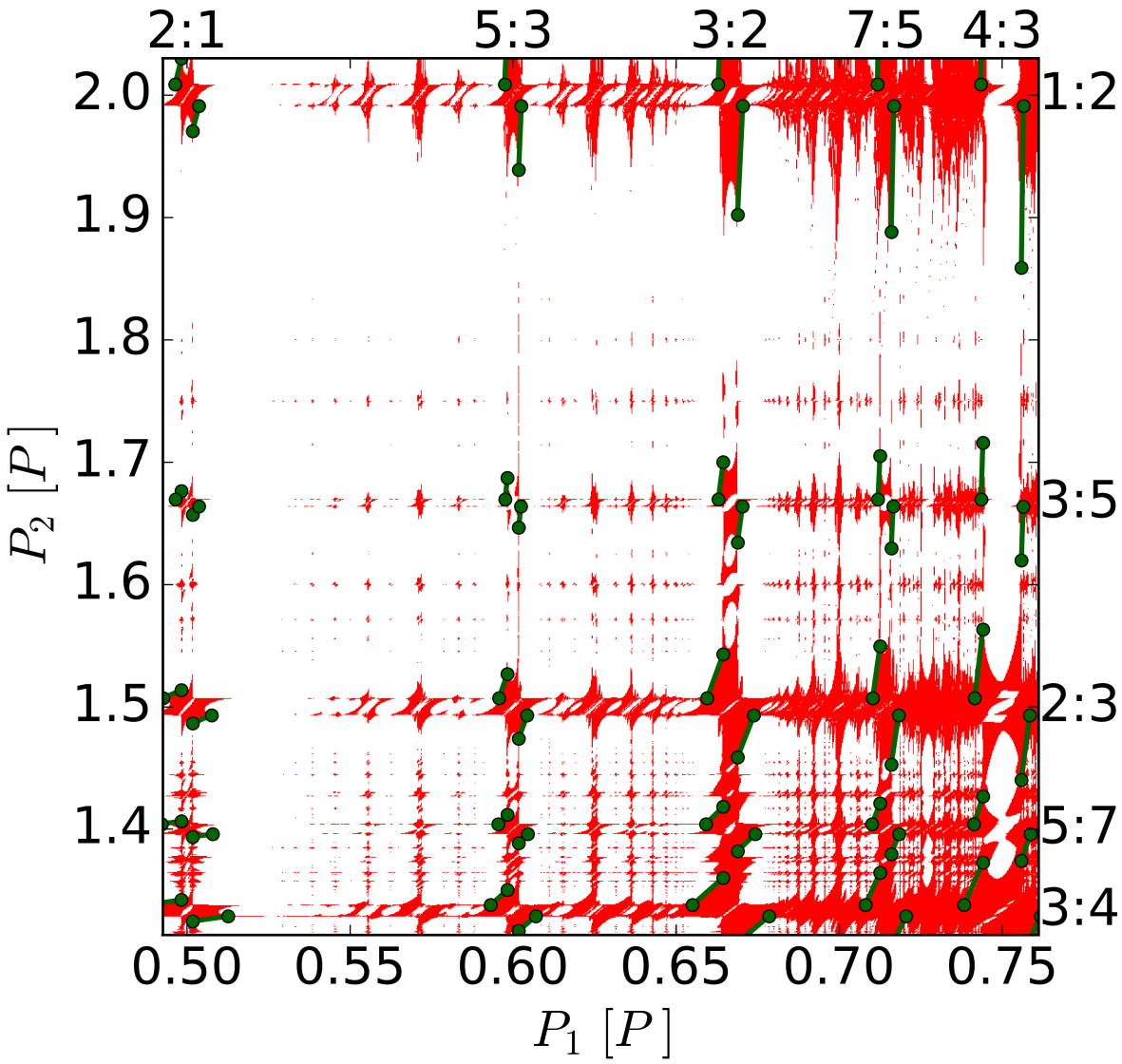

Figure 1.10. The red shaded region shows the prediction for where the chaos should occur in Figure 1.1, based on the improved kick criterion for resonances up to tenth order. The reduced classical prediction is shown as the green circles for resonances up to second order.

1.5. Theory of Overlapping Secondary Resonances

In surfaces of section such as Figures 1.4 and 1.7, one observes that new cat's eyes ("secondary resonances") appear when the two primary resonances are sufficiently close. These secondary resonances correspond to 3BRs in the orbital problem. Here, we work out their *locations* and *widths*. We also show that the overlap of neighboring secondary resonances reproduces the improved kick criterion. Finally, we use secondary resonances to estimate the Lyapunov times.

1.5.1. Locations and Widths of Secondary Resonances

We analyze the perturbed pendulum Hamiltonian (Equation 1.1) as in standard Hamiltonian perturbation theory (e.g. Lichtenberg & Lieberman, 1983). First, the unperturbed part is rewritten in action-angle variables (J, θ):

$$H_{\rm pend}(\phi, p) \equiv \frac{p^2}{2} - \epsilon_1 \cos\phi \quad \rightarrow H_{\rm pend}(J) \ . \tag{1.25}$$

Hamilton's equations for the unperturbed motion now read $J = \text{const}$, and $\dot{\theta} = \frac{dH_{\rm pend}}{dJ} \equiv \omega = \text{const.}$, where $\omega = 2\pi/\text{period}$.[8] And second, the effect of the perturbation on an unperturbed trajectory with given J is studied by expanding $H' = \epsilon_2 \cos\left[r(\phi - \nu t)\right]$ in a Fourier series in the angle, θ. Each term in the series will have a fixed frequency as the pendulum follows its unperturbed trajectory. In Appendix D, we show that the Fourier

[8]The inverse of the function $H_{\rm pend}(J)$ is given explicitly in Equation (1.3.10) in Lichtenberg & Lieberman (1983).

series is

$$H'(\theta, J, t) = \epsilon_2 \sum_{M=-\infty}^{\infty} c_M(J) \cos\left[M\theta + r(l\theta - \nu t)\right] \ , \tag{1.26}$$

where $l = 0$ when the unperturbed trajectory is in the libration zone, and $l = 1$ when it is in the circulation zone, and the Fourier coefficients are

$$c_M(J) = \frac{1}{2\pi} \int_{-\pi}^{\pi} \cos(r\phi_{\rm unp}(\theta, J) - (M + lr)\theta) \mathrm{d}\theta \ . \tag{1.27}$$

Note that we suppress functional dependencies on the parameters $(\epsilon_1, \epsilon_2, \nu, r)$. In the integrand of Equation (1.27), $\phi_{\rm unp}(\theta, J)$ describes the pendulum as it follows its unperturbed motion; it is the same function as appears in the kick criterion (Equation 1.5), except now we relabel its argument $t \to \theta = \omega t$, and we also make its dependence on J explicit. Equation (1.27) may be evaluated numerically, with $\phi_{\rm unp}(\theta, J)$ taken from Smith & Pereira (1978). An approximation for c_M that is valid near the ϵ_1-separatrix is derived in Equation (D.9) in Appendix D, and one valid far from the separatrix is provided in Appendix D of Escande (1985).

The perturbed pendulum Hamiltonian in action-angle variables is therefore $H(\theta, J, t) = H_{\rm pend}(J) + H'(\theta, J, t)$, without approximation. Each cosine term in the Fourier series for H' produces a secondary resonance. If we focus on a single M term, the Hamiltonian becomes

$$H(\theta, J, t) \approx H_{\rm pend}(J) + \epsilon_2 c_M \cos\left[M\theta + r(l\theta - \nu t)\right] \ . \tag{1.28}$$

The center of the resonance is where the argument of the cosine is stationary: $(M+rl)\dot{\theta}-r\nu=0$. After setting $\dot{\theta}=\omega$, as is valid to leading perturbative order, the Mth resonance occurs where the unperturbed pendulum has the frequency

$$\omega_M = \frac{r\nu}{M+lr} \ . \tag{1.29}$$

To understand Equation (1.29), consider first the case that the unperturbed pendulum lies in the circulation zone ($l=1$). Then the frequency of the ϵ_2 term in Hamiltonian (1.1) is $r(\dot{\phi}-\nu)\sim r(\omega-\nu)$. Equating that forcing frequency to an integer multiple of the unperturbed pendulum's frequency (ω) reproduces Equation (1.29) (when the integer is $-M$). Likewise, if the unperturbed pendulum lies in the libration zone, then the forcing frequency is $r(\dot{\phi}-\nu)\sim -r\nu$, because $\dot{\phi}$ averages to zero. Equating that to $-M\omega$ reproduces Equation (1.29) at $l=0$.

General secondary resonances of the Hamiltonian in Equation (1.1) have resonant angle in the circulation zone[9]

$$\Phi_{[M,N]} = M\phi + N\psi \tag{1.30}$$

for integers M and N. We call these $[M,N]$ resonances, in which case Equation (1.29) describes $[M,1]$ resonances. In a slight abuse of terminology, we shall also label the ϵ_1-resonance as the $[1,0]$ and the ϵ_2-resonance as the $[0,1]$.[10]

[9]Equation (1.30) is the resonant angle when the unperturbed ϕ and ψ are circulating. When the unperturbed ϕ is librating and ψ is circulating, the resonant angle is $(M-Nr)\phi+N\psi$.

[10]It is an abuse because the argument of the ϵ_2 cosine in the perturbed pendulum differs from that of the $M=0$ cosine term in Equation (1.26). The latter provides a slightly more accurate description of the ϵ_2-resonance; or, to be more precise, Equation (1.26) with $M=0$ incorporates not only the ϵ_2-resonance, but also its perturbation by the ϵ_1-resonance.

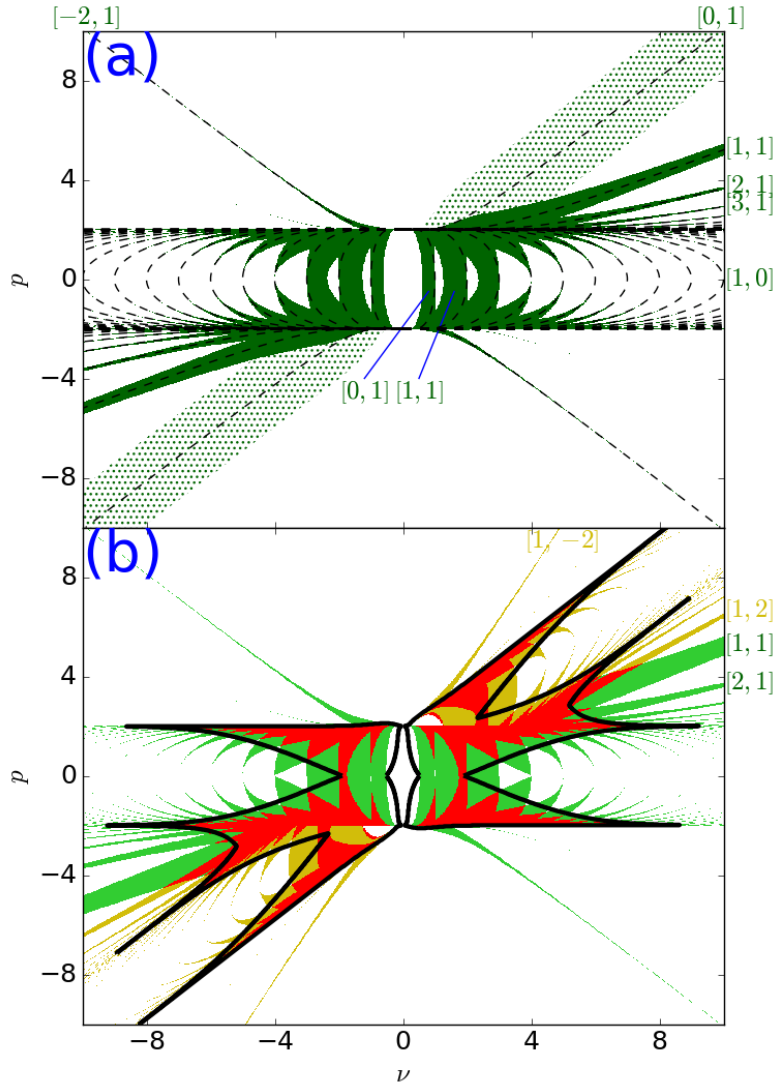

Figure 1.11. Overlap of secondary resonances leading to chaos, for a perturbed pendulum with the same parameters as Figure 1.6. (a) The locations of the $[M, 1]$ secondary resonances are shown as the black dashed curves, and their widths are shaded green. The $[0, 1]$ is stippled because we neglect it in determining where overlap occurs. (b) $[M, 1]$ secondary resonances (light green) are copied from panel (a), after inflating by $\pi/2$ and excluding the $[0, 1]$. The yellow shadings are the same for the $[1, N]$ resonances. The region where at least two secondary resonances overlap is shown in red. The black curve is the prediction of the improved kick criterion, copied from Figure 1.6(c).

Equation (1.29) determines the locations of the $[M, 1]$ resonances. To plot them in the p-ν plane, i.e., in the plane used for double surfaces of section, at each ν we use the properties of the unperturbed pendulum to convert from ω_M to energy E, and thence to the value of p at $\phi = 0$ (via $E = \frac{p^2}{2} - \epsilon_1$). The result is shown in Figure 1.11(a) as black dashed lines, for the same system as Figure 1.6.

We turn now to the widths of the resonances, which are determined by first Taylor expanding $H_{\rm pend}(J)$ in Equation (1.28) about J_M (the action corresponding to ω_M) which gives $H_{\rm pend} \approx {\rm const} + \omega_M(J - J_M) + \frac{1}{2} \left.\frac{{\rm d}^2 E}{{\rm d}J^2}\right|_{J=J_M} (J - J_M)^2$. The term linear in $J - J_M$ is removed by a canonical change of variables, and Equation (1.28) is turned into a simple pendulum by dividing through by d^2E/dJ^2 (and correspondingly rescaling time by the same factor). The full-width can then be read off:

$$\Delta J = 4 \left(\frac{\epsilon_2 c_M}{d^2E/dJ^2} \right)^{1/2} = 4 \left(\frac{\epsilon_2 c_M}{d\omega/dJ} \right)^{1/2} . \tag{1.31}$$

We use this expression to produce the green region in Figure 1.11(a), after inserting the exact $d\omega/dJ$ from Equation (4.3.29) of Lichtenberg & Lieberman (1983).

1.5.2. Chaos from Secondary Resonance Overlap

Chaos is postulated to occur where secondary resonances overlap with each other. In Figure 1.11(b), the overlapping region for the system in panel (a) is shaded red. That red region is made as follows: First, the green $[M, 1]$ secondary resonances from panel (a) are copied over, after inflating their width in ΔJ by $\pi/2$ and changing their color to light green (to indicate their inflation); the reason for the inflation will be discussed shortly. Second, the analysis that produced the light green region is repeated, but with the roles

of the ϵ_1- and ϵ_2- resonances swapped. That produces $[1, N]$ secondary resonances, in the notation introduced below Equation (1.29), which are shown in Figure 1.11(b) in yellow, after inflation.[11] The $[M, 1]$ resonances all lie to one side of the $[1, 1]$ resonance and the $[1, N]$ lie to the other. Finally, the region where at least two of the secondary resonances overlap is colored red.

In the above procedure, three of the resonances must be treated specially: the $[1, 0]$, $[0, 1]$, and $[1, 1]$. For the $[1, 0]$, we do not include its overlap with the green regions in calculating the red. That is because the ϵ_1-resonance is incorporated into H_{pend} in Equation (1.28), and that equation is integrable for a single M, i.e., two M's are needed for chaos. We also neglect the overlap with the $[0, 1]$ for the same reason. For the third—the $[1, 1]$—its width may be calculated in two ways, as it is both an $[M, 1]$ and a $[1, N]$ resonance. We choose it to be the $[M, 1]$ if the ϵ_1-resonance is stronger ($\epsilon_1 > \epsilon_2$); otherwise we choose it to be the $[1, N]$.

Also shown in Figure 1.11(b) is the prediction of the improved kick criterion (the black curve), which is copied from Figure 1.6(c). The two criteria (kick and overlap) are seen to largely agree, although the overlap criterion is spikier. Comparing with the numerical integration (Figure 1.6a), we see that most of the spikes in the numerical plot are attributable to overlapping secondary resonances.

Although the overlap criterion is more accurate than the kick criterion throughout most of the plot, in the center of Figure 1.11(c) overlap predicts less chaos; and in that

[11] To be more precise, the yellow regions are made by first defining the swapped quantities p_{sw}, ϕ_{sw}, etc., in which the 1 and 2 indices are swapped in their definitions (as described in Section 1.4.2.2). The locations and widths are then calculated in the p_{sw}-ν_{sw} plane, and that result is transformed to the p-ν plane via the transformation in Section 1.4.2.2. Note that in calculating the $[1, N]$ resonances, we take the unperturbed Hamiltonian to be the first and third terms in Equation (1.1), rather than Equation (1.28) with $M = 0$; although the latter is more accurate, we choose the former for simplicity.

region it is the kick criterion that is the more accurate, as may be seen by comparing with the numerical result. That is because resonance overlap is only accurate when the widths of the two resonances are comparable, as discussed in Section 1.2 and Section 1.4.2.2. And near the center of the figure ($|\nu| \lesssim 2$), neighboring resonances are ill-matched in size; e.g., at the value of ν pointed to by the $[0,1]$ label in panel (a), the $[0,1]$ has a large width in p, while the $[1,1]$ is squeezed into the edges of the ϵ_1-separatrix. One could, of course, improve on the overlap prediction by applying the kick method to two secondary resonances, or by considering the overlap of tertiary resonances (Escande & Doveil, 1981). But that lies beyond our scope.

1.5.3. Agreement With Improved Kick Criterion

Lichtenberg & Lieberman (1983) demonstrate analytically that the overlap and kick criteria agree with each other, subject to the approximations of the classical kick criterion. Here, we extend their analysis to the improved kick criterion. From Equation (1.29), resonances M and $M+1$ differ in their frequency by $\delta\omega \approx \frac{r\nu}{(M+lr)^2}$, when $M \gg 1$. That translates into a spacing in actions of

$$\delta J = \frac{r\nu}{(M+lr)^2} \left|\frac{\mathrm{d}J}{\mathrm{d}\omega}\right| \ . \tag{1.32}$$

Overlap between neighboring secondary resonances occurs when $\Delta J > \delta J$ where ΔJ is given in Equation (1.31),[12] i.e., when

$$16\epsilon_2 c_M > \frac{(r\nu)^2}{(M+lr)^4} \left|\frac{dJ}{d\omega}\right| \ . \tag{1.33}$$

[12]Strictly speaking, overlap occurs when the sum of the half-widths of adjacent resonances exceeds δJ. We ignore this subtlety because adjacent resonances have comparable widths when $M \gg 1$.

Setting $\frac{\mathrm{d}J}{\mathrm{d}\omega} = \frac{\mathrm{d}J}{\mathrm{d}E}\frac{\mathrm{d}E}{\mathrm{d}T}\frac{\mathrm{d}T}{\mathrm{d}\omega}$, $\frac{dE}{dJ} = \omega$, $\frac{dT}{d\omega} = -\frac{2\pi}{\omega^2}$, and ω to its resonant value (Equation 1.29) then yields

$$\left|\frac{dE}{dT}\right| < \frac{16}{2\pi}\epsilon_2 r\nu(M + lr)c_M \tag{1.34}$$

$$\approx \frac{4}{\pi^2}\epsilon_2 r^2\nu(\nu - \Delta p)A_{2r}[r(\nu - \Delta p)] \tag{1.35}$$

where in the approximation we set c_M to the form derived in Appendix D (Equation D.9), and for simplicity we specialize to the upper circulation zone and set $\epsilon_1 = 1$. Equation (1.35) reproduces the improved kick criterion (Equations 1.8 and 1.17), albeit with a numerical coefficient of $\frac{4}{\pi^2}$ instead of unity (as shown also in Lichtenberg & Lieberman, 1983).[13] This shows that the kick criterion and the secondary resonance overlap criterion produce essentially the same criterion for chaos.

1.5.4. The 5:3–2:3 Crossing

We return to the worked example in Section 1.4.3, the 5:3–2:3 crossing, for which we repeat the procedure leading to Figure 1.11(b), and then transform to the P_1-P_2 plane with Equations (1.19)–(1.20). The result is shown in Figure 1.9(d), where now we depict all of the (inflated) secondary resonances in light green. The overlap region (red) is very similar to the numerical chaotic region from the perturbed pendulum model (panel b), which in turn agrees moderately well with what is found in N-body integrations (panel a). The only place panels (b) and (d) disagree significantly is where there is a large disparity

[13]Such a disagreement is not surprising, because both criteria are only defined up to arbitrary order-unity factors. For this reason, we plot secondary resonances with widths inflated by $\pi/2$.

in resonance sizes, which occurs in the region within the 5:3 that is also outside the 2:3. A similar effect was seen in the previous example (Figure 1.11).

Much of the discrepancy between the two numerical results (panels a and b) may now be understood by comparing with panel (d). For example, the separatrix of the $[1,1]$ is chaotic throughout panel (a), and its chaos is evidently due to its intersection with horizontal and vertical lines that represent high-order 2 body resonances. Those resonances were excluded from the perturbed pendulum model. Many of the other secondaries in panel (a) are also chaotic, due to their overlap with 2-body resonances.

1.5.5. Three Body Resonances

Secondary resonances in the perturbed pendulum model give rise to 3BRs in the N-body problem.[14] Here we discuss their locations and widths in the PP plane. The 3BR resonant argument from an $[M,N]$ secondary is $M\phi+N\psi$, where for the previous example $\phi = 5\lambda - 3\lambda_1$ and $\psi = 2\lambda - 3\lambda_2$, and we neglect here the ϖ terms. The $[1,1]$ resonance is the largest secondary (see below). For the example, its argument is $\Phi_{[1,1]} = 7\lambda - 3\lambda_1 - 3\lambda_2$. Therefore, the location of the $[1,1]$ is determined by $\frac{d}{dt}\Phi_{[1,1]} = 0 \approx \frac{7}{P} - \frac{3}{P_1} - \frac{3}{P_2}$ (continuing to neglect the ϖ terms), i.e., it traces out the following curve in the PP-plane:

$$\frac{P_2}{P} = \frac{3}{7 - 3P/P_1} \ ,$$

which matches what is seen in Figure 1.9(a) and (d).

The width of an $[M,1]$ resonance is worked out by Escande (1985). We turn that into the 3BR width by inserting his Equation (D.16) for c_M into Equation (1.31), and then

[14]Not all secondary resonances are 3BRs. For example, if the two primary resonances involve the same two planets, then the resulting secondaries only involve two planet angles.

converting ΔJ to ΔP, which yields

$$\frac{\Delta P_{[M,1]}}{P} \approx \frac{\Delta P_1}{P}\sqrt{\frac{\epsilon_2}{\epsilon_1}}\left(\frac{\epsilon_1}{8E}\right)^{M/2}\Sigma\left(r,M\right) \tag{1.36}$$

to lowest order in ϵ_1/E, where $E = p^2/2 - \epsilon_1\cos\phi_i$, and ϕ_i is the initial phase (see Section 1.4.3); and $\Sigma\left(r,M\right)$ is given by Equation (D.17) of Escande (1985) (with $\Sigma(r,M) = \Sigma_r^M$ in his notation). Likewise, for the $[1,N]$ resonances,

$$\frac{\Delta P_{[1,N]}}{P} \approx \frac{\Delta P_2}{P}\sqrt{\frac{\epsilon_1}{\epsilon_2}}\left(\frac{\epsilon_2}{8E_{\rm sw}}\right)^{N/2}\Sigma\left(\frac{1}{r},N\right) \tag{1.37}$$

where $E_{\rm sw} = p_{\rm sw}^2/2 - \epsilon_2\cos\psi_i$, in terms of the swapped quantities described in footnote 11.

Of particular note is the dependence of the widths on ϵ_1 and ϵ_2, since those quantities are typically very small (of order μe^k; see Equation A.3). One might naively have expected the $[1,1]$ width to be $\sim\sqrt{\epsilon_1\epsilon_2}$, because it arises from the coupling of two MMRs, each with width $\sim\sqrt{\epsilon}$ (Equations 1.21 and 1.23). That would make the width extremely small. But Equations (1.36)-(1.37) show that there is an extra factor of E in the denominator, and that is typically of order ϵ_1 in the region of interest. Therefore the 3BR widths are not necessarily much smaller than those of the MMRs that generate them.

1.5.6. Many Crossings

For the fiducial system of Figure 1.1, the secondary resonances (i.e., 3BRs) are shown in Figure 1.12 in green. And the regions where they overlap are shown in red. Comparing to Figure 1.1, we see that the strong chaos is adequately predicted, and some of the finer structure is captured. Here, we consider also the overlap of secondary resonances from

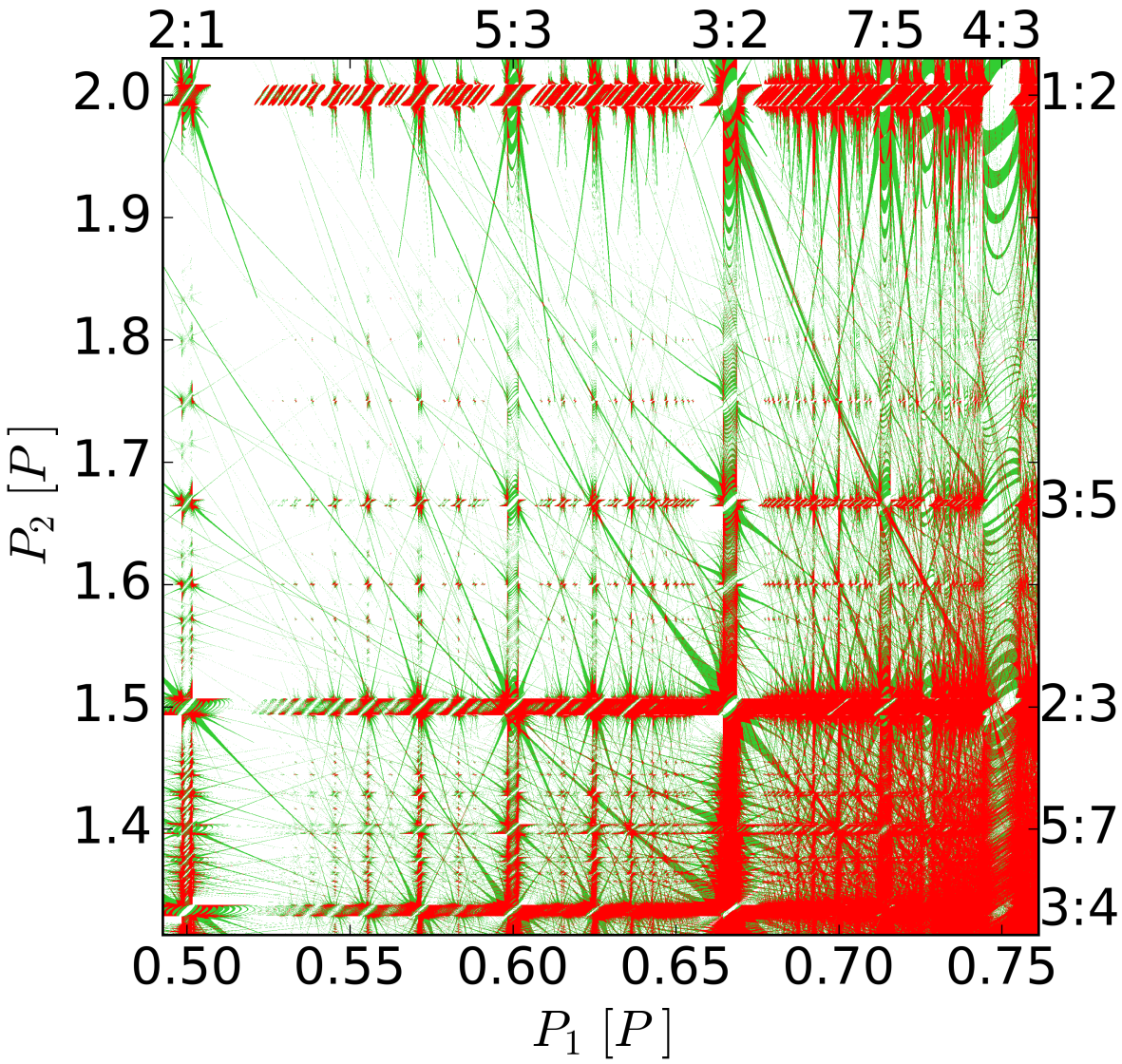

Figure 1.12. 3BRs (green) and their overlap (red) for our fiducial system. We show all 3BRs that are at least three pixels in width.

different two-body resonance crossings, which makes up a large portion of the chaos in the lower right of the figure. Secondary resonances also interact with primary resonances to produce chaos, but we omit such crossings because they are subdominant.

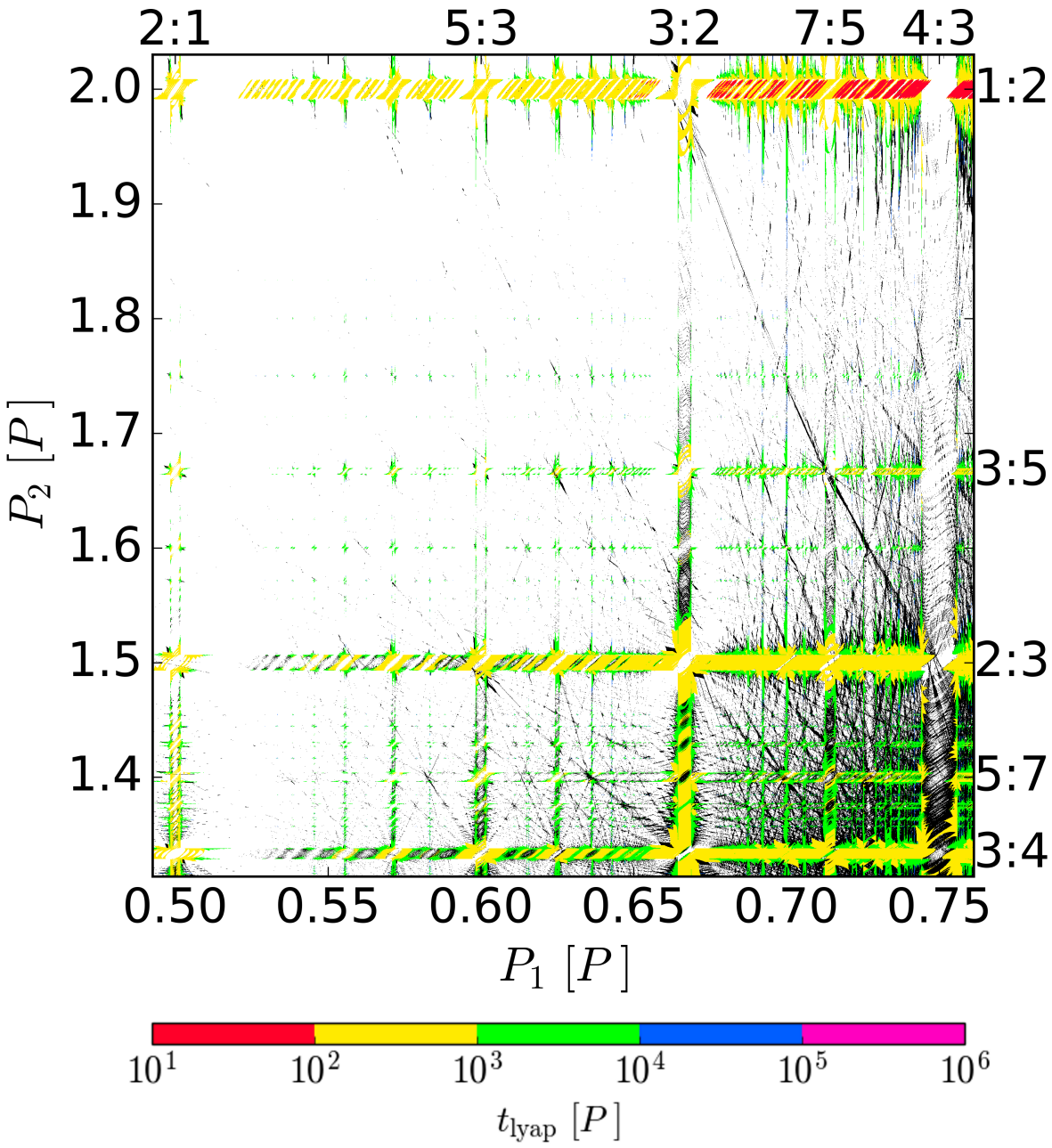

Figure 1.13. The predicted Lyapunov time based on overlapping secondary resonances. For two secondaries from the same 2BR crossing, the prediction is color-coded; but for two secondaries from different 2BR crossings, we are unable to make a prediction, and those overlaps are colored black.

We also use secondary resonances to estimate Lyapunov times. We do so in two steps: (i) we infer empirically an expression for the Lyapunov time in the perturbed pendulum model of Equation 1.1; and (ii) we apply that expression to pairs of overlapping secondary resonances. For step (i), a crude estimate of the Lyapunov time is the frequency of small oscillations in the stronger of the two resonances; for definiteness, we assume in the present discussion that $\epsilon_1 > \epsilon_2$, in which case the crude estimate is $t_{\rm lyap} \sim \epsilon_1^{-1/2}$. But we improve on that estimate by running perturbed pendulum simulations. These show that, for a given choice of the parameters r, ϵ_1, and ϵ_2, the Lyapunov time is roughly constant throughout the p-ν plane. Fitting the result to a power-law expression results in

$$t_{\rm lyap} \sim \frac{11}{\sqrt{r\epsilon_1}} \left(\frac{\epsilon_1}{\epsilon_2}\right)^{0.1} \quad . \tag{1.38}$$

We note that Shevchenko (2007) derives an expression for $t_{\rm lyap}$ analytically in his Section 3. His result is also $\propto (r\epsilon_1)^{-1/2}$, but has a different dependence on ϵ_1/ϵ_2. Additionally, he includes a dependence on ν, which we neglect.

For step (ii), we consider the overlap of neighboring secondaries, both of which come from the same 2BR crossing. In that case, the Hamiltonian is written as Equation (1.28), plus a second cosine term with $M \to M + 1$. We then rescale that Hamiltonian so that it is in the form of the perturbed pendulum model, except with new parameters (ϵ_1, ϵ_2, etc...), and apply the expression in Equation (1.38).[15] If there are multiple sets of overlapping resonances in the same location, we keep the most chaotic (the shortest Lyapunov

[15]We estimate Lyapunov times from the overlap of secondaries, rather than of primaries. Estimating them from primaries (i.e., assuming that the Lyapunov time is constant in the p-ν plane of the primary pair) provides a rough approximation to the true Lyapunov times. But a better approximation is obtained by estimating them from secondary resonance overlap, because the secondary overlap accounts for much of the fine structure within the primary pair's p-ν plane.

time). The resulting Lyapunov times are shown in color in Figure 1.13. One should also include the overlapping secondaries that come from two *different* 2BR. However, that calculation is beyond the scope of this paper; we merely color such overlapping secondaries black in Figure 1.13. Figure 1.13 shows an order-of-magnitude agreement with Figure 1.1 throughout much of the domain. While our estimate for the Lyapunov time is crude, the agreement shows that a simple model containing only 3BRs can reproduce the Lyapunov times found in the full N-body simulations. Additionally, the abundance of black in the lower right corner highlights the importance of overlapping secondaries from different 2BR crossings.

1.6. Discussion

1.6.1. Summary

Our principal results are as follows:

(1) We mapped out the chaos in the PP plane, for a fiducial three-planet system where the middle planet is converted to a test particle (Figure 1.1). As shown by Figure 1.2, resonance overlap is at best a crude guide for where chaos occurs.

(2) To improve upon resonance overlap, we first reduced the dynamics near an MMR crossing to a much simpler system with 1.5 degrees of freedom: the perturbed pendulum (Equation 1.1). The reduction, which is based on a novel approximation that combines many subresonances (Appendix A, Hadden (2019)), allows us to apply standard techniques from chaos theory to the planetary problem. The chaos map in the PP plane for a given MMR crossing was thereby reduced to

a double surface of section of the perturbed pendulum (e.g., Figures 1.5(a) and 1.9(a)-(b)).

(3) Two standard methods were applied to predict the chaotic zone. The first was kick theory (also known as the "separatrix map" or "whisker map"), which predicts the chaotic zone around each resonance. But that theory, as developed in the literature, is only adequate very near the separatrix. We therefore developed an improved kick criterion that applies further away (Section 1.4.2.2 and Appendix C). A highly simplified prediction for the extent of the chaotic zones in the PP-plane is provided by Equations (1.22) and (1.24). For our fiducial planetary system, we combined the results from many different MMR crossings in Figure 1.10, which agrees with Figure 1.1 considerably better than naive resonance overlap.

(4) The second standard method we applied was that of overlapping secondary resonances, or equivalently overlapping 3BRs (Section 1.5 and Appendix D). We developed an improved theory for the overlap, which parallels the improved kick theory, and showed that both of the improved theories agree with each other. Moreover, overlapping 3BRs account for much of the finer structure in the PP plane.

(5) We determined a semi-analytical expression for the Lyapunov time of the perturbed pendulum (Equation 1.38). We then applied that expression to adjacent secondary resonances to predict the Lyapunov times in the PP-plane (Figure 1.13). The result is in moderate agreement with Figure 1.1.

1.6.2. Validity of Key Assumptions

We assess the validity of our key assumptions:

(1) Massless middle planet: Making the middle planet massive should not introduce fundamentally new complications. For example, the reduction to a perturbed pendulum in Appendix A proceeds virtually unchanged. One complication is that whereas we only considered MMR crossings experienced by the middle planet, one must also consider crossings experienced by the inner and outer planets. But if the three planets have comparable masses, those crossings should be subdominant—because the strongest interactions should involve the middle planet. As a check, we repeated Figure 1.1, but with the middle planet having a mass of $12M_{\oplus}$ (Lissauer et al., 2011). We found very little difference from Figure 1.1, beyond the slight broadening and strengthening of the chaotic regions. A second complication with a middle massive planet is its effect on the secular evolution, as discussed below.

(2) Three planets: Based on the reasoning of the previous point, we do not expect additional planets to introduce significant novelties. To determine whether any planet is chaotic, one need only examine its MMRs with any two other planets.

(3) Coplanar planets: Allowing for modest inclinations should typically have little effect, because inclinations are weakly coupled to eccentricities. As a test, we repeated Figure 1.1 but with $i = e$ for each planet, and there was little difference to the figure. See also numerical experiments by Tamayo et al. (2021).

(4) Pendulum model for MMRs (see footnote 3): the pendulum approximation breaks down for first-order MMRs at low eccentricity ($e \lesssim \mu^{1/3} \sim 0.03$, where the latter

expression is for $10M_\oplus$ planets). In that case, the shape of the separatrix changes (Henrard & Lemaitre, 1983), and one would have to modify the two methods (kick and secondary overlap) presented in this paper to account for this change. That lies beyond the scope of this work.

(5) Neglect of secular effects: In adopting the pendulum approximation, we assume that the resonance strengths (ϵ_1 and ϵ_2) are constant, with values determined by the *initial* eccentricities. But secular evolution alters the eccentricities on a timescale of $\sim P/\mu$. Tamayo et al. (2021) show that one may account for that effect in a simple way: rather than using the initial eccentricity, one should use the maximum eccentricity as determined by secular evolution alone. Note that our fiducial system exhibits little secular evolution—because the massless planet has higher e than the other planets—and hence did not require such a correction. But where such a correction is required, it is straightforward to apply. An additional secular effect we neglect is chaos due to overlapping secular resonances. That could potentially lead to chaos on even longer timescales, as in the Solar System.

1.6.3. Comparison with Prior Work on Overlapping 3BRs

Petit et al. (2020), building on Quillen (2011) and Quillen & French (2014), determine a criterion for chaos in three planet systems from the overlap of 3BRs. In contrast to us, they assume the planets' orbits are circular, which allows for the planets to be much more closely spaced before chaos occurs. For example, for our fiducial example of Figure 1.1, they predict that the threshold for chaos for equal-spaced planets occurs at $P_1 \approx 0.88P$ and $P_2 \approx 1.14P$, which is beyond the range of Figure 1.1.

Nonetheless, it is instructive to compare their 3BRs with ours. Their 3BR locations are the same as those of the 3BRs that arise from the 1:1–1:1 crossing. The angles of the two MMRs are $\phi = \lambda - \lambda_1$ and $\psi = \lambda - \lambda_2$, and so the crossing produces 3BRs with the angle $(M+N)\lambda - M\lambda_1 - N\lambda_2$. In the PP plane, these 3BRs describe the curves $M\frac{P}{P_1} + N\frac{P}{P_2} = M + N$, all of which intersect the point $(P_1, P_2) = (1, 1)P$. Therefore those authors omit many of the 3BRs that we consider, as is appropriate at zero eccentricity. To determine the widths of the aforementioned 3BRs, Quillen (2011) considers the combination of two MMRs with angles $I_1(\lambda - \lambda_1)$ and $I_2(\lambda - \lambda_2)$, respectively, for integers I_1 and I_2. The subsequent papers by Quillen & French (2014) and Petit et al. (2020) incorporated an additional set of crossings into the width calculation: those from two 1st order MMRs, at integer combination $[M, N] = [1, 1]$, which is easily seen to produce the same 3BR arguments as the 1:1–1:1 crossings.

1.6.4. The Outer Solar System

Chaos in the outer Solar System has been attributed to 3BRs amongst Jupiter, Saturn, and Uranus (Murray & Holman, 1999). In Figure 1.14, we show the PP map for those three planets. We see that the strongest chaos in the vicinity of the true system is dominated by the crossing between the 5:2(Jup.-Sat.) and 1:3 (Sat.-Ura.), as well as the 3BRs that result from the $[1, 1]$ and $[2, 1]$ combinations of those two resonances. Nonetheless, the current system is close to—not inside of—those chaotic zones. Instead, we find that chaos appears to be more strongly affected by a very high order resonance between Jupiter and Saturn, as well as by a secular resonance. We note that the specific 3BR identified by Murray & Holman (1999) is the $[1, 1]$ combination that arises from the crossing of the

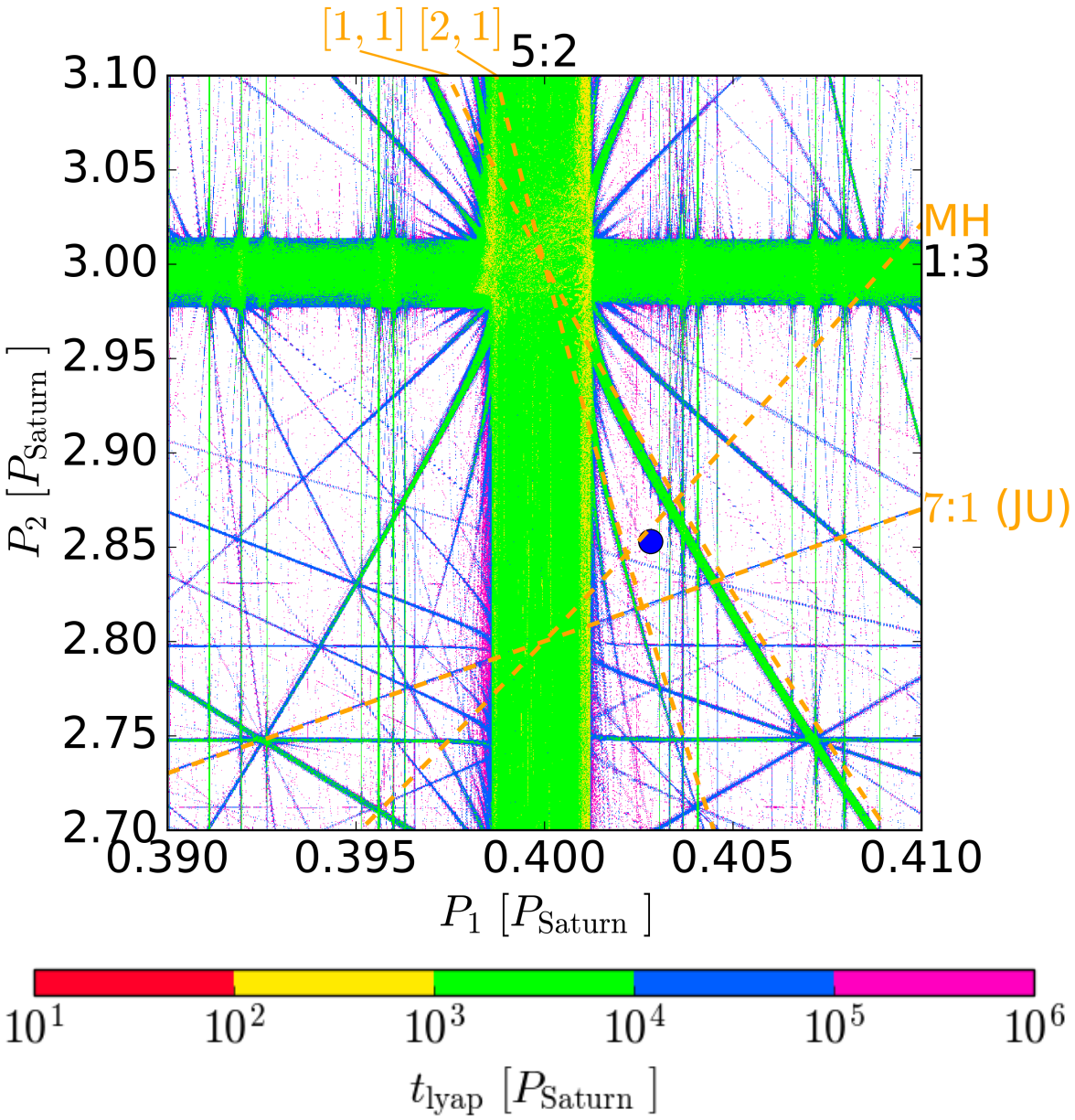

Figure 1.14. PP map for the Jupiter-Saturn-Uranus system. The parameters are from JPL's DE441 ephemerides (Park et al., 2021) evaluated at 2000 January 1. The blue dot indicates the true system. The orange dashed lines denote the nominal locations of various resonances: the one labeled MH is the 3BR proposed by Murray & Holman (1999); the ones labeled $[1, 1]$ and $[1, 2]$ are the corresponding $[M, N]$ combinations from the 5:2-1:3 crossing; and the one labeled 7:1 is a resonance between Jupiter and Uranus. The dashed lines do not correct for secular frequencies, which would shift the lines by a small amount ($\sim 0.001P$).

5:2(Jup.-Sat.) and the 1:7(Jup.-Ura.) (labeled MH on our plot). And although there is some chaos associated with the 1:7, there does not appear to be any chaos associated with the combination proposed by Murray & Holman (1999), even when we repeat Figure 1.14 at a significantly higher resolution. Additionally, in agreement with Guzzo (2005), we find that including Neptune does little to change the structure of Figure 1.14.

The Lyapunov time of the outer Solar System is very uncertain. Previous studies have found values ranging from 2 Myr (blue on our colormap) to 1 Gyr (white) (Hayes, 2007). Figure 1.14 shows that this is due to the fine-grained structure of the chaos in the vicinity of the true orbital elements (blue dot). Because there are additional effects which we neglect, e.g. those caused by the terrestrial planets, the location of the blue dot is only approximate. But its distance relative to the four key resonances (the orange dashed lines) is comparable to what is found by Guzzo (2005), who includes more effects. We defer a more careful analysis to future work.

CHAPTER 2

Warped Planet-Disk Interactions

2.1. Introduction

In the past decade, there has been an increasing number of warped protoplanetary disks (Marino et al., 2015; Stolker et al., 2016; Benisty et al., 2017; Debes et al., 2017; Long et al., 2017; Min et al., 2017; Casassus et al., 2018; Benisty et al., 2018; Muro-Arena et al., 2020; Ballabio et al., 2021). Benisty et al. (2017), for example, observe shadows on the disk, HD 100453, which they explain by the presence of an inner disk misaligned to the outer by $\sim 72^\circ$ blocking stellar light. Debes et al. (2017) infer a precessing inner disk by observing a brightness asymmetry rotate coherently over a 17 year span. Examples, such as these, have led many to speculate that the cause of such a misalignment is an unseen exoplanet. This raises the question: how massive must a planet be to cause a sufficient bend in a disk to explain the observations? To answer this, we must understand how warped disks interact with nearby planets.

Warped disks, typically in the context of a binary star system, have been studied extensively (Papaloizou & Pringle, 1983; Pringle, 1992; Papaloizou & Lin, 1995; Ogilvie, 1999; Lubow & Ogilvie, 2000; Ogilvie & Dubus, 2001; Facchini et al., 2013; Foucart & Lai, 2014; Zanazzi & Lai, 2018; Martin et al., 2019; Dullemond et al., 2022). Papaloizou & Pringle (1983) derived the equations for the tilt of a viscous accretion disk subject to an external torque in the diffusive regime ($\alpha \gg H/R$). Lubow & Ogilvie (2000), similarly,

derived the equations for the tilt in the wave regime ($\alpha \ll H/R$) (see also, e.g., Papaloizou & Lin, 1995). These equations make different assumptions, and are thus incompatible. Some attempts have been made to unify these equations (Martin et al., 2019; Dullemond et al., 2022). Martin et al. (2019) postulates a generalized set of equations that may work in both regimes, while Dullemond et al. (2022) derives from first principles a similar expression. Both sets of equations are tested only against the original equations and not against numerical simulations. However, Facchini et al. (2013) tests the prediction of the tilt from the equations of Lubow & Ogilvie (2000) against numerical simulation of a binary system and finds some cases where the theory agrees well, and other cases where there is some discrepancies. However, these studies have not aimed at understanding what happens if a planet is embedded in the disk, which is the primary goal of this paper.

Most of the work on inclined planet-disk interactions has focused on a large disk with a small planet (Tanaka & Ward, 2004; Cresswell et al., 2007; Bitsch & Kley, 2011; Rein & Liu, 2012; Arzamasskiy et al., 2018). Still, some work has looked at the massive planet case (Marzari & Nelson, 2009; Xiang-Gruess & Papaloizou, 2013; Bitsch et al., 2013; Zhu, 2019), but typically with other questions in mind (e.g., migration rates and inclination damping rates). Zhu (2019), however, does examine the bending question using theory and simulations. He derives a rough breaking condition, and finds agreement when compared with his simulations. However, his simulation results are not tested against any analytic theory, such the steady-state α-disk powerlaw surface density profile (Lynden-Bell & Pringle, 1974; Hartmann et al., 1998) or any of the warp equations. Still, his results are promising that embedded exoplanets can explain the misalignments in observed disks, and we seek to expand on it. To that end, we derive a set of equations governing the warp

in a disk, similar to those of Lubow & Ogilvie (2000). From those, we derive a bending criterion. Finally, we verify the warp equations and bending criterion with 3D numerical simulations.

The outline of this paper is as follows: We describe our background and perturbed system in Section 2.2.1. We give the time-dependent warp equations in Section 2.2.2, which are derived in Appendix E, and compare them to those of Lubow & Ogilvie (2000) in Section 2.2.3. Next, we characterize solutions in Section 2.2.4, and present the bending criterion in Section 2.2.5. The bending criterion itself is derived in Appendix F. Then we present our 3D simulations in Section 2.3. Finally, we summarize and discuss our conclusions in Section 2.4.

2.2. Warped Disks: Theory

2.2.1. Star-Planet-Disk System

We model a protoplanetary disk with an embedded planet orbiting a star. We use cylindrical coordinates, (R, ϕ, z), and align them to the orbit of the planet, i.e., the orbit of the planet is in the R-ϕ plane. We assume the mass of the disk is negligible, and that the planet mass, m_p, is much smaller than the mass of the star, $M_\odot$.

The disk is locally isothermal, i.e.,

$$c\left(r\right) = c_p \left(\frac{r}{R_p}\right)^q \ , \tag{2.1}$$

where $r = \sqrt{R^2 + z^2}$, R_p is the orbital radius of the planet, and q and c_p are parameters. The scale height of the disk is $H \approx c/\Omega_K$ where Ω_K is the Keplerian frequency. The disk

has a powerlaw density profile with a gap at the planet:

$$\Sigma\left(R\right) = \Sigma_{\rm sc}(R)\left(\frac{R}{R_p}\right)^p \quad , \tag{2.2}$$

where q is a parameter and $\Sigma_{\rm sc}(R)$,

$$\Sigma_{\rm sc}(R) = \begin{cases} \Sigma_{\rm gap} & |R - R_p| < \Delta_{\rm gap} \\ \Sigma_0 & \text{otherwise} \end{cases} \quad , \tag{2.3}$$

is our model for the gap.[1] Because we ignore self-gravity, the value of Σ_p is irrelevant, but only $\Sigma_{\rm gap}/\Sigma_0$ matters. We treat viscosity in our disk by the α-prescription (Shakura & Sunyaev, 1973), in which case viscous steady-state is achieved when $p + 2q = -1.5$ (Lynden-Bell & Pringle, 1974; Hartmann et al., 1998).

The planet is taken to be on a fixed, circular orbit, which we time-average to give

$$\Phi_p = \frac{m_p}{2\pi}\int_0^{2\pi} \frac{{\rm d}\phi}{\sqrt{R_p^2 + R^2 - 2RR_p\cos\left(\phi\right) + z^2 + h_s^2}} \tag{2.4}$$

as the potential where h_s is the softening radius. The softening radius is an ad-hoc way to remove the singularity at $R = R_p$ and $z = 0$. In the real system, the singularity is removed by the planet accreting material within some radius, but orbit averaging the planet potential precludes modeling this region of the disk. Additionally, time averaging the orbit means that the planet will not create a gap. We, therefore, model the gap with Equation (2.3) in our calculations of the warp equations, while our 3D numerical

[1]This model is unphysical.However, we find that any model that rapidly drops from $\Sigma_{\rm gap}$ to Σ_0 at the gap edges has the same outcome.

simulations will not have a gap. Taking this region into more detailed account–both in regards to the softening radius and a realistic gap–is beyond the scope of this work.

2.2.2. Governing Equations

We treat the warp in the disk as a linear perturbation to a flat, steady-state disk in the plane of the planet's orbit. The background state satisfies radial and vertical balance (Equations E.4 and E.5). The perturbation is a $m = 1$ linear warp governed by the linearly perturbed momentum and continuity equations (the steady state equations are Equations E.8-E.11, while time dependence is included in Appendix E.3). We reduce these equations by expanding the perturbed quantities in Hermite polynomials, i.e.,

$$X' = X'_0 \mathcal{H}_0\left(\frac{z}{H}\right) + X'_1 \mathcal{H}_1\left(\frac{z}{H}\right) + X'_2 \mathcal{H}_2\left(\frac{z}{H}\right) + ... \tag{2.5}$$

where $\mathcal{H}_n(z/H)$ is the nth Hermite polynomial, $X'_n = \frac{1}{n!}\langle \mathcal{H}_n\left(\frac{z}{H}\right) X' \rangle$, and

$$\langle(\cdot)\rangle \equiv \frac{1}{\sqrt{2\pi}H} \int_{-\infty}^{\infty} (\cdot) e^{-z^2/(2H^2)}\, \mathrm{d}z \ . \tag{2.6}$$

Then, we solve for the lowest order solution by neglecting higher order terms and eliminating v'_ϕ and ρ', leaving only v'_R and v'_z. Finally, we change variables to those similar to Lubow & Ogilvie (2000). For the entire derivation, see Appendix E. The resulting warp equations are

$$\frac{\partial G}{\partial t} + \left(\hat{\kappa}_0^2 - 1\right) \frac{i\Omega_0}{2} G + \alpha\Omega_0 G = \frac{\Sigma H^2 R^2 \Omega_0^3}{4} \left[(1 + 2i\alpha)\, R \frac{\partial W}{\partial R} + \frac{\mathrm{d}\ln c^2}{\mathrm{d}\ln r} \frac{\langle \frac{z}{H} \delta\Phi \rangle}{R^2\Omega_0^2} W \right] \ , \tag{2.7}$$

which we refer to as the "sloshing equation", and

$$\Sigma R^2\Omega_0\left[\frac{\partial W}{\partial t}+\frac{\langle\frac{z}{H}\delta\Phi\rangle}{R^2\Omega_0^2}\frac{i\Omega_0}{2}W+\frac{1}{4}\alpha R\Omega_0\frac{H^2}{R^2}\frac{\partial W}{\partial R}\right]=\frac{1}{R}\frac{\partial G}{\partial R}-\frac{3i\alpha G}{2R^2}\ , \tag{2.8}$$

which we refer to as the "angular momentum equation", where

$$W=-\frac{iv_{z,0}'^*}{R\Omega_0} \tag{2.9}$$

is the complex inclination,

$$G=\frac{1}{2}\Sigma H^2R^2\Omega_0\left(\frac{v_{R,1}'^*}{H}+\frac{v_{z,0}'^*}{R}\right) \tag{2.10}$$

is the internal torque (so called because of how it appears in Equation 2.8), an asterisk denotes the complex conjugate,

$$\delta\Phi=\left[R\frac{\partial\Phi}{\partial z}-z\frac{\partial\Phi}{\partial R}\right]\frac{R}{H} \tag{2.11}$$

Ω_0 is the orbital frequency evaluated in the midplane (Equation E.4), and

$$\hat{\kappa}_0^2=4+2\frac{\mathrm{d}\ln\Omega_0}{\mathrm{d}\ln R}\ . \tag{2.12}$$

is the square of the dimensionless epicyclic frequency in the midplane.

2.2.3. Comparisons

The warp equations are similar to those in Lubow & Ogilvie (2000), but with a three key differences:

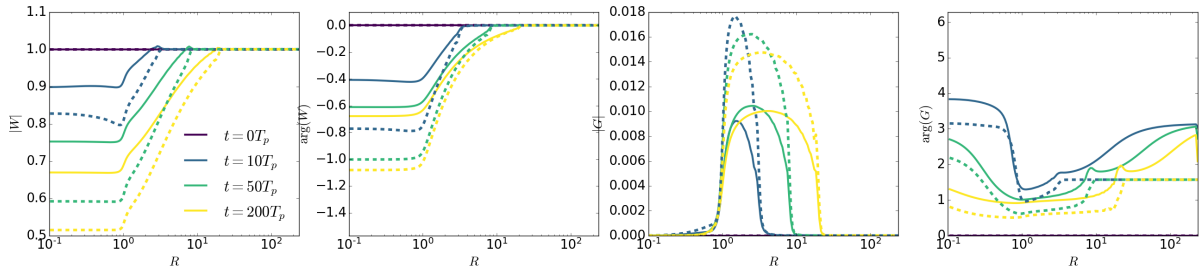

Figure 2.1. Results for $|W|$ (left), $\arg(W)$ (middle left), $|G|$ (middle right), and $\arg(G)$ from a time-dependent simulation of the warp equations. The parameters for the simulation are: $H = 0.1$, $\mu = 0.01$, $h_s = 0.1$, and $\alpha = 0.1$. The solid lines are from Equations (2.7) and (2.8), while the dashed lines are from Equations (A53) and (A54) of Lubow & Ogilvie (2000). The results are qualitatively similar, with the general difference being that the equations presented in this paper predict the planet to have a smaller effect on both W and G.

(1) The definition of the internal torque depends on v_r rather than v_R. Intuitively, this makes sense as a disk tilted to some inclination, but still flat, should have $G = 0$ which $G \propto v_r$ predicts.

(2) The planet's contribution to the angular momentum equation (Equation 2.8) is changed. However, our evaluation reduces to that in Lubow & Ogilvie (2000) when Taylor expanding about $z = 0$.

(3) We include more viscous terms, leading to three additional viscous terms in the final warp equations.

2.2.4. Solutions

To solve the time-dependent warp equations (Equations 2.7 and 2.8), we implement the numerical scheme described in Section 4 of Lubow et al. (2002). Our grid has $N = 150$ points logarithmically distributed over the computation domain, from $R = 0.1$ to $R = 250$, and $N_p = 50$ additional points within a few softening radii of the planet. W is taken

halfway between grid points, while G is taken at grid points. Each time step is split into two, where the viscous terms are evaluated at the original step, while non-viscous terms are evaluated at the half-step. For boundary conditions, we use the torque free condition for the inner boundary, which arises from angular momentum conservation at the boundary edge (Dempsey et al., 2020). For the outer boundary, we assume the disk is much larger than our numerical domain, where, outside, the disk is unaffected by the planet, and therefore flat with inclination $I_0 = 1$ and twist $\beta_0 = 0$. This corresponds to $W_{\rm out} = I_0 e^{i\beta_0}$, which we take as our second boundary condition. Correspondingly, we take Σ to be the viscous steady-state solution, such that neglecting $\frac{\partial \Sigma}{\partial t}$ is always valid. Though, we do allow for a parameterized gap at the planet (Equation 2.3).

One important fault with this integration scheme is that one term must be dropped due to a crippling instability: the viscous term proportional to $\frac{\partial W}{\partial R}$ in the sloshing equation (Equation 2.7). The instability occurs not only at the inner boundary, which would be solvable if it were the only issue, but also at $R = R_p$ where $\frac{\partial W}{\partial R}$ is largest. Therefore, all our time-dependent calulations drop this term. Qualitatively, this makes no difference and the general picture can be understood from the equations without the extra term. But it will make a quantitative difference when we compare to 3D simulations in Section 2.3.

We show a typical simulation in Figure 2.1. Very quickly (within a few orbits), the disk reaches a quasi-steady-state, where the inner disk has flattened at a smaller inclination and $G = 0$, the inclination rises and $|G| \sim$ constant from R_p out to some outer radius outside of which the disk is unchanged. The fact that the outer disk is unchanged validates our outer

boundary condition. Finally, this quasi-steady-state continues propagating outwards at roughly half the sound speed,[2] slightly decreasing the inner disk inclination as it does.

We now turn to characterizing steady-state solutions to the warp equations. We illustrate the effect of μ in Figure 2.2 by showing solutions for varying μ, while holding everything else fixed. Intuitively, a small planet mass cannot overcome the disk's pressure resisting bending. However, a large enough planet can overcome it and cause the disk to significantly bend. Comparing the timescales for the two mechanisms, $t_s \sim R_s/(H_p\Omega_0)$ for pressure flattening the disk and $t_p \sim R_s^2/(\mu_p\Omega_0 R_p^2)$ for the planet bending the disk, yields the classical bending criterion

$$\mu_{\mathrm{bend},c} \geq \frac{Hh_s}{R_p^2} \qquad \text{(classical)} \tag{2.13}$$

where the disk bends when the equality is satisfied (Larwood et al., 1996). For the case in Figure 2.2, the condition is matched for $\mu \sim 10^{-2}$, which is when a significant bend appears. If a gap in $\Sigma(R)$ is included at the planet, it will inhibit the disk's ability to resist bending, decreasing μ_{bend}.

Viscosity has the counter-intuitive effect, which we illustrate in Figure 2.3: rather than further resisting the effect of the planet as one would expect, it enhances the effect of the planet. This is accomplished by the inner part of the disk being able to further affect the rest of the disk through viscosity, smoothing out and extending the transition between the inner and outer disk. This has the ultimate effect of decreasing the inclination of the inner disk.

[2]The fact that the warp propogates at half the sound speed was derived by and generalized by Papaloizou & Lin (1995). Similarly, the dispersion relation for the warp equations makes the same prediction when $\Phi \approx \Phi_\star$ and $H/R \gg \alpha$.

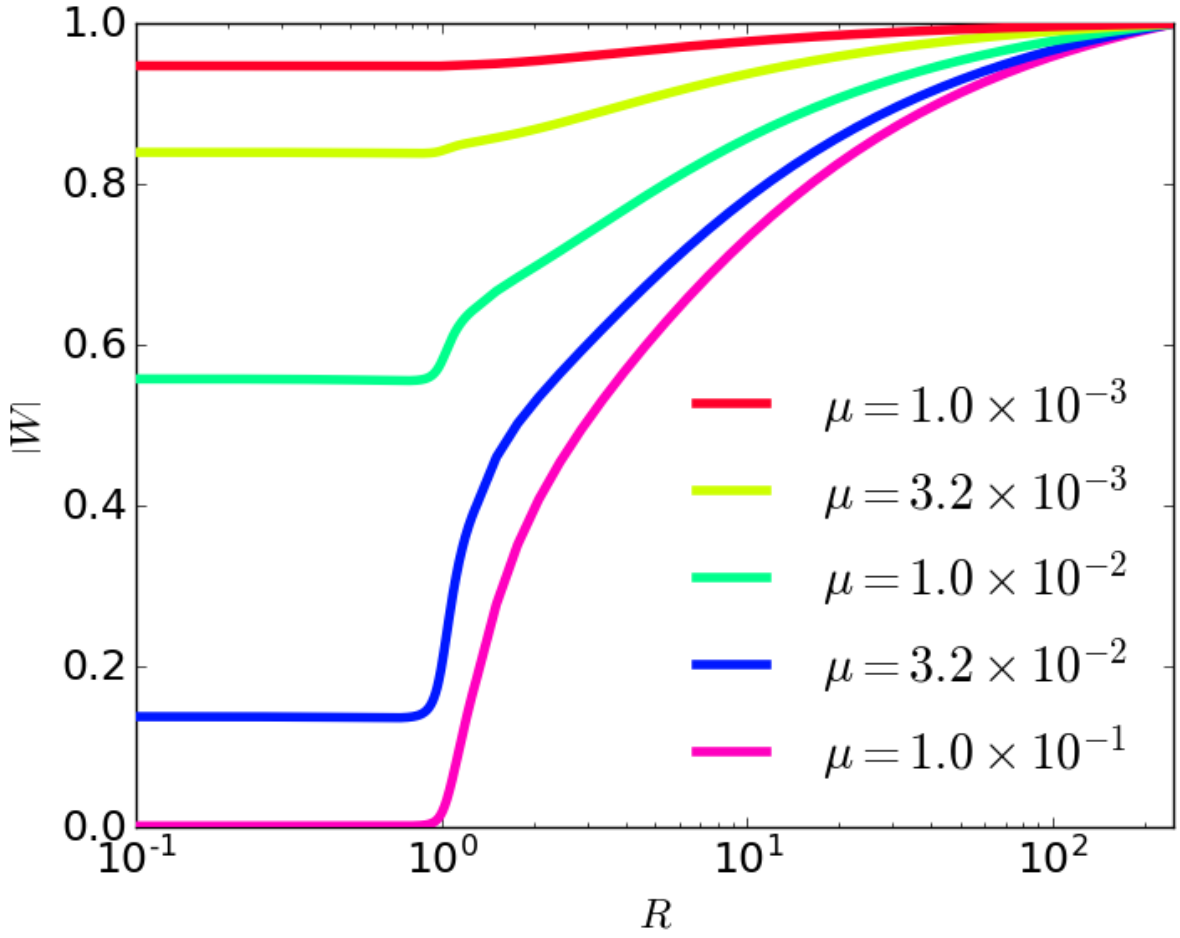

Figure 2.2. Steady state inclination profiles from warp equations (Equations 2.7 and 2.8) at steady-state, with $\alpha = 0$, $H = 0.1$, $r_s = 0.1$, and a few values of μ. Without viscosity, no twist in the disk develops. An order unity bend occurs when μ is somewhere between 10^{-2} and $3.2 \times 10{-}2$.

2.2.5. Bending Criterion

Now we answer the question: when will a disk develop a significant bend? We answer by deriving the change in inclination between the inner and outer disk, ΔW, using the perturbative approach of Foucart & Lai (2014), and determining when it is larger than the inner disk inclination, $W_{\rm in}$. See Appendix F, In the inviscid case, we find the disk

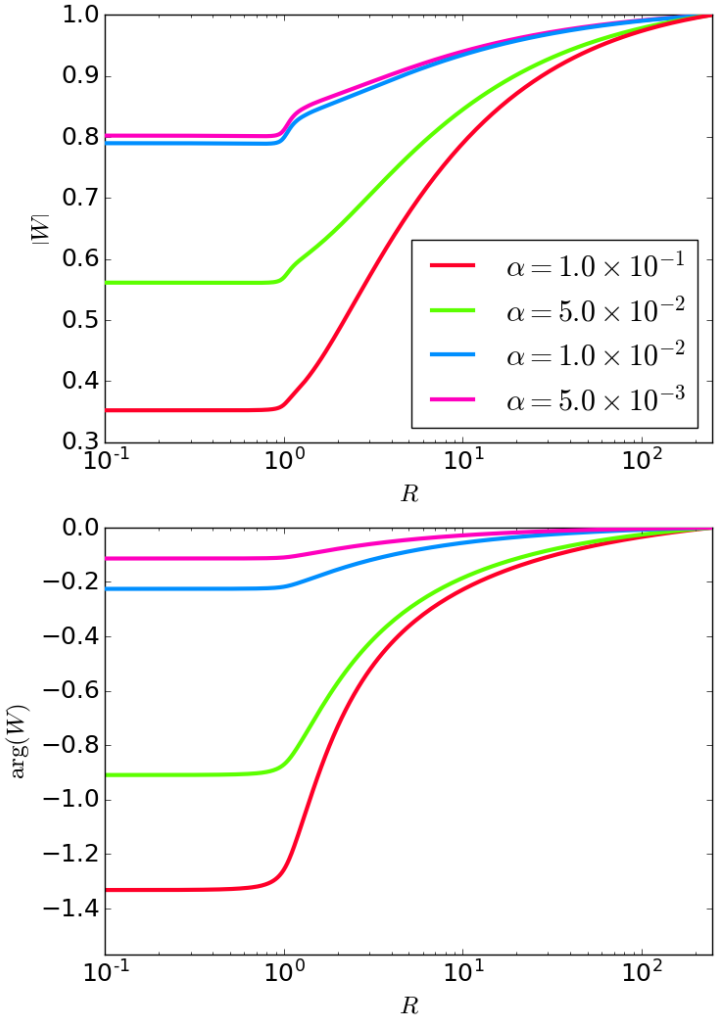

Figure 2.3. Steady-state inclination profiles from our equations (solid lines) and Lubow & Ogilvie (2000) (dashed lines), with $H_p = 0.05$, $m_p = 2.5 \times 10^{-3}$, $r_s = 0.1$, and a few values of α. Increasing α extends the influence of the planet, causing the inner disk to bend further and twist.

bends when:

$$\mu_{\rm bend,0} \gtrsim \begin{cases} \frac{H h_s}{R_p^2} & \text{(inviscid; shallow gap)} \\ \sqrt{\frac{\Sigma_{\rm gap}}{\Sigma_0} \frac{h_s \Delta_{\rm gap}}{R_p^2}} \frac{H}{R_p} & \text{(inviscid; deep gap)} \end{cases} . \tag{2.14}$$

In the shallow gap limit, this expression agrees with the classical criterion (Equation 2.13), and, in the deep gap limit, has the same dependence on $\Sigma_{\rm gap}$ as the breaking criterion[3] derived by Zhu (2019). However, when there is a gap, the disk becomes easier to bend as the gap prevents the pressure from as effectively resisting the planet's effect.

Additionally, we find a sufficiently large viscosity can make the disk more susceptible to bending. We find an additional criterion,

$$\mu_{\rm bend,\alpha}\alpha \gtrsim \begin{cases} \frac{H^2 h_s}{R_p^3} & \text{(viscous; shallow gap)} \\ \frac{\Sigma_{\rm gap}}{\Sigma_0}\frac{H^2}{R_p^2} & \text{(viscous; deep gap)} \end{cases} . \tag{2.15}$$

If either criterion is satisfied, we predict the disk to break. Typically, the inviscid criterion is sufficient, but, for a sufficiently small gap depth, $\mu_{\rm bend,\alpha}$ will become smaller than $\mu_{\rm bend,\,0}$. An example of this is shown in Figure 2.3, where inviscid bending criterion is not satisfied ($\mu_{\rm bend,0} = 5 \times 10^{-3}$), but, for $\alpha \gtrsim 0.1$, the viscous criterion is satisfied and, correspondingly, the numerical result has an order unity bend. Note, however, that in the case of protoplanetary disks, typically $H/R > \alpha$ and therefore $\mu_{\rm bend,\alpha}$ is only relevant if a deep gap is present. We illustrate $\mu_{\rm bend}$ as a function of $\Sigma_{\rm gap}$ in Figure 2.4, both from theory and numerical calculation. The numerical $\mu_{\rm bend}$ is found by a bisection algorithm on the steady-state versions of Equations (2.7) and (2.8), and agrees with the theoretical prediction to order unity.

[3]Note: our "bending" criterion is for when the inner disk has an order unity bend compared to the outer disk, while his "breaking" criterion is for when the inner and outer disks precess independently. Still, they are similar concepts.

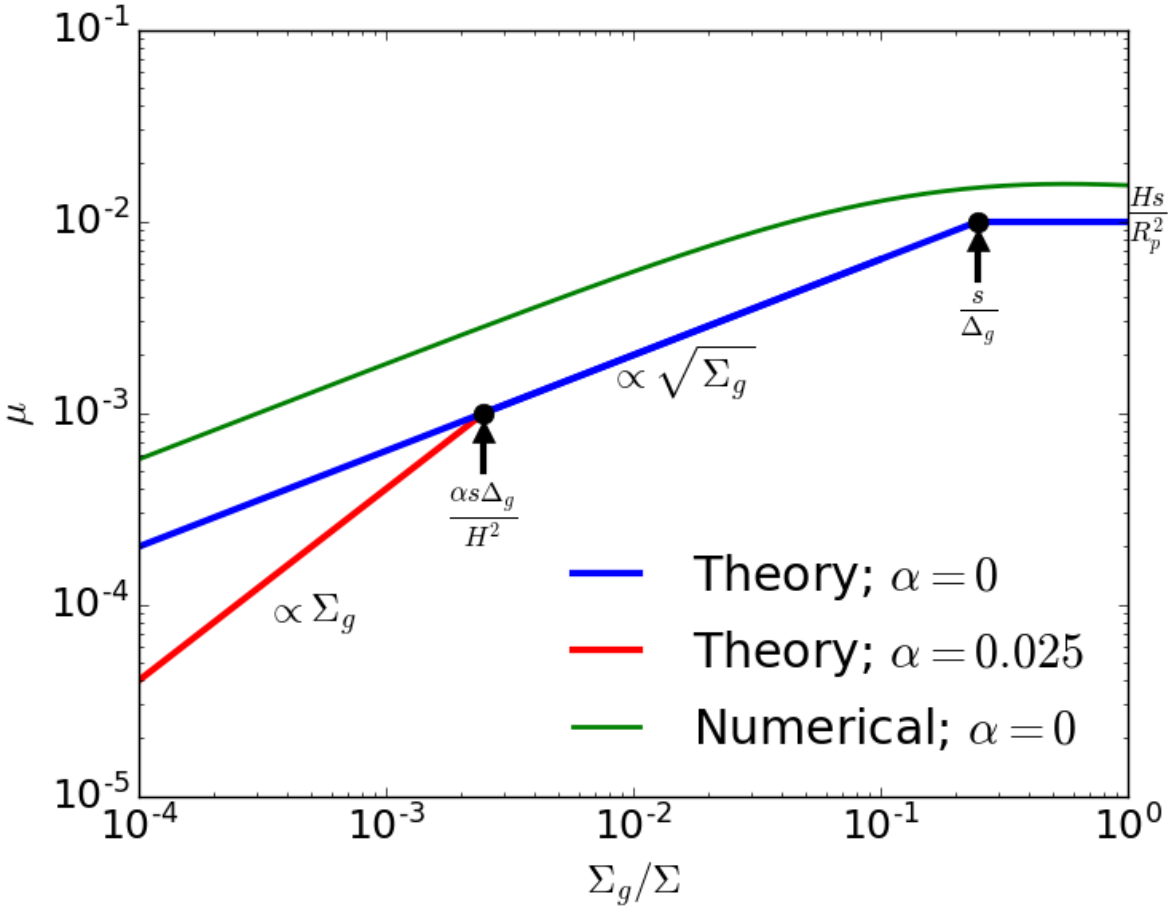

Figure 2.4. The theoretical (blue; Equation 2.14) and numerical (green) $\mu_{\rm bend}$ required for an inviscid disk to bend, which agree to a factor of unity. Additionally, the correction to $\mu_{\rm bend}$ from a small viscosity is illustrated in red.

2.3. Warped Disks: 3D Simulations

Our goal now is to verify the linear theory for warps presented in Section 2.2 using direct 3D numerical simulations. This is no easy task, however, as our background disk must be in viscous steady-state, which is difficult to achieve due to a timescale problem: the disk's viscous time t_ν is much longer than its dynamical time Ω^{-1}. As an unfortunate

result, simulation studies rarely contrast the viscous evolution of disks with theoretical steady-state solutions, such as the expected power-law profile. But there is another challenge in attaining the true solution: imperfect boundary conditions can introduce anomalous torques into the gas leading to an incorrect solution (e.g., see Dempsey et al., 2020). For example, the case of open inner and outer boundaries break angular momentum balance of viscous disks, forbidding the disk from reaching the power-law profile characteristic of the (planet-less) true steady state by artificially depleting mass at both boundaries.

To address the timescale problem, we initialize our simulations in viscous steady-state, neglecting the planet. This initial condition allows the disk to evolve on t_w, which is much shorter than t_ν. To solve the boundary problem, we implement torque free boundary conditions (Dempsey et al., 2020). This allows us to run simulations which match the theoretical models presented in Section 2.2.

2.3.1. Numerical Setup

We defer a complete description of our setup to Appendix G, but here provide a brief summary: We use the AREPO code (Springel, 2010; Pakmor et al., 2016) in its Navier-Stokes version (Muñoz & Lai, 2016). We initialize a locally isothermal disk in near steady-state with $q = -1/2$ (Equation 2.1). That is, $\boldsymbol{v}$ and ρ are given by radial and vertical balance (Equations E.4 and E.5) and $\Sigma(R)$ is given by Equation (2.2) with $p = -1/2$. The disk begins with and is kept at a resolution of roughly 250 azimuthal cells near the planet, and 100 in the rest of the disk. Finally, we rotate the disk to $I = 1^\circ$ and $\beta = 0^\circ$.[4] The

[4]This angle is, admittedly, very small; however, we tested for $I = 10^\circ$ found no change for the inclination profile, while a change appeared when $I = 30^\circ$.

star is included as a fixed point source with a spline softening for $r < 0.1R_p$ (e.g., Springel et al., 2001), while the planet's force, dependent on μ and h_s, is pre-calculated on a grid and linearly interpolated. The inner boundary condition is torque-free (Dempsey et al., 2020), and the disk is large enough such that the outer boundary condition is irrelevant.

Measuring $v'_{z,0}$ and $v'_{R,1}$ from the simulations is nontrivial as AREPO does not have a regular grid. Examining v'_z, we note first that

$$v'_z = \frac{1}{\pi}\int_0^{2\pi} v_{z,T} e^{-i\phi} \mathrm{d}\phi \tag{2.16}$$

gives the $m = 1$ component of v_z where $v_{z,T}$ is the total vertical velocity. $v'_{z,0}$ is defined as

$$v'_{z,0} = \frac{1}{H}\int_{-\infty}^{\infty} v'_z \psi \ \mathrm{d}z \ . \tag{2.17}$$

To perform the integral, we insert Equation (2.16) and integrate in R, giving

$$v'_{z,0} = \frac{1}{\pi R \Delta R H} \sum v'_{z,T} e^{-i\phi} \psi \delta V \ , \tag{2.18}$$

which is now in a usable form. We apply the same process for $v'_{R,1}$. From those, we calculate W and G, using the theoretical values of H and Ω, but calculating Σ directly from the simulation.

2.3.2. Results

Figure 2.5 shows W and G from nine AREPO simulations. The first row shows them as a function of time for the example in Figure 2.1, with the warp equations overplotted. There is reasonable agreement between theory and simulation: The overall shape of both

variables is matched well as they evolve in time, with the one exception being $\arg(G)$. While W and $|G|$ are insensitive to the method by which they are computed, $\arg(G)$ is very sensitive. It is thus difficult to determine if the disparity is due to the method we calculate G, resolution in the simulation, or an actual problem in the theory. The remaining variables have a small disparity between theory and simulation, which will be addressed momentarily. Nonetheless, the general picture described in Section 2.2.4 is matched: the inner disk quickly flattens to a lower inclination, and then the disturbance propagates outward as a quasi-steady-state. This allows us to compare the remaining simulations to the steady-state equations so that all the viscous terms can be included.

In the remaining rows, we vary one parameter of the disk or planet at a fixed time ($T = 100T_p$), and compare it to the steady-state equations.[5] As the equations assume steady-state, they are only valid roughly to where the wave has propagated. The varied parameters are, in order, μ, α, and H. We see that, in all cases, the general picture still holds true. Furthermore, the bending criterion presented in Section 2.2.5 is satisfied for $\mu = 0.01$ in the first row, $\alpha = 0.2$ in the second row, and $H = 0.05$ in the final row. These are the only simulations where $W_{\rm in} \lesssim 0.5$ validating the bending criterion. The only simulation wherein there remains noticeable disagreement between theory and simulation is when $\alpha = 0.2$, which is likely due to approximation that $\alpha \ll 1$ has started to break down.

Overall, we find good agreement between simulations and the warp equations, as well as the bending criterion. The primary observable, $W_{\rm out} - W_{\rm out}$, is well predicted in each

[5]For the steady-state equations, we use the Σ profile from AREPO and, because the overall scaling is arbitrary, normalize to $r = 5$.

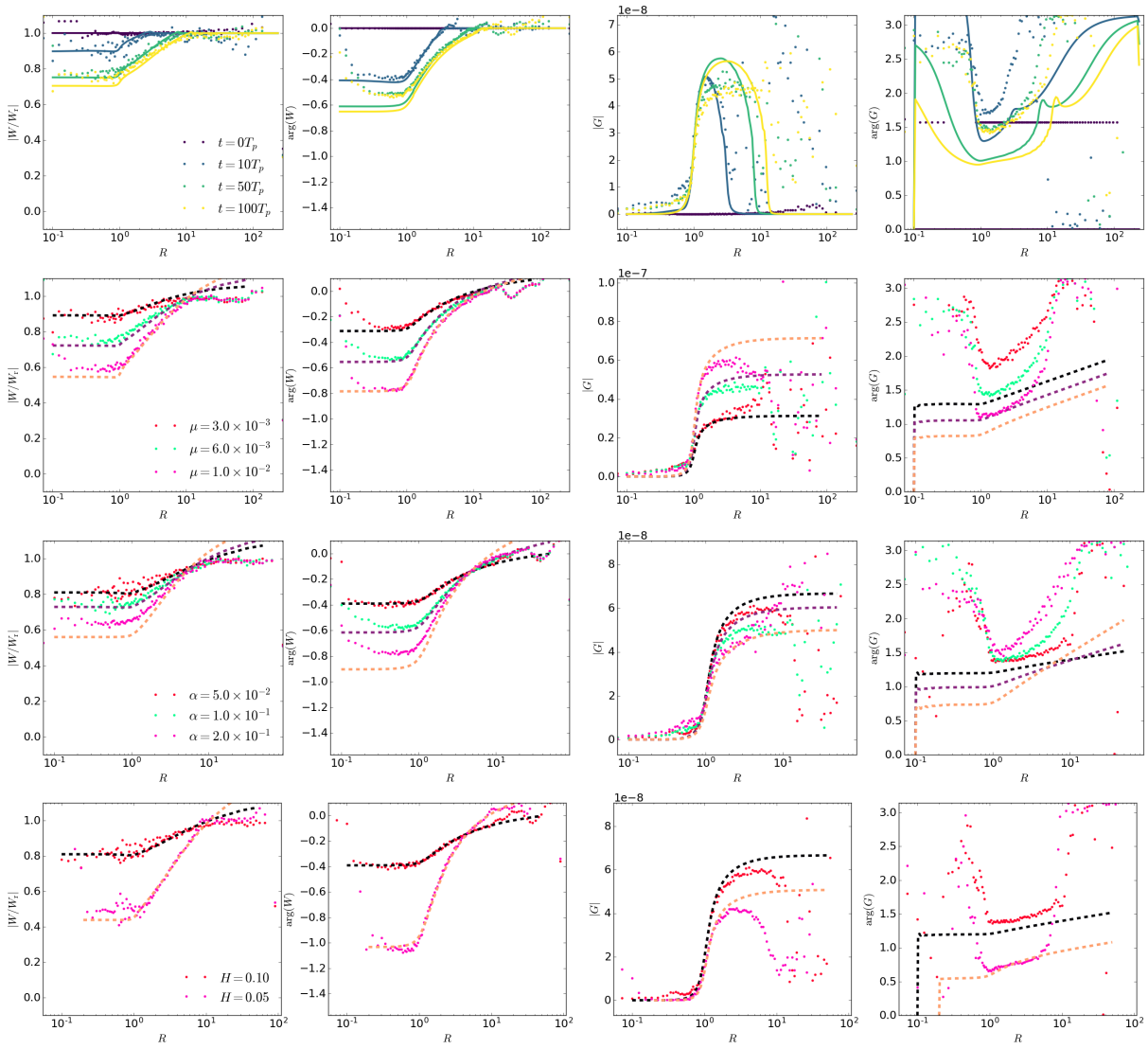

Figure 2.5. First row: W and G from an AREPO simulation at several times for the parameters in Figure 2.1 ($H = 0.1$, $\mu = 6 \times 10^{-3}$, $h_s = 0.1$, and $\alpha = 0.1$). There is acceptable agreement between the analytic theory and the AREPO simulation. The remaining three panels show AREPO while varying one variable compared to the steady-state equations. The second row varies μ, the third varies α, and the final varies H. Across all three rows (except when the panel indicates otherwise), $\mu = 0.01$, $H = 0.1$, $T = 100T_p$. The second row has $h_s = 0.1$, while the third and fourth have $h_s = 0.2$.

case. Likewise, the qualitative picture of a quasi-steady-state propagating outwards at half the sound speed holds true.

2.4. Discussion

2.4.1. Summary

Our principal results are as follows:

(1) We derived from first principles the equations that describe a warp in a disk in the presence of a star and orbit averaged planet (Equations 2.7 and 2.8; derived in Appendix E). These equations are an improvement upon those in literature, as they correct the definition of the internal torque, include a modified form of the potential, and better take into account viscosity.

(2) In Sections 2.2.4 and 2.2.5, we characterized the solutions to the warp equations as a function of time (Figure 2.1): a quasi-steady-state of a flat inner disk, transition region, and a flat outer disk. Likewise, we examined the role of each parameter (Figures 2.2 and 2.3), and determined a criterion (Equations 2.14 and 2.15; derived in Appendix F) for when the disk bends.

(3) We derived a bending criterion in the inviscid (Equations 2.14) and very viscous limits (Equation 2.15) in Appendix F, which is described in Section 2.2.5 and portrayed in Figure 2.4. In the inviscid shallow gap limit, the criterion matches the classical criterion (Equation 2.13). Likewise, it matches that of Zhu (2019) for the inviscid deep gap limit.

(4) Finally, in Figure 2.5, we compared the warp equations to 3D simulations performed in AREPO for various parameters, and found good agreement.

2.4.2. Key Approximations

The principal approximations made throughout this work are:

(1) We orbit averaged the planet's potential. This allowed us to treat the planet as an axisymmetric potential, greatly simplifying the problem. However, this introduced the unphysical softening radii, as well as requiring us to model the gap in the disk. We expect the case of a full planet will be similar to the one examined here, but dealing with that case is beyond the scope of this work.

(2) Everywhere we assumed that both $H/R \ll 1$ and $\alpha \ll 1$. This is likely the case for protoplanetary disks, but applying the warp equations to other contexts may violate these assumptions.

(3) We neglected $\frac{\partial \Sigma}{\partial t}$. Typically, this is considered equivalent to assuming $\alpha \ll H/R$, limiting our results to the wave regime. Alternatively, we assume the background disk is in viscous-steady state. This ensures $\frac{\partial \Sigma}{\partial t} = 0$, allowing Equations (2.7) and (2.8) to apply in both the wave and diffusive regimes.

References

Arzamasskiy, L., Zhu, Z., & Stone, J. M. 2018, Monthly Notices of the Royal Astronomical Society, 475, 3201, doi: 10.1093/mnras/sty001

Ballabio, G., Nealon, R., Alexander, R. D., et al. 2021, Monthly Notices of the Royal Astronomical Society, 504, 888, doi: 10.1093/mnras/stab922

Batygin, K., Deck, K. M., & Holman, M. J. 2015a, Astronomical Journal, 149, 167, doi: 10.1088/0004-6256/149/5/167

Batygin, K., Morbidelli, A., & Holman, M. J. 2015b, The Astrophysical Journal, 799, 120, doi: 10.1088/0004-637X/799/2/120

Benisty, M., Stolker, T., Pohl, A., et al. 2017, Astronomy and Astrophysics, 597, A42, doi: 10.1051/0004-6361/201629798

Benisty, M., Juhász, A., Facchini, S., et al. 2018, Astronomy and Astrophysics, 619, A171, doi: 10.1051/0004-6361/201833913

Bitsch, B., Crida, A., Libert, A. S., & Lega, E. 2013, Astronomy and Astrophysics, 555, A124, doi: 10.1051/0004-6361/201220310

Bitsch, B., & Kley, W. 2011, Astronomy and Astrophysics, 530, A41, doi: 10.1051/0004-6361/201016179

Casassus, S., Avenhaus, H., Pérez, S., et al. 2018, Monthly Notices of the Royal Astronomical Society, 477, 5104, doi: 10.1093/mnras/sty894

Chirikov, B. V. 1979, Physics Reports, 52, 263, doi: 10.1016/0370-1573(79)90023-1

Cincotta, P. M., Giordano, C. M., & Simó, C. 2003, Physica D Nonlinear Phenomena, 182, 151, doi: 10.1016/S0167-2789(03)00103-9

Cresswell, P., Dirksen, G., Kley, W., & Nelson, R. P. 2007, Astronomy and Astrophysics, 473, 329, doi: 10.1051/0004-6361:20077666

Debes, J. H., Poteet, C. A., Jang-Condell, H., et al. 2017, The Astrophysical Journal, 835, 205, doi: 10.3847/1538-4357/835/2/205

Deck, K. M., Holman, M. J., Agol, E., et al. 2012, Astrophysical Journal, Letters, 755, L21, doi: 10.1088/2041-8205/755/1/L21

Deck, K. M., Payne, M., & Holman, M. J. 2013, The Astrophysical Journal, 774, 129, doi: 10.1088/0004-637X/774/2/129

Dempsey, A. M., Muñoz, D., & Lithwick, Y. 2020, Astrophysical Journal, Letters, 892, L29, doi: 10.3847/2041-8213/ab800e

Dullemond, C. P., Kimmig, C. N., & Zanazzi, J. J. 2022, Monthly Notices of the Royal Astronomical Society, 511, 2925, doi: 10.1093/mnras/stab2791

Escande, D. F. 1985, Physics Reports, 121, 165, doi: 10.1016/0370-1573(85)90019-5
Escande, D. F., & Doveil, F. 1981, Physics Letters A, 83, 307, doi: 10.1016/0375-9601(81)90144-4
Facchini, S., Lodato, G., & Price, D. J. 2013, Monthly Notices of the Royal Astronomical Society, 433, 2142, doi: 10.1093/mnras/stt877
Foucart, F., & Lai, D. 2014, Monthly Notices of the Royal Astronomical Society, 445, 1731, doi: 10.1093/mnras/stu1869
Goździewski, K., Bois, E., & Maciejewski, A. J. 2002, Monthly Notices of the Royal Astronomical Society, 332, 839, doi: 10.1046/j.1365-8711.2002.05364.x
Guzzo, M. 2005, Icarus, 174, 273, doi: 10.1016/j.icarus.2004.10.015
Hadden, S. 2019, The Astronomical Journal, 158, 238, doi: 10.3847/1538-3881/ab5287
Hadden, S., & Lithwick, Y. 2018, Astronomical Journal, 156, 95, doi: 10.3847/1538-3881/aad32c
Hartmann, L., Calvet, N., Gullbring, E., & D'Alessio, P. 1998, The Astrophysical Journal, 495, 385, doi: 10.1086/305277
Hayes, W. B. 2007, Nature Physics, 3, 689, doi: 10.1038/nphys728
Henrard, J., & Lemaitre, A. 1983, Celestial Mechanics, 30, 197, doi: 10.1007/BF01234306
Holman, M. J., & Murray, N. W. 1996, Astronomical Journal, 112, 1278, doi: 10.1086/118098
Landau, L. D., & Lifshitz, E. M. 1997, Fluid Mechanics (Butterworth-Heinemann)
Larwood, J. D., Nelson, R. P., Papaloizou, J. C. B., & Terquem, C. 1996, Monthly Notices of the Royal Astronomical Society, 282, 597, doi: 10.1093/mnras/282.2.597
Laskar, J. 1996, Celestial Mechanics and Dynamical Astronomy, 64, 115, doi: 10.1007/BF00051610
Laskar, J., & Gastineau, M. 2009, Nature, 459, 817, doi: 10.1038/nature08096
Laskar, J., & Robutel, P. 1995, Celestial Mechanics and Dynamical Astronomy, 62, 193, doi: 10.1007/BF00692088
Lichtenberg, A. J., & Lieberman, M. A. 1983, Regular and stochastic motion
Lissauer, J. J., Fabrycky, D. C., Ford, E. B., et al. 2011, Nature, 470, 53, doi: 10.1038/nature09760
Lissauer, J. J., Jontof-Hutter, D., Rowe, J. F., et al. 2013, The Astrophysical Journal, 770, 131, doi: 10.1088/0004-637X/770/2/131
Lithwick, Y., & Wu, Y. 2011, The Astrophysical Journal, 739, 31, doi: 10.1088/0004-637X/739/1/31
Long, Z. C., Fernandes, R. B., Sitko, M., et al. 2017, The Astrophysical Journal, 838, 62, doi: 10.3847/1538-4357/aa64da
Lubow, S. H., & Ogilvie, G. I. 2000, The Astrophysical Journal, 538, 326, doi: 10.1086/309101
Lubow, S. H., Ogilvie, G. I., & Pringle, J. E. 2002, Monthly Notices of the Royal Astronomical Society, 337, 706, doi: 10.1046/j.1365-8711.2002.05949.x

Lynden-Bell, D., & Pringle, J. E. 1974, Monthly Notices of the Royal Astronomical Society, 168, 603, doi: 10.1093/mnras/168.3.603

Mahajan, N., & Wu, Y. 2014, The Astrophysical Journal, 795, 32, doi: 10.1088/0004-637X/795/1/32

Mardling, R. A. 2008, Resonance, Chaos and Stability: The Three-Body Problem in Astrophysics, ed. S. J. Aarseth, C. A. Tout, & R. A. Mardling, Vol. 760, 59, doi: 10.1007/978-1-4020-8431-7_3

Marino, S., Perez, S., & Casassus, S. 2015, Astrophysical Journal, Letters, 798, L44, doi: 10.1088/2041-8205/798/2/L44

Martin, R. G., Lubow, S. H., Pringle, J. E., et al. 2019, The Astrophysical Journal, 875, 5, doi: 10.3847/1538-4357/ab0bb7

Marzari, F., & Nelson, A. F. 2009, The Astrophysical Journal, 705, 1575, doi: 10.1088/0004-637X/705/2/1575

Min, M., Stolker, T., Dominik, C., & Benisty, M. 2017, Astronomy and Astrophysics, 604, L10, doi: 10.1051/0004-6361/201730949

Muñoz, D. J., Kratter, K., Springel, V., & Hernquist, L. 2014, Monthly Notices of the Royal Astronomical Society, 445, 3475, doi: 10.1093/mnras/stu1918

Muñoz, D. J., Kratter, K., Vogelsberger, M., Hernquist, L., & Springel, V. 2015, Monthly Notices of the Royal Astronomical Society, 446, 2010, doi: 10.1093/mnras/stu2220

Muñoz, D. J., & Lai, D. 2016, The Astrophysical Journal, 827, 43, doi: 10.3847/0004-637X/827/1/43

Muñoz, D. J., Springel, V., Marcus, R., Vogelsberger, M., & Hernquist, L. 2013, Monthly Notices of the Royal Astronomical Society, 428, 254, doi: 10.1093/mnras/sts015

Muro-Arena, G. A., Benisty, M., Ginski, C., et al. 2020, Astronomy and Astrophysics, 635, A121, doi: 10.1051/0004-6361/201936509

Murray, C. D., & Dermott, S. F. 1999, Solar system dynamics

Murray, N., & Holman, M. 1999, Science, 283, 1877, doi: 10.1126/science.283.5409.1877

—. 2001, Nature, 410, 773. https://arxiv.org/abs/astro-ph/0111602

Ogilvie, G. I. 1999, Monthly Notices of the Royal Astronomical Society, 304, 557, doi: 10.1046/j.1365-8711.1999.02340.x

—. 2008, Monthly Notices of the Royal Astronomical Society, 388, 1372, doi: 10.1111/j.1365-2966.2008.13484.x

Ogilvie, G. I., & Dubus, G. 2001, Monthly Notices of the Royal Astronomical Society, 320, 485, doi: 10.1046/j.1365-8711.2001.04011.x

Okazaki, A. T., Kato, S., & Fukue, J. 1987, Publications of the Astronomical Society of Japan, 39, 457

Pakmor, R., Springel, V., Bauer, A., et al. 2016, Monthly Notices of the Royal Astronomical Society, 455, 1134, doi: 10.1093/mnras/stv2380

Papaloizou, J. C. B., & Lin, D. N. C. 1995, The Astrophysical Journal, 438, 841, doi: 10.1086/175127

Papaloizou, J. C. B., & Pringle, J. E. 1983, Monthly Notices of the Royal Astronomical Society, 202, 1181, doi: 10.1093/mnras/202.4.1181

Park, R. S., Folkner, W. M., Williams, J. G., & Boggs, D. H. 2021, Astronomical Journal, 161, 105, doi: 10.3847/1538-3881/abd414

Petit, A. C., Pichierri, G., Davies, M. B., & Johansen, A. 2020, Astronomy and Astrophysics, 641, A176, doi: 10.1051/0004-6361/202038764

Pringle, J. E. 1992, Monthly Notices of the Royal Astronomical Society, 258, 811, doi: 10.1093/mnras/258.4.811

Quillen, A. C. 2011, Monthly Notices of the Royal Astronomical Society, 418, 1043, doi: 10.1111/j.1365-2966.2011.19555.x

Quillen, A. C., & French, R. S. 2014, Monthly Notices of the Royal Astronomical Society, 445, 3959, doi: 10.1093/mnras/stu2023

Rein, H., & Liu, S. F. 2012, Astronomy and Astrophysics, 537, A128, doi: 10.1051/0004-6361/201118085

Rein, H., & Tamayo, D. 2015, Monthly Notices of the Royal Astronomical Society, 452, 376, doi: 10.1093/mnras/stv1257

Serrano, M., & Español, P. 2001, Physical Review E, 64, 046115, doi: 10.1103/PhysRevE.64.046115

Shakura, N. I., & Sunyaev, R. A. 1973, Astronomy and Astrophysics, 24, 337

Shepelyansky, D. 2009, Scholarpedia, 4, 8567, doi: 10.4249/scholarpedia.8567

Shevchenko, I. I. 2007, in Near Earth Objects, our Celestial Neighbors: Opportunity and Risk, ed. G. B. Valsecchi, D. Vokrouhlický, & A. Milani, Vol. 236, 15–30, doi: 10.1017/S174392130700302X

Shevchenko, I. I. 2008, Physics Letters A, 372, 808, doi: 10.1016/j.physleta.2007.08.028

Smith, G. R., & Pereira, N. R. 1978, The Physics of Fluids, 21, 2253, doi: 10.1063/1.862163

Springel, V. 2010, Monthly Notices of the Royal Astronomical Society, 401, 791, doi: 10.1111/j.1365-2966.2009.15715.x

Springel, V., Yoshida, N., & White, S. D. M. 2001, New Astronomy, 6, 79, doi: 10.1016/S1384-1076(01)00042-2

Stolker, T., Dominik, C., Avenhaus, H., et al. 2016, Astronomy and Astrophysics, 595, A113, doi: 10.1051/0004-6361/201528039

Tamayo, D., Murray, N., Tremaine, S., & Winn, J. 2021, arXiv e-prints, arXiv:2106.14863. https://arxiv.org/abs/2106.14863

Tanaka, H., & Ward, W. R. 2004, The Astrophysical Journal, 602, 388, doi: 10.1086/380992

Toro, E. 2009, Riemann Solvers and Numerical Methods for Fluid Dynamics: A Practical Introduction (Berlin Heidelberg: Springer)

Volk, K., & Malhotra, R. 2020, Astronomical Journal, 160, 98, doi: 10.3847/1538-3881/aba0b0

Walker, G. H., & Ford, J. 1969, Phys. Rev., 188, 416, doi: 10.1103/PhysRev.188.416
Wisdom, J. 1980, Astronomical Journal, 85, 1122, doi: 10.1086/112778
Xiang-Gruess, M., & Papaloizou, J. C. B. 2013, Monthly Notices of the Royal Astronomical Society, 431, 1320, doi: 10.1093/mnras/stt254
Yee, S. W., Tamayo, D., Hadden, S., & Winn, J. N. 2021, Astronomical Journal, 162, 55, doi: 10.3847/1538-3881/ac00a9
Zanazzi, J. J., & Lai, D. 2018, Monthly Notices of the Royal Astronomical Society, 473, 603, doi: 10.1093/mnras/stx2375
Zaslavsky, G. M. 2007, Physics of chaos in Hamiltonian systems, doi: 10.1142/p507
Zhu, Z. 2019, Monthly Notices of the Royal Astronomical Society, 483, 4221, doi: 10.1093/mnras/sty3358

APPENDIX A

Reduction to Perturbed Pendulum

A.1. Circular Planets

We consider a test particle perturbed by two resonances: a j_1:$j_1 - k_1$ resonance with an inner planet (denoted with subscript 1) and a j_2:$j_2 + k_2$ resonance with an outer planet (denoted with subscript 2), where the j_i and k_i are all positive. We derive here the test particle's Hamiltonian when the two perturbing planets are on circular orbits (see Appendix A.2 for the extension to eccentric planets). The Hamiltonian (or, really, energy) is

$$H = -\underbrace{\frac{GM}{2a}}_{H_{\rm Kep}} - \frac{GM}{a}\left[\underbrace{\mu_1 C_1 e^{k_1}\cos(j_1\lambda - (j_1-k_1)\lambda_1 - k_1\varpi)}_{H_{\rm res,1}}\right. \\ \left. + \underbrace{\mu_2 C_2 e^{k_2}\cos(j_2\lambda - (j_2+k_2)\lambda_2 + k_2\varpi)}_{H_{\rm res,2}}\right] \tag{A.1}$$

where $\{a, e, \lambda, \varpi\}$, without subscripts, are the standard orbital elements for the test particle; the subscripted orbital elements are for the planets; M is the stellar mass; μ_i is the planet mass scaled to the stellar mass; and the C_i are disturbing function coefficients.[1]

[1]A more accurate model may be obtained by replacing the coefficients $C_i e^{k_i}$ in Equation (A.1), which approximate the resonance amplitudes at leading order in eccentricity, with the cosine amplitudes $S_{j_i,k_i}(\alpha, e)$ defined in Equation (23) of Hadden & Lithwick (2018), which are correct to all orders in eccentricity, then proceeding through the derivation presented here. Nonetheless, we find that the $C_i e^{k_i}$ provide sufficiently good approximations of the resonance amplitudes for all cases considered in this paper so we have chosen to work with these expressions as they are more common in the literature.

C_1 is obtained directly from Equation (6.113) of Murray & Dermott (1999), while C_2 has an additional factor of a/a_2. For $k_i \leq 4$, Murray & Dermott (1999) provide a convenient table in their Appendix B: for example, for a second order resonance with the inner planet ($k_1 = 2$), $C_1 \rightarrow f_{53}$ in their table's notation, and for a second order resonance with the outer planet ($k_2 = 2$), $C_2 \rightarrow \frac{a}{a_2} f_{45}$.

The derivation of Equation (1.1) proceeds as follows:

(1) We adopt the pendulum approximation, in which we treat all quantities in the non-Keplerian part of Equation (A.1) as constants, except for λ and λ_i. The validity of this approximation is examined in Section 1.6.2. Setting $\lambda_i = n_i t$ for the two planets, where n_i is their mean motion, we have

$$H_{\rm res,1} + H_{\rm res,2} = \epsilon_1 \cos(j_1(\lambda - n_{r,1}t)) + \epsilon_2 \cos(j_2(\lambda - n_{r,2}t)) \tag{A.2}$$

where

$$\epsilon_1 = \mu_1 |C_1| e^{k_1} \ , \quad \epsilon_2 = \mu_2 |C_2| e^{k_2} \ , \tag{A.3}$$

$$n_{r,1} = \frac{j_1 - k_1}{j_1} n_1 \ , \quad n_{r,2} = \frac{j_2 + k_2}{j_2} n_2 \ . \tag{A.4}$$

Here, $n_{r,i}$ is the mean motion when the test particle is at nominal resonance with the ith planet. We drop constant phases within the cosine arguments because they have little influence on the dynamics (although they are needed for transforming between orbital and pendulum coordinates).[2]

[2]Without neglecting phases, the argument of each cosine term is $j_i(\lambda - n_{ri}) - \xi_i$ where $\xi_1 = k_1 \varpi_1 - (j_1 - k_1)\lambda_{1,\rm initial}$ and $\xi_2 = -k_2 \varpi_2 + (j_2 + k_2)\lambda_{2,\rm initial}$. If $C_i < 0$, then $\xi_i \rightarrow \xi_i + \pi$.

(2) We turn Equation (A.1) into a proper Hamiltonian by replacing a in $H_{\rm kep}$ with $\Lambda \equiv \sqrt{GMa}$, which is the momentum conjugate to λ. We then expand Λ around its value at nominal resonance with either planet 1 or 2. Typically, one wishes to expand around whichever resonance has the larger effect. For definiteness, we choose planet 1 and comment on how things change with the other choice in Section 1.3.1. Therefore, we write

$$H_{\rm kep} = -\frac{G^2M^2}{2\Lambda^2} \approx n_{r,1}\Lambda_{r,1}\left(\frac{\Lambda-\Lambda_{r,1}}{\Lambda_{r,1}} - \frac{3}{2}\left(\frac{\Lambda-\Lambda_{r,1}}{\Lambda_{r,1}}\right)^2\right) \tag{A.5}$$

where $\Lambda_{r,1} = \sqrt{GMa_{r,1}}$ and $a_{\rm r,1} = (GM/n_{\rm r,1}^2)^{1/3}$.

(3) We make a canonical transformation to the new coordinate and momentum, $\{\phi, P\} = \{j_1(\lambda - n_{r1}t), (\Lambda - \Lambda_{r1})/j_1\}$, which produces a new Hamiltonian which differs from the original only in that the first term in brackets in Equation (A.5) disappears. Then, in order to remove a relative constant factor between $H_{\rm kep}$ and $H_{\rm res,i}$, we rescale both the new momentum and Hamiltonian by the same constant, $(-\Lambda_{r1}/\sqrt{3}j_1)$; although that rescaling is not canonical, it leaves the equations of motion unchanged. The result is

$$H(\phi, p, t) = \left(n_{r,1}j_1\sqrt{3}\right) \times \left(\frac{p^2}{2} - \epsilon_1\cos\phi - \epsilon_2\cos\left(\frac{j_2}{j_1}(\phi - (n_{r2}-n_{r1})j_1t)\right)\right) \tag{A.6}$$

where p is the rescaled momentum (given explicitly below).

(4) In order to remove the overall constant in front of Equation (A.6), we rescale time: $t_{\rm rescale} = t(n_{r,1}j_1\sqrt{3})$. We therefore have for our final Hamiltonian:

$$H(\phi, p, t_{\rm rescale}) = \frac{p^2}{2} - \epsilon_1\cos\phi - \epsilon_2\cos(r(\phi - \nu t_{\rm rescale})) \tag{A.7}$$

where

$$r = \frac{j_2}{j_1} \tag{A.8}$$

$$\nu = \frac{1}{\sqrt{3}} \frac{n_{r2} - n_{r1}}{n_{r1}} \ , \tag{A.9}$$

and ϕ and p are related to the orbital elements and (unscaled) time via

$$\phi = j_1(\lambda - n_{r1}t) \tag{A.10}$$

$$p = -\sqrt{3}\frac{\Lambda - \Lambda_{r1}}{\Lambda_{r1}} \approx -\frac{\sqrt{3}}{2}\frac{a - a_{r1}}{a_{r1}} \ . \tag{A.11}$$

A.2. Eccentric Planets

When the two planets are eccentric, each $H_{\rm res,i}$ in Equation (A.1) becomes a sum of k_i cosine terms, e.g.

$$H_{\rm res,1} = \mu_1 \left(C_{1,0} e^{k_1} \cos(\psi - k_1 \varpi) + C_{1,1} e_1 e^{k_1 - 1} \cos(\psi - \varpi_1 - (k_1 - 1)\varpi) + \cdots \right) \tag{A.12}$$

where $\psi = j_1\lambda - (j_1 - k_1)\lambda_1$. If one had to consider each of those cosine terms separately, the calculations needed for this paper would be exceedingly cumbersome. But one may avoid that with a trick (Hadden, 2019, hereafter H19). Following H19, we first write for the inner planet's resonance

$$H_{\rm res,1} = \mu_1 {\rm Real} \left\{ \left[\sum_{l=0}^{k_1} C_{1,l} \left(e_1 {\rm e}^{-i\varpi_1} \right)^l \left(e {\rm e}^{-i\varpi} \right)^{k_1 - l} \right] {\rm e}^{i\psi} \right\} \tag{A.13}$$

where the Roman e is an exponential (Euler's number). H19 showed that the square-bracketed sum in the above equation may be approximated by a single combined term.

Moreover, whereas the sum apparently depends on the complex eccentricities ($e\mathrm{e}^{-i\varpi}$) of the test particle and inner planet separately, the combined term only depends on a single combined quantity. To be explicit, H19 shows that the square-bracketed term is sufficiently well approximated by

$$[...] \approx C_1 \left(\tilde{e}_1 \mathrm{e}^{-i\widetilde{\varpi}_1}\right)^{k_1} \ , \tag{A.14}$$

where the new quantities (with tilde's) are defined via

$$\tilde{e}_1 e^{-i\widetilde{\varpi}_1} = e e^{-i\varpi} - \left(\frac{a_1}{a}\right)^{0.825} e_1 e^{-i\varpi_1} \ , \tag{A.15}$$

which is nearly the difference between the two complex eccentricities. We note parenthetically that H19 obtain the coefficient on the second term in the above expression by inserting Equation (A.15), with an undetermined coefficient, into Equation (A.14), with an undetermined amplitude[3]; then expanding into $k_1 + 1$ terms; and finally choosing the undetermined coefficients by matching term-by-term with the square-bracketed sum. Remarkably, even though there are only two fitting parameters and $k_1 + 1$ coefficients to match, the error after the fit is performed is small. Some discussion of why this fit works can be found in Section 2.4 of H19. Nonetheless, we may take advantage of this result by using for $H_{\mathrm{res},1}$ the term displayed in Equation (A.1), after simply replacing $e \to \tilde{e}_1$ and $\varpi \to \widetilde{\varpi}_1$. The resonance with the outer planet proceeds in a nearly identical way: in

[3]While H19 fits for both undetermined parameters, we have found that C_1 is a sufficiently good approximation for the amplitude and use it instead. This is true in all circumstances except when indirect terms are present. In our main example (Figure 1.1), this is only significant for the 2:1 and 1:2 resonances, so we fit two parameters in those cases.

$H_{\rm res,2}$, one makes the replacement $e \to \tilde{e}_2$ and $\varpi \to \widetilde{\varpi}_2$, where the variables with tildes are defined via $\tilde{e}_2 \mathrm{e}^{-i\widetilde{\varpi}_2} = e\mathrm{e}^{-i\varpi} - (a_2/a)^{0.825} e_2 \mathrm{e}^{-i\varpi_2}$.

The Hamiltonian with eccentric planets is therefore identical to the one with circular planets derived above (Equations (A.7)–(A.11)), except that the eccentricity that enters in ϵ_1 should be $\tilde{e}_1$ (rather than e), and the one that enters in ϵ_2 should be $\tilde{e}_2$.

APPENDIX B

The Melnikov-Arnold Integral

The MA integral is[1]

$$A_{2r}(r\nu) \equiv \lim_{s\to\infty} \int_{-s}^{s} \cos\left[r\left(\phi_{\rm sep}(t') - \nu t'\right)\right] dt' \tag{B.1}$$

where $\phi_{\rm sep}$ is the pendulum's phase on the separatrix (Chirikov, 1979). Technically, the integral does not converge in the limit of large s, but oscillates around a constant value as s increases. That constant value has the following analytic expression:

$$\left[A_{2r}(r\nu)\right]_{\rm constant} = \frac{2\pi}{\Gamma(2r)} \frac{e^{\pi r\nu/2}}{\sinh(\pi r\nu)} (2r\nu)^{2r-1} (1 + f_{2r}(r\nu)) \tag{B.2}$$

where f_{2r} is given by Equation (A.9) of Chirikov (1979); in particular, $f_{2r} = 0$ when $0 \leq r \leq 1$, and f_{2r} is typically order unity for $1 < r \lesssim 2$. The dependence of A_{2r} on s (before the s limit is taken) is illustrated by the orange dotted curve in Figure B.1. At large s, it oscillates around Equation (B.2) (the horizontal line). Even though Equation (B.1) is not strictly identical to Equation (B.2), we follow Chirikov (1979), and drop the "constant" label from Equation (B.2) throughout the body of the paper.

[1]We set $\epsilon_1 = 1$ throughout this appendix.

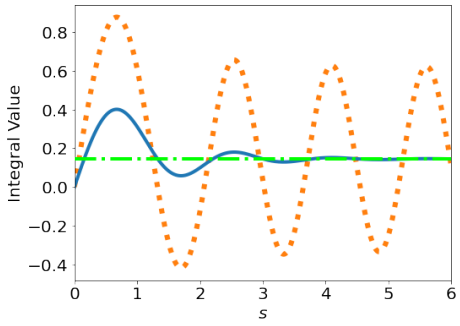

Figure B.1. An illustration of the proper integral versions of $A_{2r}(r\nu)$ (the orange dotted line) and $\tilde{A}_{2r}(r\nu)$ (the blue solid line) as functions of the integration bound, as well as the analytic expression given in Equation (B.2) (the horizontal green line), with $r = 1$ and $\nu = 4.2$. This figure is based on Figure 3.22 in Lichtenberg & Lieberman (1983).

The integral that appears in the classical kick criterion (Section 1.4.2.1) is not Equation (B.1), but

$$\tilde{A}_{2r}(r\nu) \equiv \frac{1}{\nu} \lim_{s\to\infty} \int_{-s}^{s} \dot{\phi}_{\text{sep}}(t') \cos\left[r\left(\phi_{\text{sep}}(t') - \nu t'\right)\right] \, \mathrm{d}t' \ , \tag{B.3}$$

which has an extra factor of $\dot{\phi}_{\text{sep}}/\nu$. Unlike Equation (B.1), this integral does converge to Equation (B.2). The blue curve in Figure B.1 shows this integral and its convergence at large s. We note that in the context of the classical kick criterion, the issue of integral non-convergence is merely an artifact of the standard definition of the MA integral (Equation B.1); i.e., had one chosen to adopt Equation (B.3) as the definition, no such issue would arise. We have belabored the non-convergence because it plays an important role in the improved kick criterion (Appendix C).

APPENDIX C

Improved Kick Criterion

For the kick criterion, one must evaluate $\mathcal{K}$ in Equation (1.5), which we restate here for convenience as

$$\mathcal{K}(E, r, \nu; s) = \int_{-s}^{s} \dot{\phi}_{\rm unp}(t') \cos\left[r(\phi_{\rm unp}(t') - \nu t')\right] \mathrm{d}t' \tag{C.1}$$

where $s = T/2$ and $T = T(E)$ is the unperturbed period. Note that we now allow $\mathcal{K}$ to depend explicitly on the integral limit s, for reasons that will be apparent; we set $\epsilon_1 = 1$ for this appendix; and we explicitly display the dependence of $\mathcal{K}$ on r and ν, unlike in the body of the paper. For the classical criterion, one sets $\phi_{\rm unp}$ in this expression to be on the separatrix and $T = \infty$. But for the improved criterion, we allow $\phi_{\rm unp}$ to follow a trajectory slightly displaced from the separatrix by approximating

$$\phi_{\rm unp}(t) \approx \phi_{\rm sep}(t) + (\Delta p)t \tag{C.2}$$

where Δp is a constant that we take to be the relative drift rate at $t = 0$:

$$\Delta p = \dot{\phi}_{\rm unp}(0) - \dot{\phi}_{\rm sep}(0) \tag{C.3}$$

$$= \sqrt{2(E+1)} - 2 \ . \tag{C.4}$$

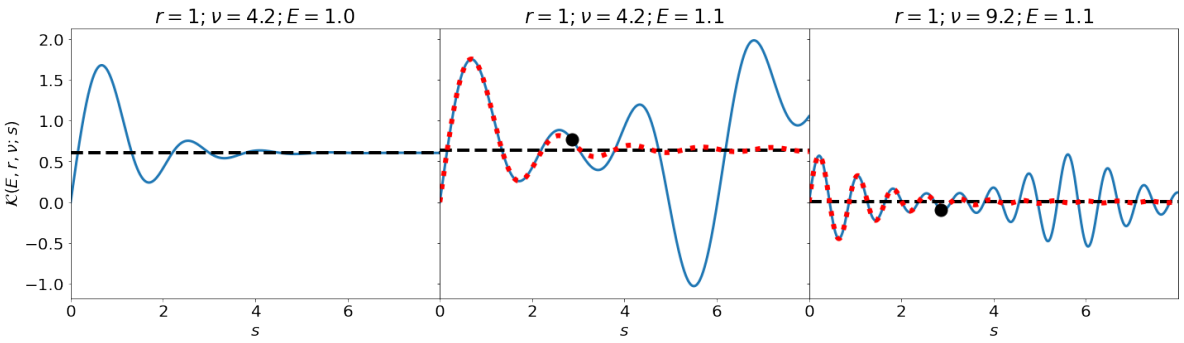

Figure C.1. In each panel, we show the original definition of $\mathcal{K}$ as a function of s (Equation C.1) as a blue solid line. We show our approximation to $\mathcal{K}$ (Equation C.5) as a red dotted line. The approximation is absent from the left panel because it is identical to Equation (C.1) when $E = 1$. The horizontal dashed lines are given by Equation (C.7). The black points indicate the value of Equation (C.1) at $s = T/2$. It is absent in the left panel because $T = \infty$ there.

Inserting this $\phi_{\rm unp}$ into Equation (C.1) leads to

$$\mathcal{K}(E, r, \nu; s) \approx \int_{-s}^{s} \Big(\dot{\phi}_{\rm sep}(t') + \Delta p\Big) \cos(r(\phi_{\rm sep}(t') - (\nu - \Delta p)t'))\mathrm{d}t' \ . \tag{C.5}$$

Figure C.1 shows $\mathcal{K}$ versus s for three sets of parameters. The left panel has $E = 1$ (and hence $\Delta p = 0$) and is the same as the blue curve in Figure B.1. In the middle panel, the trajectory is displaced from the separatrix ($E = 1.1$). The solid blue curve shows the exact integral (Equation C.1); the red dotted curve shows the approximation (Equation C.5); and the black dot indicates where $s = T/2$. We see that the approximation agrees well for this value of E at the time of interest. The right panel shows another comparison at higher ν.

Figure C.1 also illustrates an important, yet subtle, complication: the value of Equation (C.1) (i.e., the height of the black dot at time $T/2$) is subject to fast oscillations, and it depends on the precise phase of the fast oscillation at that time. Yet in truth,

one wishes to average out the fast oscillations. That is because each successive kick is subject to similar fast oscillations, and so they average out after many kicks. As a result, the value of Equation (C.1) at time $T/2$ is not what should enter the kick criterion. One requires the height of the horizontal lines in the figure, rather than those of the black dots.

To calculate the horizontal lines, we start from Equation (C.5), and focus first on the $\dot{\phi}_{\rm sep}$ term within the brackets. At large $|t|$, $\dot{\phi}_{\rm sep}$ decays smoothly to zero ($\dot{\phi}_{\rm sep} \approx 4e^{-|t|}$). Therefore, extending the integration limits to $s = \infty$ will remove oscillations on a timescale much faster that T. The second bracketed term (Δp) is subdominant to the first for $|t'| < T/2$ and is oscillatory as $s \to \infty$. Therefore, we neglect it. The net result is that Equation (C.1) should be replaced with

$$\mathcal{K}(E, r, \nu) \approx \int_{-\infty}^{\infty} \dot{\phi}_{\rm sep}(t') \cos(r(\phi_{\rm sep}(t') - (\nu - \Delta p)t'))\mathrm{d}t' \tag{C.6}$$

$$= (\nu - \Delta p) A_{2r}\left[r(\nu - \Delta p)\right] \tag{C.7}$$

where the latter equality follows from Appendix B, and A_{2r} is given by Equation (B.2). Equation (C.7) is the main result of this appendix; the horizontal lines in Figure C.1 are at the values prediction by this equation. In Section 1.4.2.2, we use Equation (C.7) to produce the improved kick criterion.

The "improved" expression for $\mathcal{K}$ differs from the classical one (Equation 1.9) by the replacement $\nu \to \nu - \Delta p$. One may understand why $\nu - \Delta p$ is the relevant frequency by referring to a surface of section, such as Figure 1.3. The perturbing resonance is at height $p = \nu$, and our trajectory of interest is at height $p = 2 + \Delta p$ at the critical moment when

it receives its kick (i.e., when $\phi_{\rm unp} \approx 0$). The difference between those two heights is equal to the difference in frequencies, which sets the strength of the kick. Therefore the kick strength on our trajectory of interest is almost equivalent to the kick on a trajectory *on* the separatrix, provided the height of the perturbing resonance is lowered from $\nu \to \nu - \Delta p$.

Figure (C.2) (left panel) compares the various expressions for $\mathcal{K}$ as a function of E, for $r = 1$ and $\nu = 4.2$. The horizontal dot-dashed line is the classical $\mathcal{K}$ (Equation 1.9), which is independent of E. The blue solid curve is the exact expression before the removal of fast oscillations (i.e., Equation C.1 at $s = T/2$). One sees that very close to the separatrix ($E - 1 \lesssim 1$), the exact expression oscillates around the classical one. The oscillations are caused by the aforementioned fast oscillations, and do not contribute to chaos. In fact, the classical expression is more accurate than the exact one at such close distances to the separatrix. But the peak in the blue curve at $E - 1 \sim 10$ is not due to fast oscillations, and the classical expression is inadequate there. The black dashed curve is the improved expression (Equation C.7). It both captures the true behavior close to the separatrix, and does an adequate job at capturing the peak—considerably better than the classical criterion. The right panel of Figure C.2 is similar, but for $r = 4$ and $\nu = 2.5$, and likewise shows how Equation (C.7) captures the broad peak while removing the fast oscillations. We note that a truer measure for how well Equation (C.7) performs can be ascertained by comparing its prediction for the transition to chaos with numerical integrations, as is done in Figure 1.6 (a) and (b) for the case $r = 1$ and $\epsilon_2/\epsilon_1 = 0.8$. We have done so for many additional cases, and find that Equation (C.7) invariably produces the best match with simulations.

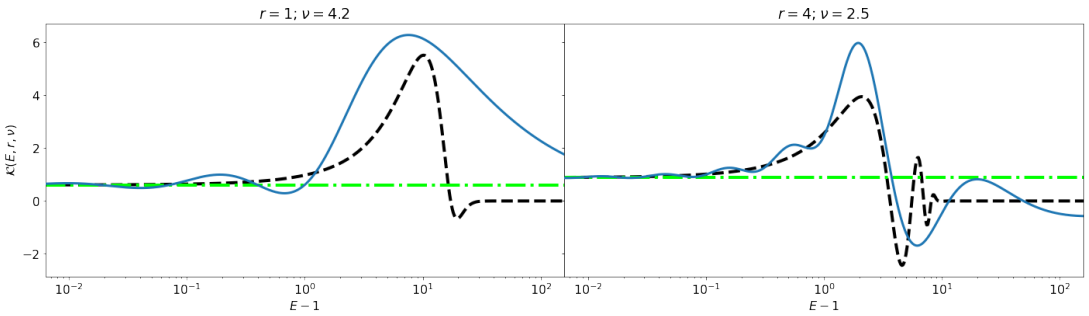

Figure C.2. A comparison of different expressions for $\mathcal{K}$ as a function of E: Solid blue lines depict the original definition (Equation C.1), green dot-dashed lines depict Chirikov's approximation (Equation 1.9), and black dashed lines depict our approximation (Equation C.7). The left panel has the same parameters as the two left panels of Figure C.1.

We conclude this Appendix with a second, more formal, derivation of Equation (C.7), based on the action-angle formalism derived in Appendix D. The rate of change of the unperturbed energy is

$$\frac{dE}{dt} = \frac{\partial E}{\partial J}\frac{dJ}{dt} = -\omega\frac{\partial H}{\partial \theta} = \epsilon\omega \sum_{M=-\infty}^{\infty} c_M(M+lr)\sin\left[M\theta + r(l\theta - \nu t) + \psi^{(1)}\right] \tag{C.8}$$

where $\omega = 2\pi/T$; the final expression follows from the Fourier expansion of the perturbation in the angle variable (Equation D.5); and $\psi^{(1)}$ is the forcing phase at the time of the first kick (Section 1.4.1). Integrating over an (unperturbed) orbit yields a change in energy with the form of Equation (1.4) where

$$\mathcal{K}(E, r, \nu) = \sum_{M=-\infty}^{\infty} \omega c_M\left(\frac{M+lr}{r}\right)\int_{-\frac{\pi}{\omega}}^{\frac{\pi}{\omega}} \cos\left[M\theta + r(l\theta - \nu t)\right] \mathrm{d}t \tag{C.9}$$

We keep in this sum over M only the dominating term (i.e., the one that is near-resonant) satisfying $(lr + M)\omega - r\nu \sim 0$. This effectively removes the fast oscillations. Next, we set

$\theta = \omega t$ and evaluate the integral to yield

$$\mathcal{K}(E, r, \nu) \approx 2\omega c_M \left(\frac{M + lr}{r}\right) \frac{\sin\left[\frac{\pi}{\omega}(M\omega + r(l\omega - \nu))\right]}{(M + lr)\omega - r\nu} \ . \tag{C.10}$$

Using the approximation that $(lr + M)\omega - r\nu \sim 0$ and inserting Equation (D.9) for c_M, we get

$$\mathcal{K}(E, r, \nu) \approx (\nu - \Delta p) A_{2r} \left[r(\nu - \Delta p)\right] \tag{C.11}$$

which is identical to Equation (C.7).

APPENDIX D

Perturbed Pendulum Expansion in Action-Angle Variables

For Section 1.5, we require the expansion of the perturbed piece of the Hamiltonian, H', in terms of the action-angle variables of the unperturbed pendulum. Before expanding $H' \equiv \epsilon_2 \cos[r(\phi - \nu t)]$, we first expand $e^{ir\phi}$. In the libration zone of H_{pend}, ϕ is a periodic function of θ (i.e. $\phi(\theta) = \phi(\theta + 2\pi n)$ where $n \in \mathbb{Z}$). Hence we may expand

$$e^{ir\phi} = \sum_M c_M e^{iM\theta} \text{ , where } c_M \equiv \frac{1}{2\pi} \int_{-\pi}^{\pi} e^{i(r\phi - M\theta)} \mathrm{d}\theta \text{ (in libration zone)} \tag{D.1}$$

But in the circulation zone, ϕ changes by 2π when θ does; i.e., it is the difference $(\phi - \theta)$ which is a periodic function of θ. In that case, one should replace $\phi \to \phi - \theta$ throughout Equation (D.1). Both zones may be combined by introducing

$$l = \begin{cases} 0 \text{ in libration zone} \\ 1 \text{ in circulation zones} \end{cases} \tag{D.2}$$

in which case

$$e^{ir\phi} = \sum_M c_M e^{i(M+lr)\theta} \text{ , where } c_M \equiv \frac{1}{2\pi} \int_{-\pi}^{\pi} e^{i[r\phi - (M+lr)\theta]} \mathrm{d}\theta. \tag{D.3}$$

Note that c_M is real, which follows from the fact that H_{pend} is unchanged when $\phi \to -\phi$. Using Equation (D.3), we write

$$H' = \epsilon_2 \cos\left[r\left(\phi - \nu t\right)\right] \tag{D.4}$$

$$= \epsilon_2 \sum_{M=-\infty}^{\infty} c_M \cos\left[M\theta + r\left(l\theta - \nu t\right)\right] \tag{D.5}$$

where

$$c_M = \frac{1}{2\pi} \int_{-\pi}^{\pi} \cos\left[r\phi - \left(M + lr\right)\theta\right] \mathrm{d}\theta \ . \tag{D.6}$$

This expression was derived for the libration zone by Smith & Pereira (1978) and for the circulation zone by Escande & Doveil (1981). The above expressions for H' and c_M are exact, and are the main result of this appendix. There are several approaches to approximate/compute the integral in c_M: Smith & Pereira (1978) give analytic expressions for $r = \frac{1}{2}$ and $r = 1$, and show analytic solutions exist for all $2r \in \mathbb{Z}$. Escande (1985) gives approximate expressions far from the separatrix for both inside and outside of resonance, which we use for the sake of computation time to create Figures 1.12, and 1.13.

We conclude this appendix with an approximate expression for c_M, which is needed for deriving the improved kick criterion with the action-angle method (Appendix C) and for quantifying secondary resonance overlap (Section 1.5.2). As was done to evaluate Equation (C.1), we set $\phi(t) \approx \phi_s(t) + (\Delta p)t$ and take the integration bounds to infinity

to get

$$c_M \approx \frac{\omega}{2\pi} \int_{-\infty}^{\infty} \cos\left[r\phi_{\text{sep}} - (M + lr)\,\omega t + r\Delta p\ t\right] \mathrm{d}t \tag{D.7}$$

$$= \frac{\omega}{2\pi} A_{2r}\left[(M + lr)\,\omega - r\Delta p\right] \tag{D.8}$$

where $A_m(\lambda)$ is the MA-integral given in Equation (B.2). Although the above approximation is generally a good one, it fails at $M = 0$. In that case, as $E \to \infty$ the argument of the A_{2r} approaches a constant (because $\omega \to \Delta p + 2$) and the prefactor (ω) increases without bound. However, in truth $\lim_{E\to\infty} c_0 = 1$. To correct for that, we change the prefactor by a quantity that is small whenever $M \neq 0$, yet yields the correct limiting behavior of c_0, by setting

$$c_M \approx \frac{1}{2\pi}\left[\omega - \frac{r\Delta p}{M + lr}\right] A_{2r}\left[(M + lr)\,\omega - r\Delta p\right] \ . \tag{D.9}$$

APPENDIX E

The Warp Equations

We derive the governing equations for the steady-state warp of a disk caused by a planet. Our results are similar to those found in Papaloizou & Lin (1995) and Lubow & Ogilvie (2000), but with some differences to be described in Section 2.2.3. We model the disk perturbatively. The background state consists of disk and planet both having zero inclination, while the perturbation is the an $m = 1$ mode corresponding to the disk's inclination. We use cylindrical coordinates (R, ϕ, z) aligned with the planet's orbit. We assume the disk mass is sufficiently low that the gravitational force it exerts is negligible. We also assume that the equation of state is locally isothermal, with pressure = density $\times$ $c(r)^2$, where $c(r)$ is the prespecified sound speed (Equation 2.1), and $r = \sqrt{R^2 + z^2}$.

The disk's equations are

$$0 = \frac{\partial \boldsymbol{v_T}}{\partial t} + (\boldsymbol{v_T} \cdot \boldsymbol{\nabla})\boldsymbol{v_T} + c^2 \boldsymbol{\nabla} \lambda_T + \boldsymbol{\nabla}(\Phi + c^2) - \boldsymbol{f_T} \tag{E.1}$$

$$0 = \frac{\partial \lambda_T}{\partial t} + \boldsymbol{\nabla} \cdot \boldsymbol{v_T} + (\boldsymbol{v_T} \cdot \boldsymbol{\nabla})\lambda_T \tag{E.2}$$

where the T subscript denotes total value (i.e., background plus perturbed), $\boldsymbol{v_T}$ is the velocity, $\lambda_T = \ln \rho_T$ is the logarithm of the density, $\boldsymbol{f}_T$ is the viscous force, and Φ is the sum of star and planet potentials. We first solve the time-independent case by expanding the perturbation in Hermite polynomials, following Okazaki et al. (1987); Ogilvie (2008). Then, we include time dependence in Appendix E.3.

E.1. Background

We assume the background is axisymmetric, and neglect viscosity. The velocity is

$$\boldsymbol{v} = R\Omega\hat{\boldsymbol{\phi}} \ , \tag{E.3}$$

with $\Omega(R, z)$ to be determined. We denote background quantities by dropping the T subscript. The profiles of Ω and λ are determined by the radial and vertical components of Equation (E.1):

$$R\Omega^2 = c^2\frac{\partial\lambda}{\partial R} + \frac{\partial}{\partial R}\left(\Phi + c^2\right) \tag{E.4}$$

$$0 = c^2\frac{\partial\lambda}{\partial z} + \frac{\partial}{\partial z}\left(\Phi + c^2\right) \ . \tag{E.5}$$

The vertical equation (Equation E.5) to leading order gives

$$\lambda \approx \ln\left[\frac{\Sigma(R)\psi(\zeta)}{H}\right] \tag{E.6}$$

where $\zeta = z/H$, $\Sigma(R)$ is the surface density profile,

$$\psi(\zeta) = \frac{1}{\sqrt{2\pi}}e^{-\zeta^2/2} \ , \tag{E.7}$$

$H \approx c_0/\Omega_K \approx c_0/\Omega_0$ is the scale height where Ω_K is the Keplerian frequency, and Ω_0 and c_0 are their respective values at $z = 0$.

E.2. Steady-State Equations

We set $\lambda_T = \lambda + \lambda'$, with $\lambda' =$ (function of R) $\times e^{i\phi}$, and similarly for $\boldsymbol{v}_T$. Perturbing Equations (E.1) and (E.2) in steady-state produces

$$0 = i\Omega v'_R - 2\Omega v'_\phi + c^2 \frac{\partial \lambda'}{\partial R} - f'_R \tag{E.8}$$

$$0 = i\Omega v'_\phi + \left(2\Omega + R\frac{\partial \Omega}{\partial R}\right) v'_R + R\frac{\partial \Omega}{\partial z} v'_z + \frac{ic^2\lambda'}{R} - f'_\phi \tag{E.9}$$

$$0 = i\Omega v'_z + c^2 \frac{\partial \lambda'}{\partial z} \tag{E.10}$$

$$0 = i\Omega \lambda' + \frac{\partial \lambda}{\partial z} v'_z + \frac{\partial v'_z}{\partial z} + \frac{1}{R}\frac{\partial}{\partial R}\left(R v'_R\right) + \frac{\partial \lambda}{\partial R} v'_R + \frac{i v'_\phi}{R} \ . \tag{E.11}$$

We solve these equations by expanding the perturbed quantities in Hermite polynomials, e.g.,

$$X' = X'_0 \mathcal{H}_0(\zeta) + X'_1 \mathcal{H}_2(\zeta) + X'_2 \mathcal{H}_2(\zeta) + ... \tag{E.12}$$

where $\mathcal{H}_n$ is the nth Hermite polynomial and X'_n is given by

$$X'_n = \frac{1}{n!} \langle \mathcal{H}_n(\zeta) X' \rangle \tag{E.13}$$

where, as shorthand, we denote

$$\langle (\cdot) \rangle \equiv \int_{-\infty}^{\infty} (\cdot) \psi(\zeta) \mathrm{d}\zeta \ . \tag{E.14}$$

The Hermite polynomials have the property that $\langle \mathcal{H}_n \mathcal{H}_m \rangle = n! \delta_{nm}$, where δ_{nm} is the Kronecker delta function. We adopt the ansatz that the solution does not differ too

significantly from the rigid tilt solution, i.e., λ', v'_R, and v'_ϕ are odd functions while v'_z is even,[1] and that the nth term has magnitude $O(H/R)^n$.[2]

Multiplying Equations (E.8) and (E.9) by $\mathcal{H}_1(\zeta)\psi(\zeta)$ and Equation (E.10) by $\psi(\zeta)$, vertically integrating in ζ, and neglecting terms $O(H^2/R^2)$ and smaller yields:

(E.15)
$$0 = i\Omega_0 v'_{R,1} - 2\Omega_0 v'_{\phi,1} + Hc_0^2 \frac{\mathrm{d}}{\mathrm{d}R}\left(\frac{\lambda'_1}{H}\right) - f'_{R,1}$$

(E.16)
$$0 = i\Omega_0 v'_{\phi,1} + \left(2\Omega_0 + R\frac{\mathrm{d}\Omega_0}{\mathrm{d}R}\right) v_{R,1} + \frac{ic_0^2\lambda_1}{R} + \frac{\Omega_0}{2}\frac{\mathrm{d}\ln c_0^2}{\mathrm{d}\ln R}\left[1 + \frac{\langle\zeta\delta\Phi\rangle}{R^2\Omega_0^2}\right]\frac{H}{R}v'_{z,0} - f'_{\phi,1}$$

(E.17)
$$0 = i\Omega_0 v'_{z,0} + \frac{c_0^2\lambda'_1}{H} \ ,$$

where $\frac{\partial\Omega}{\partial z}$ is determined from $\frac{\partial}{\partial z}\times$ (Equation E.4) $-\frac{\partial}{\partial R}\times$ (Equation E.5):

(E.18)
$$2R\Omega\frac{\partial\Omega}{\partial z} = \frac{\mathrm{d}\ln c_0^2}{\mathrm{d}\ln R}\left[\Omega^2\zeta + \frac{\delta\Phi}{R^2}\right]\frac{H}{R}$$

and we define

(E.19)
$$\Omega_0^2 \equiv \left.\frac{1}{R}\frac{\partial\Phi}{\partial R}\right|_{z=0}$$

---

[1]This can also be argued by symmetry: λ', e.g., must be positive for the entirety of the midplane of a warped disk. As $e^{i\phi}$ becomes negative for half the orbit, the sign must be counter-acted by the fact that λ' is odd in z.

[2]As an example, the rigid tilt solution for the radial velocity is $v'_R = \sin(I)\Omega z$ (Papaloizou & Lin, 1995). Ω is an even function in z, whose expansion in z/R has $O(1)$ coefficients. Therefore, the expansion in Hermite polynomials has only odd terms with ordering is $O(H^n/R^n)$.

and

$$\delta\Phi \equiv R\left[\frac{R}{H^2}\frac{\partial}{\partial\zeta} - \zeta\frac{\partial}{\partial R}\right]\Phi \ . \tag{E.20}$$

Solving for λ_1' in Equation (E.17), inserting it into Equations (E.15) and (E.16), and rescaling gives

$$0 = v_{R,1}' + 2iv_{\phi,1}' + \frac{H}{R}\frac{\mathrm{d}\ln c_0^2}{\mathrm{d}\ln R}v_{z,0}' - \frac{H}{R}\left[\frac{\mathrm{d}\ln\Omega_0}{\mathrm{d}\ln R} + \frac{\mathrm{d}}{\mathrm{d}\ln R}\right]v_{z,0}' + \frac{if_{R,1}'}{\Omega_0} \tag{E.21}$$

$$0 = \left(2 + \frac{\mathrm{d}\ln\Omega_0}{\mathrm{d}\ln R}\right)v_{R,1} + iv_{\phi,1}' + \frac{H}{R}\left[1 + \frac{1}{2}\frac{\mathrm{d}\ln c_0^2}{\mathrm{d}\ln R}\left(1 + \frac{\langle\zeta\delta\Phi\rangle}{R^2\Omega_0^2}\right)\right]v_{z,0}' - \frac{f_{\phi,1}'}{\Omega_0} \ . \tag{E.22}$$

Turning now to the continuity equation (Equation E.11), there is a subtlety with the ordering of the terms. The first three terms all require going to higher order because λ' and $\frac{\partial\lambda}{\partial z}$ are both R^2/H^2 larger than the other terms, and the derivative of v_z' brings $v_{z,2}'$ down to the order of the rest of the terms. λ_1' at higher order is given by Equation (E.10) to $O(H^4/R^4)$:

$$\left[1 + \frac{(c^2)_2}{c_0}\left(\frac{H}{R}\right)^2\right]\frac{iH\lambda_1'}{c_0^2} = \Omega_0\left[1 + \frac{\Omega_2}{\Omega_0}\left(\frac{H}{R}\right)^2\right]v_{z,0}' \tag{E.23}$$

where $\Omega = \Omega_0 + \Omega_2 z^2/R^2 + ...$ and likewise for c^2. Therefore, after multiply by $\mathcal{H}_1(\zeta)$ and integrating, the first three terms of the continuity equation become

$$\langle\mathcal{H}_1(\zeta)\left[i\Omega\lambda' + \frac{\partial\lambda}{\partial z}v_z' + \frac{\partial v_z'}{\partial z}\right]\rangle = \frac{\Omega_0^2 H}{c_0^2}\left(4\frac{\Omega_2}{\Omega_0} - \frac{(c^2)_2}{c_0^2}\right)\left(\frac{H}{R}\right)^2 v_{z,0}' + \frac{H}{R}\frac{\mathrm{d}\ln(\Sigma H^2)}{\mathrm{d}\ln R}\frac{v_{z,0}'}{R} - \frac{\langle\zeta\delta\Phi\rangle}{Rc_0^2}v_{z,0}' \tag{E.24}$$

where $v'_{z,2}$ canceled completely,Equation (E.18) gives $\Omega_2 \approx \frac{\Omega_0}{4}\frac{\mathrm{d}\ln c_0^2}{\mathrm{d}\ln R}$, $(c^2)_2 \approx \frac{c_0^2}{2}\frac{\mathrm{d}\ln c_0^2}{\mathrm{d}\ln R}$, and $\frac{\partial\lambda}{\partial z}$ is given by $z \times$ (Equation E.4) $- R \times$ (Equation E.5):

$$\frac{\partial\lambda}{\partial z} = -\frac{\Omega^2 z}{c^2} + \frac{z}{R}\frac{\partial\lambda}{\partial R} - \frac{\delta\Phi}{Rc^2} \ . \tag{E.25}$$

Including the remaining terms and multiplying by R yields

$$0 = \frac{1}{\Sigma H}\frac{\partial}{\partial R}(R\Sigma H v'_{R,1}) + i v'_{\phi,1} - \frac{\langle\zeta\delta\Phi\rangle}{c_0^2} v'_{z,0} + \frac{H}{R}\left[\frac{1}{2}\frac{\mathrm{d}\ln c_0^2}{\mathrm{d}\ln R} + \frac{\mathrm{d}\ln(\Sigma H^2)}{\mathrm{d}\ln R}\right] v'_{z,0} \ . \tag{E.26}$$

Our set of three equations, Equations (E.21), (E.22), and (E.26), can be further reduced by eliminating $v'_{\phi,1}$ via (Equation E.21)$-2\times$(Equation E.22) and (Equation E.21)$-$(Equation E.22) $-$ (Equation E.26):

(E.27)
$$0 = -\left(3 + 2\frac{\mathrm{d}\ln\Omega_0}{\mathrm{d}\ln R}\right) v'_{R,1} + \frac{i}{\Omega_0}\left(f'_{R,1} - 2i f'_{\phi,1}\right) - \frac{H}{R^2\Omega_0}\frac{\mathrm{d}}{\mathrm{d}R}\left(R^2\Omega_0 v'_{z,0}\right) - \frac{H}{R}\frac{\mathrm{d}\ln c_0^2}{\mathrm{d}\ln R}\frac{\langle\zeta\delta\Phi\rangle}{R^2\Omega_0^2} v'_{z,0}$$

and

$$0 = -\frac{1}{\Sigma H R\Omega_0}\frac{\mathrm{d}}{\mathrm{d}R}\left[\Sigma H R\Omega_0\left(R v'_{R,1} + H v'_{z,0}\right)\right] + \frac{\langle\zeta\delta\Phi\rangle}{c_0^2} v'_{z,0} + \frac{i}{\Omega_0}\left(f'_{R,1} - i f'_{\phi,1}\right) \ , \tag{E.28}$$

where we dropped the subdominate $\langle\zeta\delta\Phi\rangle$ term. Taking advantage of the combination in the derivative in Equation (E.28), we swap variables to u_r[3] and u_z defined as

$$u_r \equiv \frac{1}{\Omega_0}\left[\frac{v'_{R,1}}{H} + \frac{v'_{z,0}}{R}\right] \tag{E.29}$$

$$u_z \equiv \frac{v'_{z,0}}{R\Omega_0} \tag{E.30}$$

and simplify the expression by using the dimensionless square of the epicyclic frequency:

$$\hat{\kappa}_0^2 = 4 + 2\frac{\mathrm{d}\ln\Omega_0}{\mathrm{d}\ln R}\ . \tag{E.31}$$

Making these substitutions and dividing the equations by $H\Omega_0$ simplifies Equations (E.27) and (E.28) to

$$R\frac{\mathrm{d}u_z}{\mathrm{d}R} = \left(1-\hat{\kappa}_0^2\right)u_r - \frac{\mathrm{d}\ln c_0^2}{\mathrm{d}\ln R}\frac{\langle\zeta\delta\Phi\rangle}{R^2\Omega_0^2}u_z + \frac{i(f'_{R,1} - 2if'_{\phi,1})}{H\Omega_0^2} \tag{E.32}$$

and

$$\frac{1}{\Sigma H^2R^2\Omega_0^2}\frac{\mathrm{d}}{\mathrm{d}R}\left(\Sigma H^2R\Omega_0^2u_r\right) = \frac{\langle\zeta\delta\Phi\rangle}{c_0^2}u_z + \frac{i(f'_{R,1} - if'_{\phi,1})}{H\Omega_0^2}\ . \tag{E.33}$$

As a pair, they describe the warp in steady-state in terms of u_r and u_z.

E.3. Time-Dependent Equations

We now include time dependence in Equations (E.8)-(E.11) and follow the same procedure as in Appendix E.2 to derive the final form. Following Lubow & Ogilvie (2000), we assume that the time variances are slow, and therefore $\partial^2/\partial t^2$ terms can be neglected.

[3]The name, u_r, is chosen as the definition corresponds to a rescaling of $v'_{r,1}$. This can be seen by: $\langle v'_r\zeta\rangle = v'_{R,1} + \frac{H}{R}v'_{z,0} + O(H^3/R^3)$.

The z-part of the momentum equation (Equation E.17) becomes:

$$0 = \frac{\partial v'_{z,0}}{\partial t} + i\Omega_0 v'_{z,0} + \frac{c_0^2 \lambda'_1}{H} \ . \tag{E.34}$$

The remaining equations then become

$$\frac{i}{\Omega_0}\frac{\partial v'_{R,1}}{\partial t} - iH\frac{c_0^2}{\Omega_0}\frac{\partial}{\partial R}\left(\frac{1}{c_0^2}\frac{\partial v_{z,0}}{\partial t}\right) = [\text{RHS of Eq. (E.21)}] \tag{E.35}$$

$$-\frac{1}{\Omega_0}\frac{\partial v'_{\phi,1}}{\partial t} - \frac{iH}{R\Omega_0}\frac{\partial v'_{z,0}}{\partial t} = [\text{RHS of Eq. (E.22)}] \tag{E.36}$$

$$\frac{iRH\Omega_0}{c_0^2}\frac{\partial v'_{z,0}}{\partial t} = [\text{RHS of Eq. (E.26)}] \tag{E.37}$$

where the right hand side (RHS) of the equations are unchanged. As before, we compute (Equation E.35) $-$ 2 $\times$ (Equation E.36) and (Equation E.35) $-$ (Equation E.36) $-$ (Equation E.37), which give

$$\frac{i}{\Omega_0}\frac{\partial v'_{R,1}}{\partial t} - iH\frac{c_0^2}{\Omega_0}\frac{\partial}{\partial R}\left(\frac{1}{H}\frac{\partial \lambda'_1}{\partial t}\right) + \frac{2}{\Omega_0}\frac{\partial v'_{\phi,1}}{\partial t} + \frac{2iH}{R\Omega_0}\frac{\partial v'_{z,0}}{\partial t} = [\text{RHS of Eq. (E.27)}] \tag{E.38}$$

and

$$-\frac{2iRH\Omega_0}{c_0^2}\frac{\partial v'_{z,0}}{\partial t} = [\text{RHS of Eq. (E.28)}] \ , \tag{E.39}$$

where, for the latter equation, we only keep the one time derivative as it is $O(c_0^{-2})$ larger than the rest. The factor of 2 arises because $\frac{\partial \lambda'_1}{\partial t}$ contributes one and $i\Omega_0\lambda'_1$ contributes another.

We eliminate $v'_{\phi,1}$ in Equation (E.38) by taking the time derivative of Equation (E.16) and dropping higher order terms, giving:

$$\frac{\partial v'_{\phi,1}}{\partial t} = \frac{i}{2}\frac{\partial v'_{R,1}}{\partial t} + \frac{iHc_0^2}{2}\frac{\partial}{\partial R}\left(\frac{1}{H}\frac{\partial \lambda_1}{\partial t}\right) \tag{E.40}$$

which reduces Equation (E.38) to

$$\frac{2i}{\Omega_0}\frac{\partial v'_{R,1}}{\partial t} + \frac{2iH}{R\Omega_0}\frac{\partial v'_{z,0}}{\partial t} = [\text{RHS of Eq. (E.27)}] \ . \tag{E.41}$$

Finally, converting to u_r and u_z and matching the previous scaling, yields

$$\frac{2i}{\Omega_0}\frac{\partial u_r}{\partial t} + \left(\hat{\kappa}_0^2 - 1\right) u_r - \frac{i(f'_{R,1} - 2if'_{\phi,1})}{H\Omega_0^2} = -R\frac{\partial u_z}{\partial R} - \frac{\mathrm{d}\ln c_0^2}{\mathrm{d}\ln R}\frac{\langle\zeta\delta\Phi\rangle}{R^2\Omega_0^2}u_z \ . \tag{E.42}$$

The other time-dependent warp equation is attained by is attained by dividing Equation (E.39) by $H\Omega_0$ and converting to u_r and u_z:

$$\frac{2iR^2\Omega_0}{c_0^2}\frac{\partial u_z}{\partial t} + \frac{\langle\zeta\delta\Phi\rangle}{c_0^2}u_z + \frac{i(f'_{R,1} - if'_{\phi,1})}{H\Omega_0^2} = \frac{1}{\Sigma H^2 R\Omega_0^2}\frac{\mathrm{d}}{\mathrm{d}R}\left(\Sigma H^2 R^2\Omega_0^2 u_r\right) \ . \tag{E.43}$$

E.4. The Viscous Force

We now derive the perturbed viscous force, $\boldsymbol{f'}$, to leading order in H/R and α neglecting the planet potential. The *total* (perturbed plus unperturbed) viscous force is given by

$$\boldsymbol{f_T} = \frac{1}{\rho_T}\nabla\cdot\left(\frac{\alpha\rho_T c^2\boldsymbol{\tau}_T}{\Omega}\right) \tag{E.44}$$

$$= \nabla\cdot\left(\frac{\alpha c^2\boldsymbol{\tau}_T}{\Omega}\right) + \frac{\alpha c^2\boldsymbol{\tau}_T}{\Omega}\nabla\lambda \tag{E.45}$$

where $\lambda_T = \ln \rho_T$ as before,

$$\boldsymbol{\tau} = \begin{bmatrix} 2\frac{\partial v_{R,T}}{\partial R} & R\frac{\partial}{\partial R}\left(\frac{v_{\phi,T}}{R}\right) + \frac{1}{R}\frac{\partial v_{R,T}}{\partial \phi} & \frac{\partial v_{R,T}}{\partial z} + \frac{\partial v_{z,T}}{\partial R} \\ & 2\left(\frac{1}{R}\frac{\partial v_{\phi,T}}{\partial \phi} + \frac{v_{R,T}}{R}\right) & \frac{\partial v_{\phi,T}}{\partial z} + \frac{1}{R}\frac{\partial v_{z,T}}{\partial \phi} \\ & & 2\frac{\partial v_{z,T}}{\partial z} \end{bmatrix} - \frac{2}{3}\left(\nabla \cdot \boldsymbol{v_T}\right) \boldsymbol{I_{3\times 3}} \tag{E.46}$$

and the elements of τ are given in Section 2 of Landau & Lifshitz (1997). We suppress the lower-left elements of the matrix above since their values are apparent from symmetry of the matrix. We neglect bulk viscosity as it does not contribute to the contribute any leading order terms: for the background, $\boldsymbol{\nabla} \cdot \boldsymbol{v} = 0$, so the bulk viscosity drops entirely, and, for the perturbation, $\boldsymbol{\tau'}$ is dominated by the only z-independent terms, τ'_{zz} and $\tau'_{\phi z}$.

Perturbing the viscous force, we get

$$\boldsymbol{f'} = \nabla \cdot (\frac{\alpha c^2 \boldsymbol{\tau}}{\Omega})' + \frac{\alpha c^2}{\Omega}\left(\boldsymbol{\tau \cdot \nabla} \lambda' + \boldsymbol{\tau' \cdot \nabla} \lambda\right) \ . \tag{E.47}$$

The dominant terms in $\boldsymbol{f'}$ will contain either λ' or $\frac{\partial \lambda}{\partial z}$, as they are a factor of c_0^{-2} larger than the rest. The first term on the right hand side of Equation (E.47) contains no such terms, so we neglect it.

The only nonvanishing components of the unperturbed τ matrix are $\tau_{R\phi}$ and $\tau_{\phi z}$. Therefore, we can write

$$\boldsymbol{\tau \cdot \nabla} \lambda' = \tau_{R\phi}\left(\frac{1}{R}\frac{\partial \lambda'}{\partial \phi}\hat{\boldsymbol{R}} + \frac{\partial \lambda'}{\partial R}\hat{\boldsymbol{\phi}}\right) + \tau_{\phi z}\left(\frac{\partial \lambda'}{\partial z}\hat{\boldsymbol{\phi}} + \frac{1}{R}\frac{\partial \lambda'}{\partial \phi}\hat{\boldsymbol{z}}\right) \tag{E.48}$$

$$\approx R\frac{\partial \Omega}{\partial R}\left(\frac{i\lambda'}{R}\hat{\boldsymbol{R}} + \frac{\partial \lambda'}{\partial R}\hat{\boldsymbol{\phi}}\right) + R\frac{\partial \Omega}{\partial z}\left(\frac{\partial \lambda'}{\partial z}\hat{\boldsymbol{\phi}}\right) \tag{E.49}$$

where we neglect the $\hat{z}$ term because it is $O(H^2/R^2)$.

Turning to $\boldsymbol{\tau'} \cdot \boldsymbol{\nabla}\lambda$, all the elements are non-zero. However, from Appendix E.2, we know the leading terms are τ_{Rz} and $\tau_{\phi z}$, which are $O(1)$, while all remaining terms are at least $O(H/R)$. This, along with the fact that the background density dominates over the horizontal ones, reduces $\boldsymbol{\tau'} \cdot \boldsymbol{\nabla}\lambda$ to

$$\boldsymbol{\tau'} \cdot \boldsymbol{\nabla}\lambda \approx (\tau_{Rz}\hat{R} + \tau_{\phi z}\hat{\phi})\frac{\partial \lambda}{\partial z} \ . \tag{E.50}$$

Notably, neither term produces any leading order contribution to f'_z.

Combining terms, and setting $\frac{\partial \lambda}{\partial z} \approx -\frac{\Omega^2 z}{c^2}$ (Equation E.5), we see that the $\hat{\boldsymbol{R}}$ and $\hat{\boldsymbol{\phi}}$ components of Equation (E.47) are

$$f'_R = \frac{\alpha c^2}{\Omega}\frac{\partial \Omega}{\partial R} i\lambda' - \alpha z \Omega \left(\frac{\partial v'_R}{\partial z} + \frac{\partial v'_z}{\partial R} \right) \tag{E.51}$$

$$f'_\phi = \frac{\alpha c^2}{\Omega}\left[R\frac{\partial \Omega}{\partial R}\frac{\partial \lambda'}{\partial R} + R\frac{\partial \Omega}{\partial z}\frac{\partial \lambda'}{\partial z} \right] - \alpha z \Omega \left(\frac{\partial v'_\phi}{\partial z} + \frac{i v'_z}{R} \right) \ . \tag{E.52}$$

Following the process in Appendix E, we multiply the viscous force by $\mathcal{H}_1(\zeta)\psi(\zeta)$ and vertically integrate (in ζ). Therefore, $f'_{R,1}$ is

$$f'_{R,1} = \frac{\alpha c_0^2}{\Omega_0}\frac{\mathrm{d}\Omega_0}{\mathrm{d}R} i\lambda'_1 - \alpha \Omega_0 \left[v'_{R,1} + H\frac{\mathrm{d}v'_{z,0}}{\mathrm{d}R} \right] \tag{E.53}$$

$$= \alpha H \Omega_0^2 \left[\frac{\mathrm{d}\ln \Omega_0}{\mathrm{d}\ln R}\frac{v'_{z,0}}{R\Omega_0} - \frac{v'_{R,1}}{H\Omega_0} - \frac{1}{\Omega_0}\frac{\mathrm{d}v'_{z,0}}{\mathrm{d}R} \right] \tag{E.54}$$

$$= -\alpha H \Omega_0^2 \left[u_r + R\frac{\mathrm{d}u_z}{\mathrm{d}R} \right] \tag{E.55}$$

where in the second line we used Equation (E.17) for λ_1', and in the third we used the definitions of u_z and u_r (Equations E.30 and E.29). Similarly, $if_{\phi,1}'$ is

$$if_{\phi,1}' = \alpha c_0^2 \left[H \frac{\mathrm{d}\ln\Omega_0}{\mathrm{d}\ln R} \frac{\mathrm{d}}{\mathrm{d}R} \left(\frac{i\lambda_1'}{H} \right) + \frac{\mathrm{d}\ln c_0^2}{\mathrm{d}\ln R} \frac{i\lambda_1'}{2R} \right] - \alpha\Omega_0 \left(iv_{\phi,1}' - \frac{H}{R} v_{z,0}' \right) \tag{E.56}$$

$$= \alpha\Omega_0 \frac{H}{R} \left[\frac{R}{\Omega_0} \frac{\mathrm{d}\ln\Omega_0}{\mathrm{d}\ln R} \frac{\mathrm{d}}{\mathrm{d}R} \left(\Omega_0 v_{z,0}' \right) + 2v_{z,0}' + \left(2 + \frac{\mathrm{d}\ln\Omega_0}{\mathrm{d}\ln R} \right) \frac{Rv_{R,1}'}{H} \right] \tag{E.57}$$

$$= \frac{1}{2}\alpha H\Omega_0^2 \left[\hat{\kappa}_0^2 u_r + 2R \frac{\mathrm{d}\ln\Omega_0}{\mathrm{d}\ln R} \frac{\mathrm{d}u_z}{\mathrm{d}R} \right] + 2\alpha H\Omega_0^2 \left(\frac{\mathrm{d}\ln\Omega_0}{\mathrm{d}\ln R} \right)^2 u_z \tag{E.58}$$

where we used Equation (E.16) for $iv_{\phi,1}'$,[4] Equation (E.17) for $i\lambda_1'$, and $\hat{\kappa}_0^2$ is given by Equation (E.31).

Equation (E.58) shows that a rigidly tilted circular disk—i.e., a disk with u_z constant and $u_r = 0$—has non-vanishing viscous force. That might appear surprising on physical grounds. But, in truth, the "extra" term (the term proportional to u_z) in Equation (E.58) arise from the viscous force of the unperturbed disk, which leads to accretion. That claim may be verified by calculating the viscous force in a circular disk with zero inclination, and then tilting the force field, which reproduces u_z term. Alternatively, one could include viscous terms in the background state, in which case the u_z terms cancel out. In either case, one should drop the u_z term if one seeks the effect of viscosity on the warp (as opposed to its effect on accretion). Doing so, Equation (E.58) reduces to

$$if_{\phi,1}' \to \frac{1}{2}\alpha H\Omega_0^2 \left[u_r - 3R \frac{\mathrm{d}u_z}{\mathrm{d}R} \right] , \tag{E.59}$$

[4]The steady-state equations allow us to solve for $f_{\phi,1}'$ from a set of equations (Equations E.16 and E.56). Since the correction will be $O(\alpha^2)$, we neglect it.

after additionally approximating Ω_0 as Keplerian, consistent with the approximations at the beginning of this appendix.

E.5. Combining Results

We now combine the results from the previous two appendices to give the final form of the time-dependent, warp equations we use throughout the main body of the paper. We switch to similar variables as those of Lubow & Ogilvie (2000):

$$W = -iu_z^* \tag{E.60}$$

is the complex inclination,

$$G = \frac{1}{2}\Sigma H^2 R^2 \Omega_0^2 u_r^* \,, \tag{E.61}$$

and an asterisk denotes the complex conjugate. Then Equation (E.43) can be written as

$$\Sigma R^2 \Omega_0 \left[\frac{\partial W}{\partial t} + \frac{\langle \zeta \delta \Phi \rangle}{R^2 \Omega_0^2} \frac{i\Omega_0}{2} W + \frac{1}{4} \alpha R \Omega_0 \frac{H^2}{R^2} \frac{\partial W}{\partial R} \right] = \frac{1}{R} \frac{\partial G}{\partial R} - \frac{3i\alpha G}{2R^2} \tag{E.62}$$

where we have used Equations (E.55) and (E.59) for the viscous forces. In this form, Equation (E.63) is conservation of angular momentum with G being the internal torque. Similarly, the same process applied to Equation (E.42) yields

$$\frac{\partial G}{\partial t} + \left(\hat{\kappa}_0^2 - 1\right) \frac{i\Omega_0}{2} G + \alpha \Omega_0 G = \frac{\Sigma H^2 R^2 \Omega_0^3}{4} \left[(1 + 2i\alpha) R \frac{\partial W}{\partial R} + \frac{\mathrm{d} \ln c_0^2}{\mathrm{d} \ln R} \frac{\langle \zeta \delta \Phi \rangle}{R^2 \Omega_0^2} W \right] \tag{E.63}$$

as the second warp equation. The principal advantage of the equations in this form are that G is roughly a piecewise constant at steady-state, making solving either the time-dependent or steady-state equations much easier.

APPENDIX F

Bending Criterion

We now derive the difference in inclination between the inner and outer disks, ΔW, in steady-state, and use the result to determine an approximate bending criterion. We take $R^3\Omega^2 \approx 1$ and drop most of the viscous terms.[1] These allow Equation (E.63) to be written as

$$\frac{\mathrm{d}W}{\mathrm{d}R} = (\epsilon_H - \epsilon_p - 2i\alpha)\,\frac{2iG}{\Sigma H^2}\ , \tag{F.1}$$

where $\hat{\kappa}_0^2 - 1 \equiv \epsilon_H - \epsilon_p$ and

$$\epsilon_p \sim \frac{\mu R_p^2}{(R-R_p)^2 + h_s^2} \tag{F.2}$$

$$\epsilon_H \sim \frac{H^2}{R^2}\left[\frac{\mathrm{d}\ln\Sigma}{\mathrm{d}\ln R} + \frac{\mathrm{d}\ln^2\Sigma}{\mathrm{d}\ln R^2}\right]\ . \tag{F.3}$$

$\epsilon_p = \frac{\mu R^2}{2R_p^2} b_{3/2}^{(1)}(R/R_p)$ is the exact form (taken from Equations 2.4 and 2.12)) where $b_s^{(j)}(\alpha)$ is the Laplace coefficient, and Equation (F.2) is a modification of the approximation given in Equation (45) of Laskar & Robutel (1995).[2] Similarly, the angular momentum equation

[1] The viscous terms, other than $\alpha\Omega_0 G$, primarily influence the twist and $\arg(G)$ and only minorly affect $|W_{\rm in}|$.

[2] We modify the approximation in two ways: we include a softening radius and we take $R^2 \to R_p^2$ in the numerator. This latter approximation is so that the approximation is better at the planet at the expense of $R \ll 1$.

(Equation E.62) is

$$\frac{\mathrm{d}G}{\mathrm{d}R} = -\frac{1}{2}\Sigma\epsilon_p i W \ . \tag{F.4}$$

where we Taylor expand the planet potential about $z = 0$ to get:

$$\frac{\langle\zeta\delta\Phi\rangle}{R^2\Omega_0^2} \approx \epsilon_p \ . \tag{F.5}$$

In order to determine the bending criterion, we solve perturbatively, following Foucart & Lai (2014). We assume that $W = W^{(0)} + W^{(1)}(R)$, where the unperturbed $u_z^{(0)}$ is independent of R and, in our setup, is equal to the disk's inclination far beyond the planet. We do the same thing for G, where $G^{(0)} = 0$ for the unperturbed disk, matching our inner boundary condition. The angular momentum equation yields, to first order,

$$G^{(1)}(R) = -\frac{1}{2}iW^{(0)}\int_0^R \Sigma(R')\epsilon_p(R')\ \mathrm{d}R' \ . \tag{F.6}$$

We then insert this into Equation (F.1) to yield the change in inclination:

$$\Delta W = W^{(1)}(R\to\infty) - W^{(1)}(R=0) \tag{F.7}$$

$$= \int_0^\infty (\epsilon_p + \epsilon_H - 2i\alpha)\frac{2iG^{(1)}}{\Sigma H^2}\ \mathrm{d}R \ . \tag{F.8}$$

The bending criterion is that

$$|\Delta W|/W^{(0)} \gtrsim 1 \ . \tag{F.9}$$

It may be evaluated for any assumed values for Σ, H, μ, and h_s. In the following, we derive simple rough expressions for the bending criterion, considering four cases of increasing complexity.

F.1. Inviscid with a Shallow Gap

We consider first the "stiffest" case: an inviscid disk with a shallow gap. Because $\epsilon_p(R)$ is a sharply-peaked function with maximum at $R \sim R_p$, provided the gap is not too deep (see Appendix F.2 for quantification), we may approximate

$$G^{(1)} \sim \begin{cases} -iW^{(0)}\Sigma(R)E(R) & R \lesssim R_p - h_s \\ -iW^{(0)}\Sigma(R_p)E(R \to \infty) & R \gtrsim R_p - h_s \end{cases} \tag{F.10}$$

where

$$E(R) \equiv \int_0^R \epsilon_p(R')\ \mathrm{d}R' \tag{F.11}$$

$$\sim \mu R_p^2 \begin{cases} \frac{1}{R_p - R} & R \lesssim R_p - h_s \\ \frac{1}{h_s} & R \gtrsim R_p - h_s \end{cases} . \tag{F.12}$$

Therefore, for an inviscid shallow gap, Equation (F.8) becomes

$$\Delta W \sim -\int_0^\infty \frac{\epsilon_p i G^{(1)}}{\Sigma H^2}\,\mathrm{d}R \tag{F.13}$$

$$\sim W^{(0)}\int_0^{R_p}\frac{E(R)\epsilon_p}{H^2}\,\mathrm{d}R \tag{F.14}$$

$$\sim W^{(0)}\frac{E(R)^2}{H^2}\,\mathrm{d}R \tag{F.15}$$

$$\sim W^{(0)}\frac{\mu^2 R_p^4}{H^2 h_s^2}\,, \tag{F.16}$$

where the last line takes $\epsilon_p \gg \epsilon_H$, which is valid for a shallow gap. The bending criterion (Equation F.9) becomes

$$\mu \gtrsim \frac{h_s H}{R_p^2} \quad \text{(inviscid shallow gap)}\,. \tag{F.17}$$

F.2. Inviscid with a Deep Gap

We now consider the case of a deep gap. We denote the gap width by Δ_{gap}, and the gap depth by Σ_{gap}. The key difference when considering a deep gap is that the integral in Equation (F.6) is dominated by the region interior to the gap. Then, provided the gap is sufficiently deep, then at radii $R \gtrsim R_p - \Delta_{\text{gap}}$, we have

$$\int_0^R \Sigma(R')\epsilon(R')\,\mathrm{d}R' \sim (\Sigma E)|_{R=R_p-\Delta_{\text{gap}}} \tag{F.18}$$

$$\sim \frac{\mu R_p^2}{\Delta_{\text{gap}}}\Sigma_0\,, \tag{F.19}$$

where Σ_0 is the value interior to the gap (i.e., the ungapped value). For the above equation to hold, the integral in the gap region,

$$\int_{R_p-\Delta_{\rm gap}}^{R_p} \Sigma(R')\epsilon(R')\ \mathrm{d}R' \sim \frac{\mu_p R_p^2}{h_s}\Sigma_{\rm gap}\ , \tag{F.20}$$

must be subdominant. In other words, a "sufficiently deep" gap satisfies

$$\frac{\Sigma_{\rm gap}}{\Sigma_0} \lesssim \frac{h_s}{\Delta_{\rm gap}}\ . \tag{F.21}$$

Inserting Equation (F.19) into Equation (F.6) shows that for such a gap

$$G^{(1)} \sim -\frac{\Sigma_0\mu_p R_p^2}{\Delta_{\rm gap}} iW^{(0)}\ , \qquad \text{for } R \gtrsim R_p - \Delta_{\rm gap} \tag{F.22}$$

Inserting that into Equation (F.8) gives

$$\Delta W \sim \frac{iG^{(1)}}{\Sigma_{\rm gap}H^2}\int_{R_p-\Delta_{\rm gap}}^{\infty} \epsilon_p\ \mathrm{d}R \tag{F.23}$$

$$\sim W^{(0)}\frac{\Sigma_0}{\Sigma_{\rm gap}}\frac{\mu R_p^4}{H^2 h_s \Delta_{\rm gap}} \tag{F.24}$$

where in the first line we drop ϵ_H for simplicity, even though, for a sufficiently deep gap, it could play a role at the gap edge. Therefore, the bending criterion becomes

$$\mu \gtrsim \left(\frac{\Sigma_{\rm gap}}{\Sigma_0}\frac{h_s\Delta_{\rm gap}}{R_p^2}\right)^{1/2}\frac{H}{R_p} \quad \text{(inviscid deep gap)}\ . \tag{F.25}$$

F.3. Viscous with a Shallow Gap

When viscosity is included ($\alpha \neq 0$), the torque is unchanged (Equation F.6), but α contributes a term to W (Equation F.8):

$$\Delta W|_\alpha \sim \alpha \int_0^\infty \frac{G^{(1)}}{\Sigma H^2} dR \tag{F.26}$$

$$\begin{aligned} &\sim -i\alpha W^{(0)} \left[\frac{1}{H^2} \int_0^{R_p} E(R)\, \mathrm{d}R \right. \\ &\left. + E(\infty) \int_{R_p}^\infty \frac{\Sigma(R_p)}{\Sigma H^2}\, \mathrm{d}R \right] \end{aligned} \tag{F.27}$$

which is found by inserting Equation (F.10) into Equation (F.8). The second integral converges provided we assume that $\Sigma H^2/R$ is an increasing function of R, which is always true for a viscous steady-state disk. In that case, both integrals have comparable magnitudes, yielding

$$\Delta W|_\alpha \sim -i\alpha W^{(0)} \frac{\mu R_p^3}{h_s H^2} \tag{F.28}$$

And therefore viscosity will cause the disk to bend provided

$$\mu\alpha \gtrsim \frac{h_s H^2}{R_p^3} \tag{F.29}$$

Comparing with the inviscid case (Equation F.17), we infer the following: if $\alpha < H/R_p$, then the bending criterion is the inviscid one; where as is if $\alpha > H/R_p$, then then the critical μ for bending is smaller than the inviscid one by $\frac{H}{R_p \alpha}$.

F.4. Viscous with a Deep Gap

When a deep gap is present, the viscosity contributes primarily between the planet and the outer edge of the gap. Therefore, inserting Equation (F.22) into Equation (F.8) gives

$$\Delta W|_\alpha \sim -i\alpha\mu_p W^{(0)} \frac{\Sigma_0 R_p^2}{\Delta_{\rm gap}} \int_{R_p-\Delta_{\rm gap}}^{\infty} \frac{1}{\Sigma H^2} dR \tag{F.30}$$

$$\sim -i\alpha\mu W^{(0)} \frac{\Sigma_0 R_p^2}{\Sigma_{\rm gap} H^2} \tag{F.31}$$

i.e., the bending criterion is

$$\mu\alpha \gtrsim \frac{\Sigma_{\rm gap}}{\Sigma_0} \frac{H^2}{R_p^2} \ . \tag{F.32}$$

Again, comparing with the inviscid result (Equation F.25), we find that the criterion is the inviscid one when $\alpha \lesssim \frac{\Sigma_0}{\Sigma_{\rm gap}} \frac{H^2}{h_s \Delta_{\rm gap}}$, and Equation (F.32) otherwise.

APPENDIX G

Computational Methods

We simulate 3D accretion disks using the moving-mesh code AREPO (Springel, 2010; Pakmor et al., 2016) in its Navier-Stokes version (Muñoz et al., 2013). We choose this numerical scheme because of its unstructured, moving mesh, which offers three main benefits: (i) The resolution elements follow the motion of the disk, capturing orbital, viscous, and bending motion easily, while also keeping the resolution elements in the regions of interest. (ii) It allows for flexible refinement conditions, which permits the necessary higher resolutions in the disk midplane when there is a sharp bend, such as near the planet. (iii) It enables us to simulate large disks with little additional cost, as the time step for larger cells decreases.

G.1. Gravitational Potential

The star's gravitational force is including directly with a spline softening for $r < 0.1R_p$ (e.g., Springel et al., 2001). We implement the planet through the the time-averaged potential in Equation (2.4). The planet's angular momentum is aligned with the coordinate frame's z-axis. The derivatives of the potential are pre-computed numerically on an (R, z) grid and provided to AREPO. The force on a cell is calculated by linearly extrapolating between the grid points.

G.2. Initial Conditions

We initialize a locally isothermal, power-law α-disk with $q = p = -1/2$ (Section 2.2.1).[1] Therefore, the outer part of the disk—where the planet has no effect—is already in steady-state. We reduce Σ rapidly inside of $R_{\rm in} = 0.1R_p$ and outside of $R_{\rm out} = 100R_p$. We translate $\Sigma(R)$ to $\rho(R, z)$ by applying vertical hydrostatic balance (Equation E.5). Similarly, we get the azimuthal velocity by next applying centrifugal balance (Equation E.4). The radial and vertical velocities are initialized as zero, as the viscous flow is very small compared to the azimuthal flow.

G.3. Mesh Construction and Refinement Criteria

AREPO is a Godunov-type finite volume method (e.g., Toro, 2009) implemented on a continuously deforming Voronoi tessellation (e.g., Serrano & Español, 2001), itself generated from a set of mesh-generating points. The mesh-generating points can be placed across the computational domain in an arbitrary fashion. For 2D accretion disks, a quasi-polar allocation of points may be desirable (e.g., Muñoz et al., 2014). Alternatively, a Monte-Carlo sampling of the density field can be used to produce nearly constant mass Voronoi cells in 3D (e.g., Muñoz et al., 2015). Volume-based and mass-based approaches can also coexist in a single simulation, alternating them depending on location within the computational domain (e.g., Muñoz & Lai, 2016).

In this work, we choose to allocate mesh-points quasi-cylindrically in 3D, using an ad-hoc scheme that allocates $N_\phi(R, z)$ cells spaced uniformly in the ϕ-direction for any

[1] Because we neglect self-gravity, Σ_0 scales out of the problem and is, therefore, an irrelevant a parameter.

given R and z. The resolution function is defined as

$$N_\phi(R,z) = N_{\rm disk} f(R) g(z/z_{\rm decay}) \ . \tag{G.1}$$

where $f(R)$ and $g(z)$ are arbitrary functions that are responsible for allocating most Voronoi cells closer to the disk midplane and closer to $R = R_{\rm p}$ (see Figure G.1). Our fiducial resolution scale is represented by $N_{\rm disk} = 50$.

First, we place a ring of $N_\phi(R_{\rm p}, 0)$ mesh-generating points in the disk's midplane at $R = R_{\rm p}$. We then place additional rings inside/outside our first ring radially spaced by the azimuthal spacing of the original ring. Rings are added in this way until the whole midplane is filled. Next, we place rings of $N_\phi(R,z)$ points above and below each current ring, with the vertical position of the new ring equal to the azimuthal spacing of the old ring. This process is repeated until the entire computational box is filled. Finally, we misalign the disk to the planet by rotating our mesh by the inclination I about the y-axis, and the twist γ about the z axis. We typically initialize our disks with $I_0 = 1^\circ$ and $\beta_0 = 0^\circ$.

This mesh-allocation procedure consequently defines a space-varying inter-cell separation of $\simeq 2\delta_{\rm targ}$ where we have defined the "target cell radius"

$$\delta_{\rm targ} \equiv \frac{\pi \tilde{R}}{N_\phi(\tilde{R},\tilde{z})} \ , \tag{G.2}$$

where the tilde denotes coordinates measured relative to the disk midplane. This reference size provides us with a resolution criterion to be implemented throughout the duration of the simulation: cells with $r_{\rm cell} > 2\delta_{\rm targ}$ are flagged for splitting, while $r_{\rm cell} < 2\delta_{\rm targ}$ are flagged for merging (Springel, 2010).

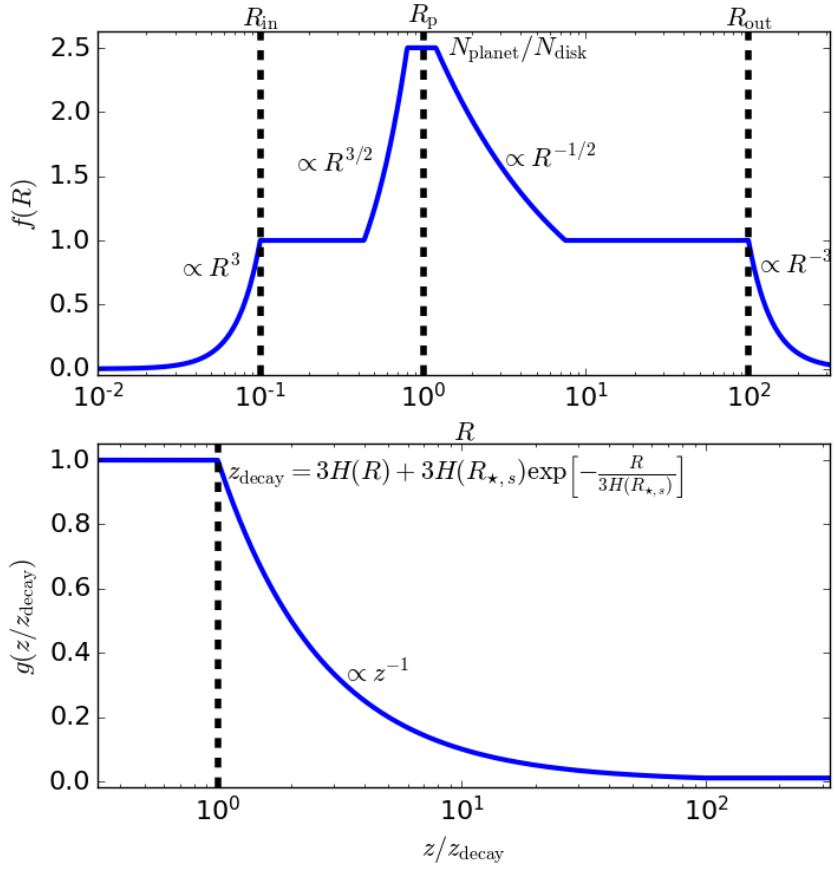

Figure G.1. Here we show $f(R)$ and $g(z)$ from Equation (G.1) for $N_\phi = 100$, $N_p = 250$, $R_{\rm in} = 0.1$, and $R_{\rm out} = 100$.

G.4. Boundary Conditions

Our disk is embedded in a large cube, $R_{\rm box} = 250R_p$ with periodic boundary conditions. This condition creates spurious reflections at the boundary, but because the region outside the disk has an extremely low density and evolves on a timescale much longer than our runtime, it does not affect the disk.

The inner boundary presents more difficulties. AREPO has no computational inner boundary. However, do to the dynamics of the system, mass will pile up at the star

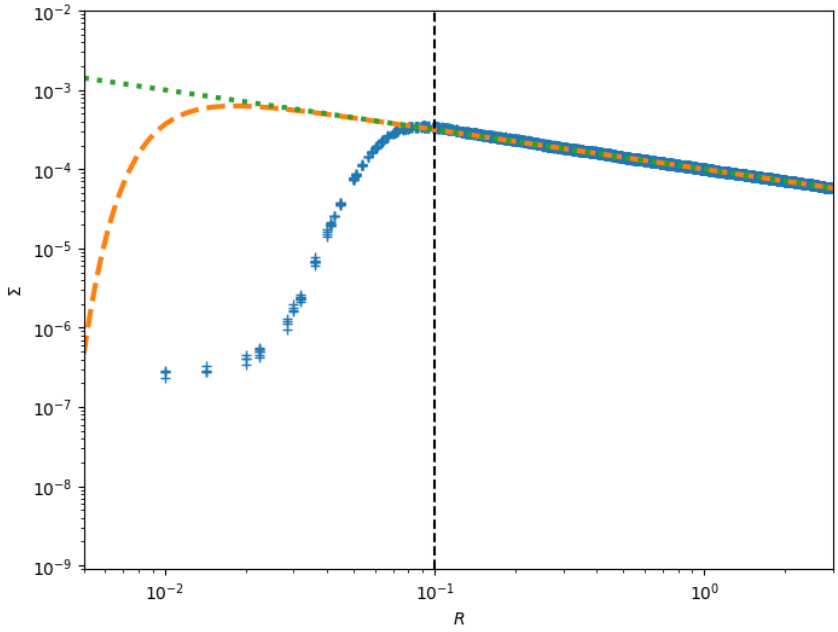

Figure G.2. The Σ profile for a simulations of a flat disk without a planet. The orange dashed line is the initial condition, the green line is the viscous steady-state solution, and the blue points are the simulation after one viscous time at the inner boundary. The numerical solution matches well to the theoretical prediction, validating our choice of inner boundary condition.

as the disk accretes. Consequently, this extraneous, excess mass needs to be removed. So, we model the computational inner edge of the disk by an accretion region of radius $r_{\rm acc} = 0.1R_{\rm p}$ where the mass of each volume element is gradually drained. This accretion radius is assumed to be much larger than the "true" inner edge ($\approx$ the stellar radius). Consequently, the boundary condition implemented there must obey the "torque free" behavior described by Dempsey et al. (2020). That is, angular momentum must be conserved as mass is removed. Dempsey et al. (2020) do this in 2D by increasing the azimuthal velocity of a cell as its mass is removed. We extend this to 3D by increasing velocity in both the azimuthal and polar directions. Specifically, inside radius $r_{\rm acc}$, we

remove mass during a timestep by

$$\rho\left(t+\Delta t\right)-\rho\left(t\right)=-\gamma\left(r\right)\rho\left(t\right)\Delta t \tag{G.3}$$

where $\gamma\left(r\right)=$ is our mass removal function. When we remove mass, we also boost the velocity by

$$\frac{\left|\Delta v_{\phi}\right|}{\left|v_{\phi}\right|}=\frac{\Delta\rho}{\rho} \qquad\qquad \frac{\left|\Delta v_{\theta}\right|}{\left|v_{\theta}\right|}=\frac{\Delta\rho}{\rho} \tag{G.4}$$

and thus angular momentum is conserved across the boundary. We show in Figure G.2 that the steady-state $\Sigma\left(r\right)$ profile is preserved into the inner boundary with this boundary condition. This validates that this is the correct inner boundary condition to use for our 3D simulations.

For the systems we are examining, the part of the disk interior to the planet is off less importance as it roughly has constant inclination and zero internal torque. Therefore, for the sake of computational time, we drop the resolution significantly inside the planet, and only preserve the proper Σ profile outside of the planet. For example, the Σ profile for simulation shown in the first row of Figure 2.5 is shown in Figure G.3 at the same times. In this instance, Σ does initially evolve inside of R_p until settling to an incorrect steady-state. However, it stays roughly the viscous steady-state solution for $R \gtrsim R_p$, which is the region of interest.

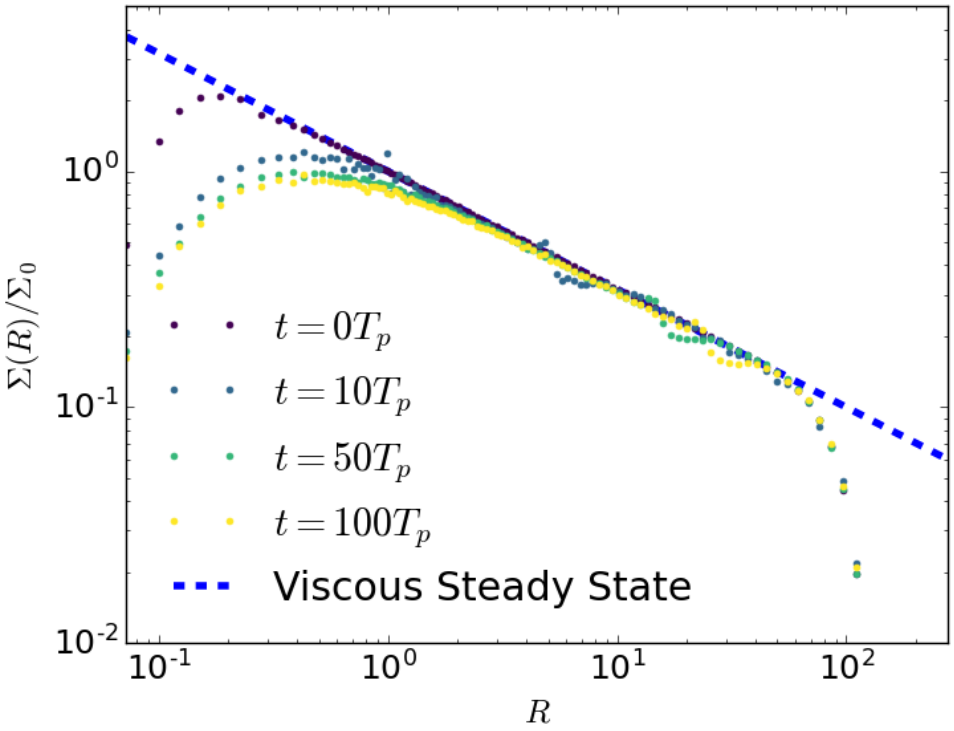

Figure G.3. The Σ profile for the AREPO simulation corresponding to the first row of Figure 2.5. The viscous steady-state solution is shown in blue. While the simulation does not match the correct solution up to the inner boundary, it is correct in the region of interest, from $R \sim 1$ to $R \sim 50$.